

2018-01-01

# Geophysical Investigations Of Southcentral Alaska

Felix Dziedzorm Ziwu

University of Texas at El Paso, [dziezi@yahoo.com](mailto:dziezi@yahoo.com)

Follow this and additional works at: [https://digitalcommons.utep.edu/open\\_etd](https://digitalcommons.utep.edu/open_etd)



Part of the [Geophysics and Seismology Commons](#)

---

## Recommended Citation

Ziwu, Felix Dziedzorm, "Geophysical Investigations Of Southcentral Alaska" (2018). *Open Access Theses & Dissertations*. 191.  
[https://digitalcommons.utep.edu/open\\_etd/191](https://digitalcommons.utep.edu/open_etd/191)

This is brought to you for free and open access by DigitalCommons@UTEP. It has been accepted for inclusion in Open Access Theses & Dissertations by an authorized administrator of DigitalCommons@UTEP. For more information, please contact [lweber@utep.edu](mailto:lweber@utep.edu).

# GEOPHYSICAL INVESTIGATIONS OF SOUTHCENTRAL ALASKA

ZIWU FELIX DZIEDZORM

Doctoral Program in Geological Sciences

APPROVED:

---

Diane I. Doser, Ph.D., Chair

---

Laura F. Serpa, Ph.D.

---

Kevin Mickus, Ph.D.

---

Terry L. Pavlis, Ph.D.

---

Hector Gonzalez-Huizar, Ph.D.

---

Charles Ambler, Ph.D.  
Dean of the Graduate School

Copyright ©

by

Ziwu Felix Dzedzorm

2018

GEOPHYSICAL INVESTIGATIONS OF SOUTHCENTRAL ALASKA

by

ZIWU FELIX DZIEDZORM, BSc., MS.

DISSERTATION

Presented to the Faculty of the Graduate School of

The University of Texas at El Paso

in Partial Fulfillment

of the Requirements

for the Degree of

DOCTOR OF PHILOSOPHY

Department of Geological Sciences

THE UNIVERSITY OF TEXAS AT EL PASO

December 2018



## **ACKNOWLEDGEMENTS**

My sincere gratitude to the members of my dissertation committee for their immense support and guidance. To Mr. Galen Kaip and Mr Carlos Montana for their technical support and training. To my wife Esenam Adzo Fumador for her immense moral and emotional support throughout my studies.

## **ABSTRACT**

Two different geophysical studies were conducted within southcentral to as part of the ongoing research to understand the tectonics and the driving mechanism that produces complex deformations in this region. The objective of the first research is to understand the geometry and motion along the Castle Mountain Fault (CMF) and how its neighboring Susitna basin and Matanuska Valley influence the behavior of this fault. Gravity and magnetic data were used to generate cross sections along the fault. Four profiles were generated across the length of CMF. The models show a high angle reverse fault cutting through Mesozoic. This deformation shows a high degree deformation across the length of CMF. Other rocks layers modelled within the profiles are Tertiary sedimentary rocks, Cretaceous igneous rocks, Serpentinized rocks, Border Range Ultramafic mafic assemblages (BRUMA), a layer of low velocity density zone (LVDZ), and Peninsula Terrane basement rocks and the subducting Yakutat microplate. Relocated seismic plots across the cross sections indicates active motion along the west CMF (WCMF) as compared to the east CMF (ECMF). The second study entails using magnetic, temperature, gravity, earthquake and GPS to analyze current subsidence within Cook Inlet basin and uplift along the Kenai Mountain. The vertical motion within this region has been attributed to the presence of serpentinized blocks beneath the basin. Consequently, the first approach is to investigate the presence of serpentinized block beneath CIB using a 3D inversion of magnetic and gravity data. The inverted magnetic results are constraints with power density spectrum analysis and temperature depth profiles. The results of this study do not support serpentinization. Furthermore, I speculate the subsidence of the CIB and uplift of the Kenai Mountains is controlled by oroclinal bending produce by the subduction of Yakutat microplate.

## TABLE OF CONTENTS

ACKNOWLEDGEMENTS .....	iv
ABSTRACT.....	v
TABLE OF CONTENTS.....	vi
LIST OF TABLES .....	viii
LIST OF FIGURES .....	ix
SECTION 1.....	1
A GEOPHYSICAL STUDY OF THE CASTLE MOUNTAIN FAULT SYSTEM AND MATANUSKA-VALLEY NEAR ANCHORAGE, ALASKA .....	1
1.1 ABSTRACT.....	1
1.2 INTRODUCTION .....	2
1.3 TECTONIC AND GEOLOGIC SETTING .....	5
1.4 PREVIOUS STUDIES .....	8
1.5 METHODOLOGY .....	18
1.6 RESULTS AND INTERPRETATION OF 2D MODELS .....	26
1.7 DISCUSSION .....	33
1.8 CONCLUSIONS.....	35
1.9 REFERENCES .....	37
SECTION 2.....	43
Geophysical investigation of structural and tectonic vertical motion within Cook Inlet basin and Kenai Mountain, Alaska .....	43
2.1 ABSTRACT.....	43
2.2 INTRODUCTION .....	45

2.1 BACKGROUND .....	48
2.2 INVESTIGATING THE PRESENCE OF SERPENTINIZATION BENEATH COOK INLET BASIN .....	54
2.3 METHODOLOGY .....	57
2.4 Comparing results with earthquake and GPS information .....	92
2.5 DISCUSSION .....	100
2.6 CONCLUSION.....	106
2.7 REFERENCES .....	108
SECTION 3.....	125
APPENDIX A.....	125
APPENDIX B .....	126
APPENDIX C .....	128
VITA.....	131

## LIST OF TABLES

Table 1: Densities and Magnetic Susceptibilities used in 2D Forward Modeling.....	25
Table 1: Estimated depths of depth to top ( $Z_t$ ), centroid ( $Z_c$ ) and bottom ( $Z_b$ ) of high magnetic anomalies within the CIB.....	75
Table 2: Values for temperature calculations for Alaska. Data for Anchorage were used in the temperature calculation for CIB and its vicinities). (Modified from Batir et al., 2016).....	76

## LIST OF FIGURES

Figure 1. Tectonic setting of southern Alaska showing relationship between collision of the Pacific plate and Yakutat block with North American plate..	3
Figure 2. Geologic map of the Castle Mountain Fault and Matanuska-Susitna study area showing locations of all gravity measurements.....	4
Figure 3. Map of study area. ....	7
Figure 4. Seismicity of the study area.....	13
Figure 5. Cross section of seismicity along the Castle Mountain fault. ....	14
Figure 6. Bouguer gravity anomaly map of study area with relocated seismicity.....	15
Figure 7. Aeromagnetic map of study area with relocated seismicity..	16
Figure 8. Structural models based on 2.5-D modeling of gravity and magnetic data for the study area. ....	17
Figure 9. Simple Bouguer anomaly map gridded at 1000 m..	22
Figure 10. Total intensity aeromagnetic map gridded at 1000 m..	23
Figure 11: 2D profile A-A' showing the western CMF forming at the contact of Cretaceous igneous rock and Late Mesozoic sedimentary rocks. ....	29
Figure 12: 2D profile B-B' showing the west CMF cutting through the late Mesozoic sedimentary rock. ....	30
Figure 13: 2D profile C-C' showing eastern CMF cutting through the late Mesozoic sedimentary rock..	31
Figure 14: Profile D-D' showing eastern CMF formed at the contact of the Cretaceous igneous rock and the late Mesozoic sedimentary rock.....	32

Figure 1: Map of the Cook Inlet Basin, Alaska, showing recent faults and folds related to deformation in the region.....	47
Figure 2: Geologic map of CIB, Kenai Peninsula and Chugach Mountains, locations of gravity points and mapped faults and folds.....	51
Figure 3: The aeromagnetic map shows long wavelength anomalies trending SW to NE within the CIB.. .....	62
Figure 4: Complete Bouguer anomaly map of CIB showing a southwest to northeast trending long wavelength low gravity anomaly. Selected blocks for 3D inversion are 4, 6, 7, 10, 11 and 16.....	63
Figure 5a: Aeromagnetic map of block 4(A) and 6 (B). Lines 1 and 2 are used to show a west/east cross section and a north/south cross section of the inversion models (Figures 6a)respectively. ....	64
Figure 5b: Aeromagnetic map of block 7(A) and 11(B). Lines 1 and 2 are used to show the west/east face and north/south face cross sections of the inversion models (Figure 6b) .	
CMF=Castle Mountain Fault, BRF=Border Range Fault.....	65
Figure 5c: Aeromagnetic map of block 10 and 16. The map on the on the left is block 10 and the map on the right is block 16. Lines 1 and 2 are used to indicate the west/east face and north/south cross sections of inversion models .....	66
Figure 6a: Cross sections of 3D inversion models showing depth and geometry of magnetic susceptibility sources determined from inversion of magnetic anomaly data.. .....	67
Figure 6b: Cross sections of 3D inversion models showing depth and geometry of magnetic susceptibility sources determined from inversion of magnetic anomaly data. ....	68

Figure 6c: Cross sections of 3D inversion models showing depth and geometry of magnetic susceptibility sources determined from inversion of magnetic anomaly data. ....	69
Figure 7: Aeromagnetic anomaly map randomly drawn white lines across positive long wavelength anomalies.....	72
Figure 8: Example of the spectral analysis technique for line 4-4' . ....	74
Figure 9: Temperature curves showing changes with depth.....	78
Figure 10a: The Bouguer gravity anomaly maps for block 4 (A) and 6 (B). ....	84
Figure 10b: Bouguer gravity anomaly maps for blocks 7 (A) and 11 (B).....	85
Figure 10c: Bouguer anomaly maps for blocks 10 (A) and 16 (B). ....	86
Figure 11a: 3D gravity inversion models. 1 and 2 on the left side are the east and south cross sections of the block 4. 1 and 2 on the right side are the west and north faces respectively of block 6.....	87
Figure 11b: 3D gravity inversion model for block 7. 1 and 3 are west cross sections. 2 and 4 are the south cross sections.....	88
Figure 11c: 3D gravity inversion model for block 11. 1 and 3 are east cross sections. 2 and 4 are the south cross sections. ....	89
Figure 11d: 3D gravity inversion model for block 10. 1 and 3 are west cross sections. 2 and 4 are south cross sections.....	90
Figure 11e: 3D gravity inverted Bouguer anomaly showing density contrast for block 16. 1 and 3 are west cross sections 2 and 4 are south cross sections.....	91
Figure 12: Earthquake relocated events superimposed on the complete Bouguer gravity map:..	93
Figure 13a: East west profile showing hypocenter of seismic events with a map zone of LDZ (low density zone) and subducting plate.....	94



Figure 13b: Profile 2 is a west east vertical profile south along the southern boundary of the low Bouguer anomaly within the basin. ....	95
Figure 13c: Profile 3 showing seismic events running north south through CIB. LDZ=Low density zone .....	96
Figure 14: GPS time series plot for data AC11 showing the rate of vertical motion (unit is mm/day). ....	98
Figure 15: Rate of uplift contours within CIB from time series GPS data superimposed on complete Bouguer gravity anomaly map.. ....	99
Figure 16: Complete Bouguer map with Isovelocity contours showing estimates of depth (km) to Moho within the southcentral Alaska showing crustal thickness within the basin.....	102
Figure 17a: Cartoon summary of tectonic deformation causing subsidence and shortening of CIB and uplift of Kenai. ....	103
Figure 17b: Cross sectional profile of the subducting Pacific plate and overriding North American Plate with the subsidence and uplift of CIB and Kenai Mountains respectively. ....	104

## **SECTION 1**

# **A GEOPHYSICAL STUDY OF THE CASTLE MOUNTAIN FAULT SYSTEM AND MATANUSKA-VALLEY NEAR ANCHORAGE, ALASKA**

### **1.1 ABSTRACT**

The Castle Mountain Fault (CMF) is the closest (<50 km) active fault to Anchorage, Alaska and is known to be capable of producing earthquakes of magnitude 7.0 – 7.1. While several mapping and trenching studies have been conducted along the CMF, geophysical investigations along the fault zone have been limited. We use over 700 recently collected, closely spaced gravity observations, in addition to existing regional gravity, aeromagnetic, seismic reflection, well log data, and geologic information, to develop new 2D models of the deeper structure of the CMF system. We developed four 2D integrated forward models across the Castle Mountain Fault. These models indicate differences between the western and eastern segments of the Castle Mountain Fault. The models show a thick sequence of Tertiary to Mesozoic sediments overlying the Peninsular terrane basement at varying depths within the area. We identified two main intrusive granitic rocks based on the varying susceptibilities. These granitic rocks share a possible fault contact with the Mesozoic sedimentary rocks. The model also shows that the CMF cuts through the Mesozoic sediments at depth. These rocks can create strong coupling along the fault and with the decreasing eastward angle of subduction, it is highly for fluid migration to the eastern edge of the subducting Yakutat microplate. Seismic events plotted along the profiles supports the Holocene motion along the western CMF (WCMF) and indicates a deeper extent of the CMF into the crust. The eastern CMF shows high rate of deformation based on the structures associated with the Mesozoic rocks.

## 1.2 INTRODUCTION

The Castle Mountain Fault (CMF) is located in southern Alaska <50 km north of downtown Anchorage, and represents a structural feature influenced by complex tectonic processes above a subduction zone that is itself complicated by collisional tectonics (Figures 1 and 2). Geologic studies show that stress accumulation along the fault is capable of producing magnitude ~7 earthquakes (Haeussler et. al., 2002). As the Anchorage metropolitan area expands toward the Matanuska-Susitna (Matsu) Valley regions and closer to the CMF, potential seismic hazards increase significantly. Seismic hazards associated with elevated seismicity along the CMF motivate geophysical investigations aimed at better understanding the subsurface structure of the fault and how it may control local fault segmentation and depth of seismicity. Our 2D geophysical models of the deeper structure of the CMF system and Matsu Valley area (61-62°N Latitude and 148-152°W Longitude) lead to better understanding of the interaction between the CMF and other local active faults and folds. Understanding the relationship between the structure along the CMF and its influences on the faults seismic behavior is critical to better predicting strong ground motion from earthquakes occurring along the fault zone.

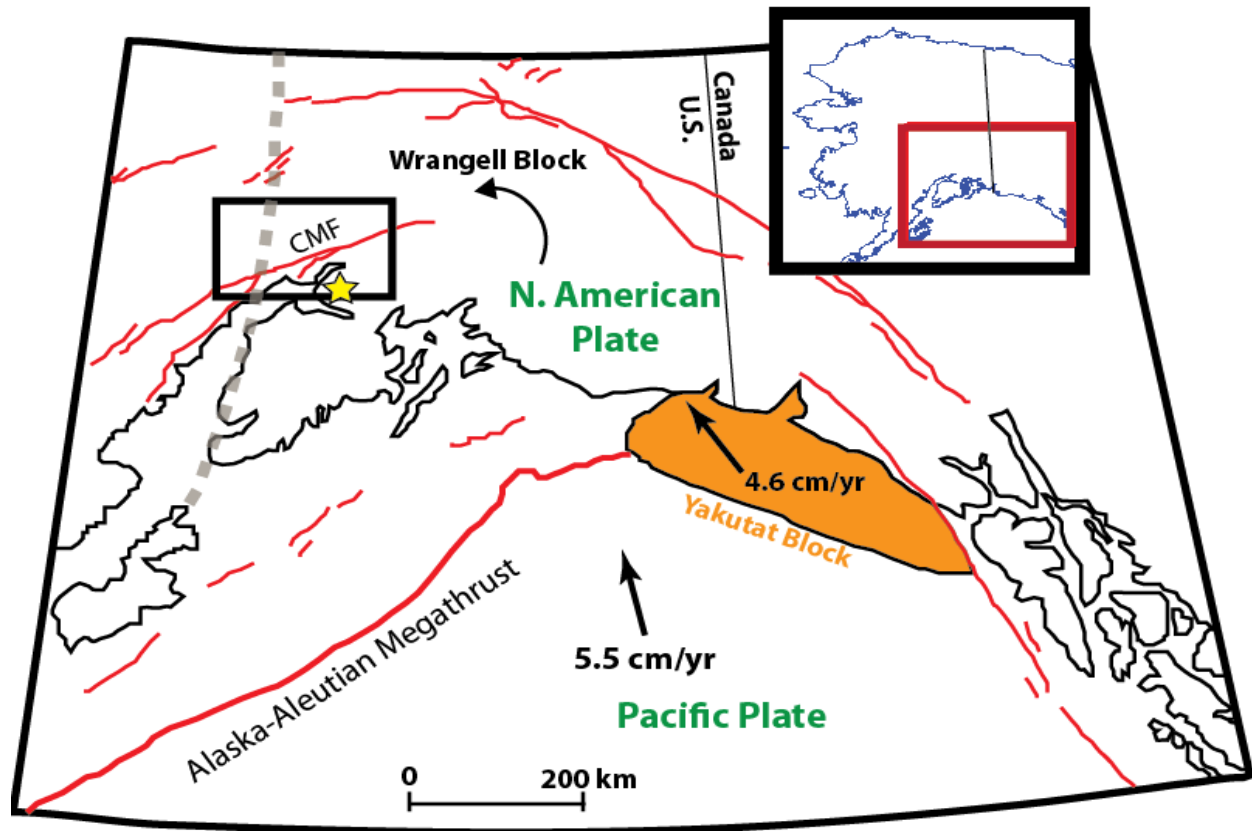


Figure 1. Tectonic setting of southern Alaska showing relationship between collision of the Pacific plate and Yakutat block with North American plate. Counter clockwise pointing arrow shows hypothesized direction of movement of the Wrangell block with respect to North America. Dashed gray line shows interpretation Wrangell block boundary. Thin dashed line represents southwestern edge of subducting Yakutat block. Black rectangle indicates study area and yellow star within study area is Anchorage. Bold red line is Alaska-Aleutian Megathrust and thin red lines are faults. Arrows show directions of plate motions relative to stable North America. Figure modified from Haeussler et.al, 2000.

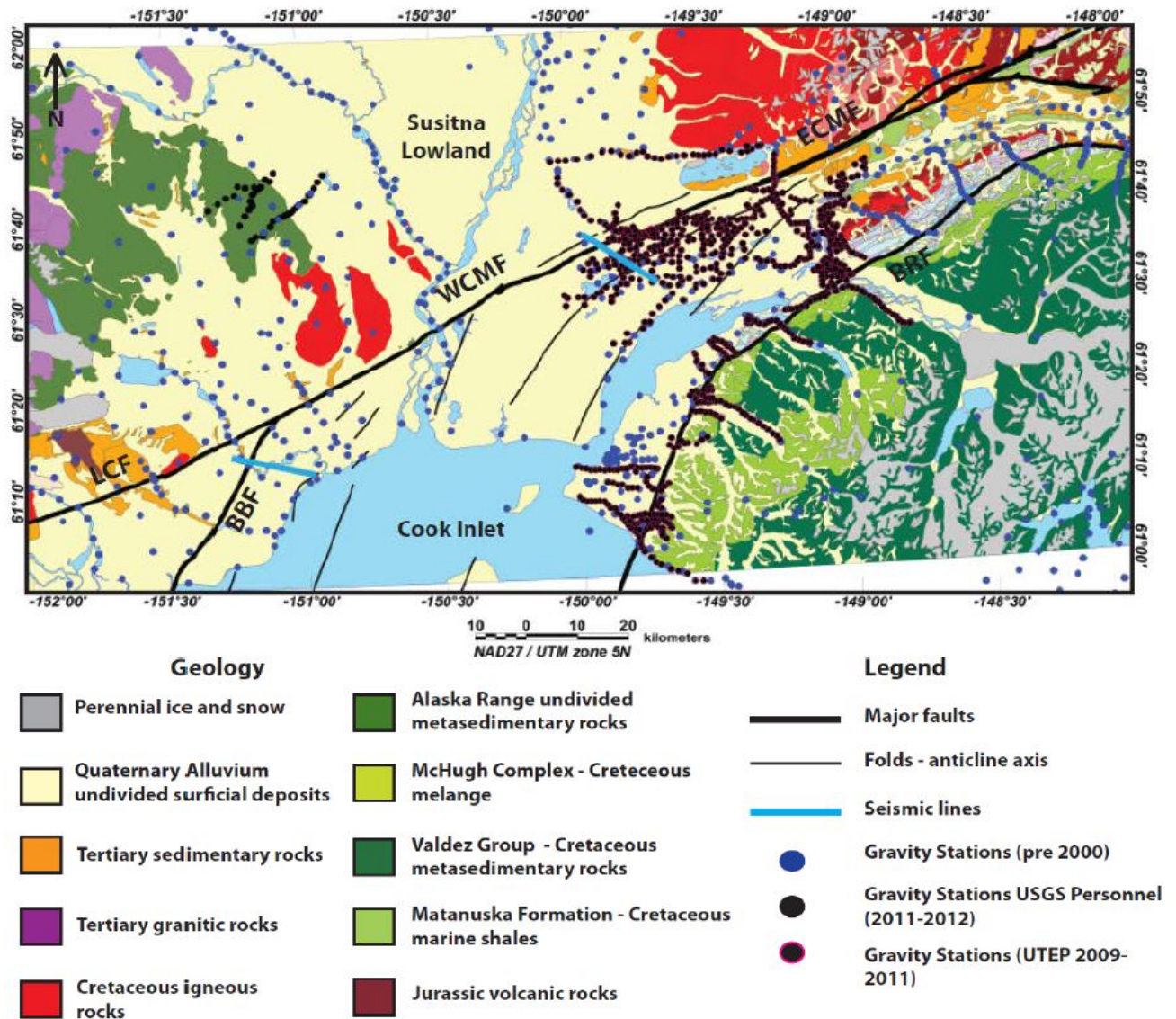


Figure 2. Geologic map of the Castle Mountain Fault and Matanuska-Susitna study area showing locations of all gravity measurements (simplified from Wilson et al., 2009). WCMF and ECMF are western and eastern Castle Mountain Fault. BRF is Border Ranges Fault, LCF is Lake Clark Fault, BBF is Bruin Bay Fault. NAD-North American Datum; UTM-Universal Transverse Mercator. Fault and fold data are digitized from Haeussler et al. (2000).

### 1.3 TECTONIC AND GEOLOGIC SETTING

Anchorage is Alaska's most populated city and is located in a zone of oblique subduction between the North American and Pacific Plates (Figure 1). Collision of the Yakutat microplate with North America complicates regional subduction resulting in a shallow dipping slab (approximately 3 degrees) beneath south central interior Alaska (e.g., Brocher et al., 1994). Regional folding and faulting occur in the upper crust as a result of oblique subduction in the Anchorage area. The most active (Neogene/Quaternary) crustal structures are concentrated between the Castle Mountain-Bruin Bay fault system and the Border Ranges fault (Figure 3) (e.g. Haeussler et al., 2000). Studies along these structures suggest that 2 to 6% of cumulative North American/Pacific Plate convergence may be accommodated within the crust (Doser et al., 2004) through a combination of strike-slip and reverse faulting and folding.

The Castle Mountain fault (CMF) is located south and east of Quaternary volcanic centers and above the Aleutian megathrust (Haeussler et al., 2014). The CMF trends northeast within an active forearc basin system defining the southern margin of the Susitna basin and the northern margin of both the Cook Inlet Basin (CIB) and Matanuska Valley (Figure 3).

The Susitna Basin is an extension of the CIB (Rouse and Houseknecht, 2012; Craddock et al., 2014), and forms a broad lowland with minimal outcrop consistent with an actively subsiding basin. Scarcity of subsurface data have handicapped understanding of its stratigraphic and geologic history (Merritt, 1986). The CIB basin is bounded approximately by two major fault systems: the Bruin Bay fault to the west and the Border Ranges Fault System (BRFS) to the east (Figures 2 and 3). The Matanuska Valley is an exhumed remnant of part of the Mesozoic-Paleogene forearc basin, exposing a deformed section of Jurassic to Eocene sedimentary rocks (Trop et al., 2005). The Alaska Range and Talkeetna Mountains, located northwest and northeast of the CMF respectively,

represent mostly Mesozoic granitic arc rocks (Figure 2) while the Chugach Mountains to the southeast consist primarily of Permian to Eocene strata deformed in a Mesozoic subduction complex. This subduction complex is comprised of two major lithotectonic assemblages: the older Chugach mélange assemblage, and the younger metasedimentary rocks known as the Valdez Group. (Tysdal and Plafker, 1978; Pavlis and Roeske, 2007).

Extensive Quaternary glacial deposits cover most of the lowlands of the CMF area. These undifferentiated glacial deposits unconformably overlie Late Eocene to Late Pliocene sedimentary rocks known as the Kenai Group within the CIB (Fig. 1; Hauessler and Saltus, 2011). Borehole data reveal that the Kenai Group contains cross-bedded to massive sandstones, siltstones, and shale with an estimated total thickness of ~2km near the basin axis (e.g., Plafker et al., 1989). Five nonmarine formations are recognized within the Kenai group, including the Sterling, Beluga, Tyonek, Hemlock, and West Foreland Formations which overlie late Mesozoic sequences (Swenson, 1997). The late Mesozoic sequences are recognized as a succession of shallow-marine rocks of Middle Jurassic-Cretaceous age with an approximate thickness of ~8500m. These sedimentary deposits collectively define the forearc basin stratigraphic sequences that cover Early Jurassic volcanic and intrusive assemblages of the Peninsular terrane basement rocks.

The Border Ranges mafic/ultramafic assemblage (BRUMA), is identified among the Peninsular terrane basement rocks along the eastern CIB boundary (Burns, 1982; Debari and Coleman 1989; Plafker et al., 1989). The BRUMA primarily represents plutonic rocks ranging in composition from gabbro to tonalite with associated ultramafic bodies (e.g., Burns, 1982; Plafker et al., 1994) and is widely interpreted as a fragmented crustal section of an Early Jurassic oceanic arc system (e.g., Burns, 1982; Plafker et al., 1989; Pavlis and Roeske, 2007).

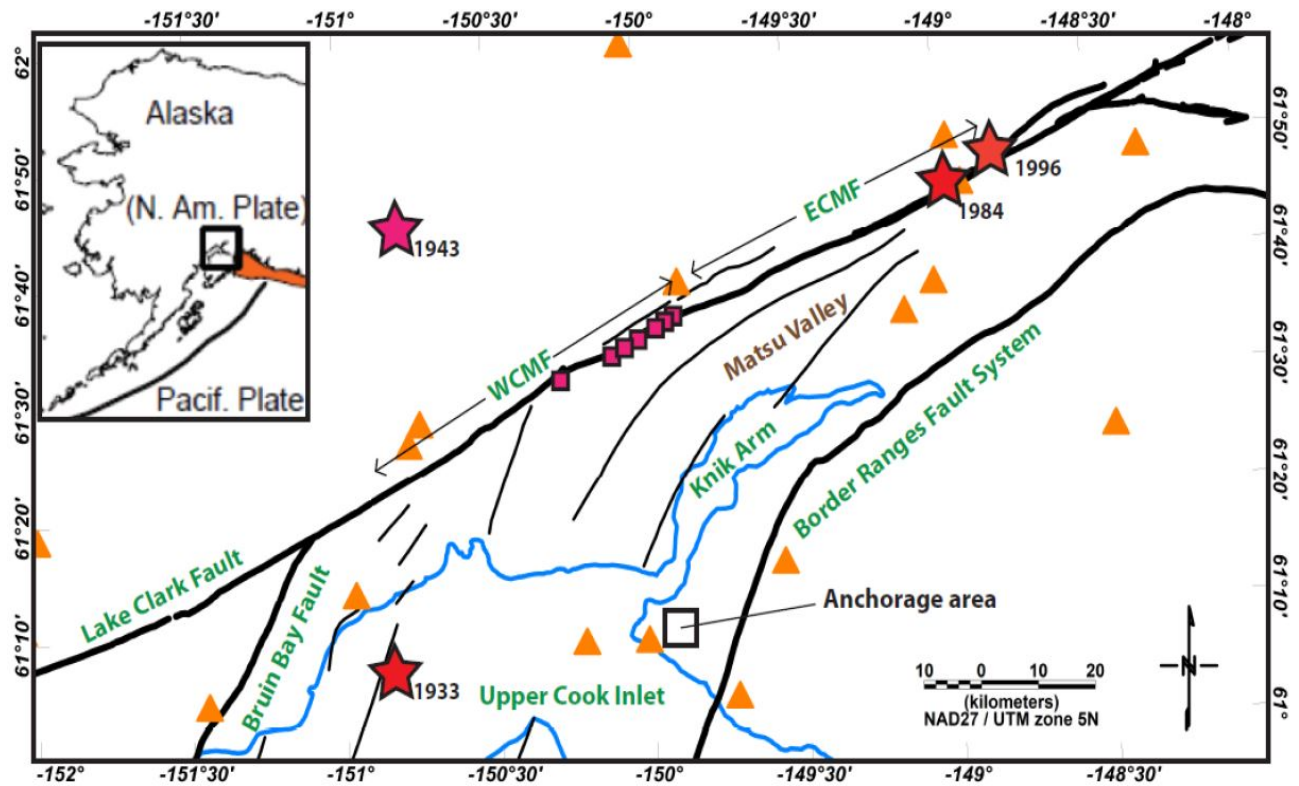


Figure 3. Map of study area showing major faults (bold black lines) and folds (thin black lines) from Haeussler et al. (2000) and Haeussler and Saltus (2011). Pink squares along WCMF are locations of previous trenching studies. Inset map at upper left shows location of study area in Alaska with respect to major tectonic plates and Yakutat microplate (offshore portion in orange). Bold black line in inset map is the Aleutian trench. Stars indicate important earthquakes discussed in text. Black open square is location of Anchorage. Orange triangles are seismograph stations.



## 1.4 PREVIOUS STUDIES

The Castle Mountain Fault is the only fault in the Anchorage region showing consistent evidence for repeated Holocene movement (Haeussler et al., 2000). Geological and seismological studies reveal that four significant earthquakes have occurred on the CMF over the past ~2700 years, and that the CMF remains capable of generating magnitude 6 to 7 earthquakes (Haeussler et al., 2000). The average recurrence interval for earthquakes along the CMF is estimated to be 700 years, with approximately 600 to 700 years having passed since the last high magnitude event occurred along this fault (Haeussler et al., 2000). Additional studies report fault slip rate estimates of 0.27 to 0.32 cm/yr along the western portion of the CMF (Willis et al., 2007). These estimates indicate that 1.6 to 2.2m of slip has built up along the fault since the last event (enough to generate a magnitude ~7 event). While the eastern portion of the CMF shows no direct evidence of Holocene faulting, moderate earthquakes have occurred along this part of the fault in 1984 ( $M_w = 5.7$ ) (Lahr et al., 1986) and in 1996 ( $M_L = 4.6$ ) (Figure 3). Paleoseismic data indicate that the timing of earthquakes along the western portion of the CMF is similar to that of events along the plate interface, suggesting a possible link between the megathrust and crustal faults located within the study area (Haeussler et al., 2002). Since the east and west strands of the fault have different current and past seismic behavior, developing a new geophysical model of the CMF area is crucial to better understanding the structure along the fault and its seismological impact on the Anchorage region. Previous geophysical studies along the CMF have been limited to analysis of a seismic reflection line crossing the eastern end of the western CMF (Figure 1), gravity data, magnetic data, and regional borehole information. Seismic reflection data reveal long-wavelength open folds deforming early to middle Miocene strata southeast of the CMF's surface trace (Haeussler et al., 2000). This particular fault zone is a complex area of faulting and folding at least 3km wide which

is interpreted as a flower structure (Haeussler et al., 2000). Gravity gradient from previous gravity studies (Hackett, 1977b), revealed the high angle reverse component of the CMF.

A number of geologic studies have shown that the CMF displays a notable change in geomorphic expression along its trace. The western ~60km portion of the fault (Figure 3) displays linear, mostly south facing, and right-stepping scarps up to 2m high that cut late Quaternary glacial and fluvial deposits associated with the Susitna and Little Susitna Rivers. Numerous liquefaction features are located along the western CMF (Haeussler et al. 2002). In contrast, no evidence for Holocene faulting is detected along the eastern part of the CMF (Detterman et al., 1976; Haeussler, 1994) even though this portion of the fault is associated with recent seismicity (Lahr et al., 1986; Flores and Doser, 2005). The sense of slip on this segment of the fault has also been debated.

Bruhn and Pavlis (1879?) used fault slip data from exposures of the fault to suggest that Neogene slip was dominantly reverse motion. In contrast (there are other more recent studies)

Adjacent to the CMF, the Upper Cook Inlet area contains the highest concentration of Neogene reverse faults and folds within the region. These structural features are likely a result of positioning above the southwestern edge of the subducting Yakutat microplate (Figure 6) that focuses transpressional deformation (Haeussler and Saltus, 2011). Many of the structures, however, originated in the Paleogene (e.g. Bruhn and Pavlis, 1979; Trop et al, 2005; Pavlis and Roeske, 2007), complicating a single interpretation for the specific structures

Flores and Doser (2005) identified numerous shallow, seismically active features (likely faults or fault-cored folds) located close to Anchorage and the CMF. A subset of 4200 shallow earthquake relocations (<20km) occurring between 1964 and 1999 is shown in Figure 4a. More recent events, occurring between 2000 and 2014, were then taken from the Alaska Earthquake Information Center (AEIC) catalog and compared to those occurring between 1964 and 1999 (Figure 4b). By

comparison, it is evident that prominent regions of seismicity observed between 1964 and 1999 continue to be active through 2000 – 2014.

Seismicity between Upper Cook inlet and the western CMF is consistent with reverse motion along faults coring mapped folds, such as the Bell Island anticline (BI box, Figure 4a). Just north of the junction between the CMF and the Bruin Bay fault, a NNW striking band of seismicity is observed (Talachulitna region, TL, Figure 4a). Seismicity patterns along this fault suggest a northeast dipping fault (Flores and Doser, 2005). Two focal mechanisms from the AEIC catalog occurring within this region are also consistent with eastward dipping reverse faulting.

Figure 5 shows a cross section of the seismicity along the eastern CMF (magenta NE trending rectangle, Figure 4a). Events occurring within 10 km of the fault were projected onto this cross section. The dashed rectangle on the cross section encloses aftershocks of the 1984 Sutton earthquake. The Sutton sequence corresponds to considerably deeper seismicity (15-20 km). Shallow events appear on both sides of the 1984 Sutton Sequence. Along-strike changes in earthquake depth may be controlled by variations in bedrock geology along the fault. The deeper seismicity near Sutton suggests that the seismogenic width of the CMF could be greater than that of other Alaskan crustal faults, such as the Denali (~12 km, Ratchkovski et al., 2003) fault. This suggested seismogenic width has important implications for estimating the maximum credible earthquake and strong ground motion expected from the CMF.

In 2010 and 2011 UTEP students collected over 700 gravity data points along numerous transects across the Border Ranges Fault System (BRFS) and the CMF (Figure 2). This data was used by Mankhemthong et al., (2013) to model 2D geometries of the Border Range Fault System (BRFS), the Border Range Ultramafic and Mafic Assemblages (BRUMA) and other forearc boundary structures extending across the CMF. Comparing a simple Bouguer gravity anomaly map (Figure

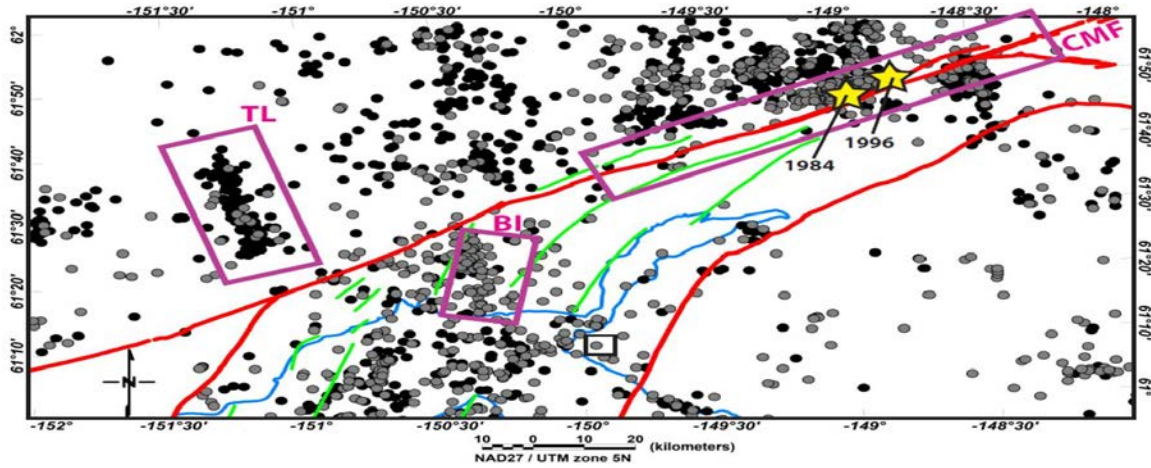
6) produced from the gravity data with earthquake relocated events from Flores and Doser (2005) shows an increase in seismicity along the CMF associated with a gravity high north of the fault. South to the CMF in figure 6 is a long wavelength gravitational low, extending through Upper Cook Inlet and ending near the inferred southwestern edge of the Yakutat microplate (dashed white line, Figure 6), is interpreted as the extension of a mid-crustal serpentinite body previously imaged by Saltus et al. (2001) in middle Cook Inlet (Mankhemthong et al., 2011; Mankhemthong et al., 2012c). Mankhemthong et al., (2012c) modeled the gravitational low located east of Knik Arm as due to underplated sediment from subduction of the Yakutat microplate. Two cross sections showing an interpretation of these deeper, longer wavelength features using gravity and magnetic data are shown in Figure 8.

The relationship between aeromagnetic data from Saltus et al. (1999) and relocated seismicity (Flores and Doser, 2005) is shown in Figure 7. A strong magnetic high ( $>200\text{nT}$ ) along the eastern edge of Upper Cook inlet is related to the highly magnetized rocks of the Border Ranges ultramafic and mafic assemblage (BRUMA). An extension of a mid-crustal serpentinite body modeled by Saltus et al. (2001) appears to be causing a moderate magnetic high ( $100\text{nT}$ - $200\text{nT}$ ) within Cook Inlet. Flores and Doser (2005) proposed a connection between the concentrated seismicity in Cook Inlet and the location of the serpentinite body. While much of seismicity associated with the CMF occurs in a magnetic low, seismicity in the Talachultina region is located within a magnetic high (Figure 7).

Preliminary 2-D models based on modeling of long wavelength signals in the regional gravity and magnetic fields are shown in Figure 8 (locations of cross section lines E-E' and F-F' are shown in Figure 7) (Mankhemthong et al., 2011; Mankhemthong et al., 2012c). These models will serve as

a starting point for more detailed modeling of the crustal and upper mantle structure the CMF region (including Upper Cook Inlet and the Matsu Valley) within this study.

a) 1971-1999 (relocated)



b) 2000-2014 AEIC catalog

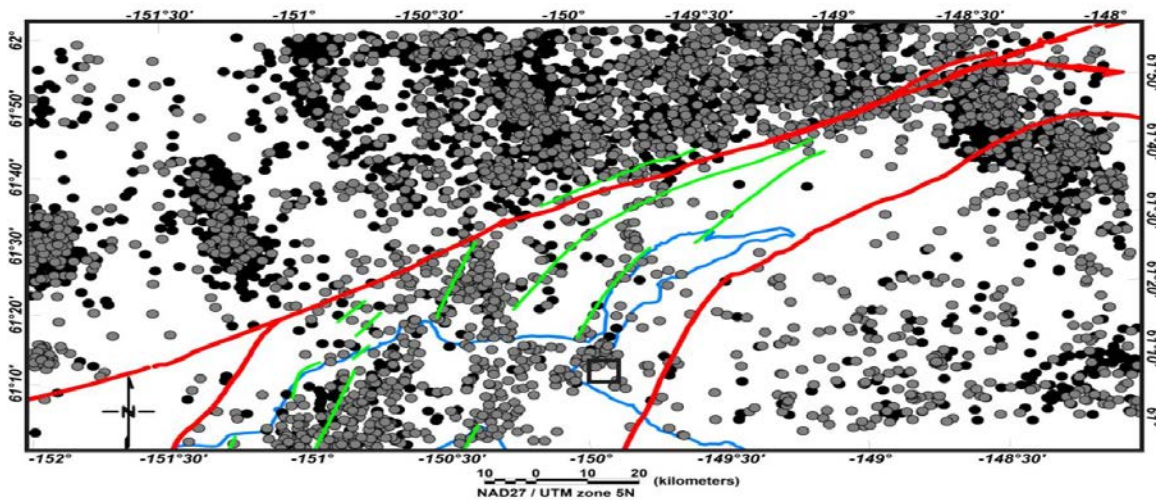


Figure 4. Seismicity of the study area. Black circles are events with depths <10 km and gray circles are events with depths of 10-20 km. All black and gray symbols are  $M < 5$  events. **a)** Magenta boxes indicate regions of intense seismicity related to the Castle Mountain fault (CMF), an unnamed fault in the Talachulitna region (TL) and Bell Island anticline (BI). The box labeled CMF is shown in cross section in Figure 5. Stars are the 1984 Sutton and 1996 eastern CMF earthquakes. **b)** AEIC catalog seismicity between 2000 and 2014.

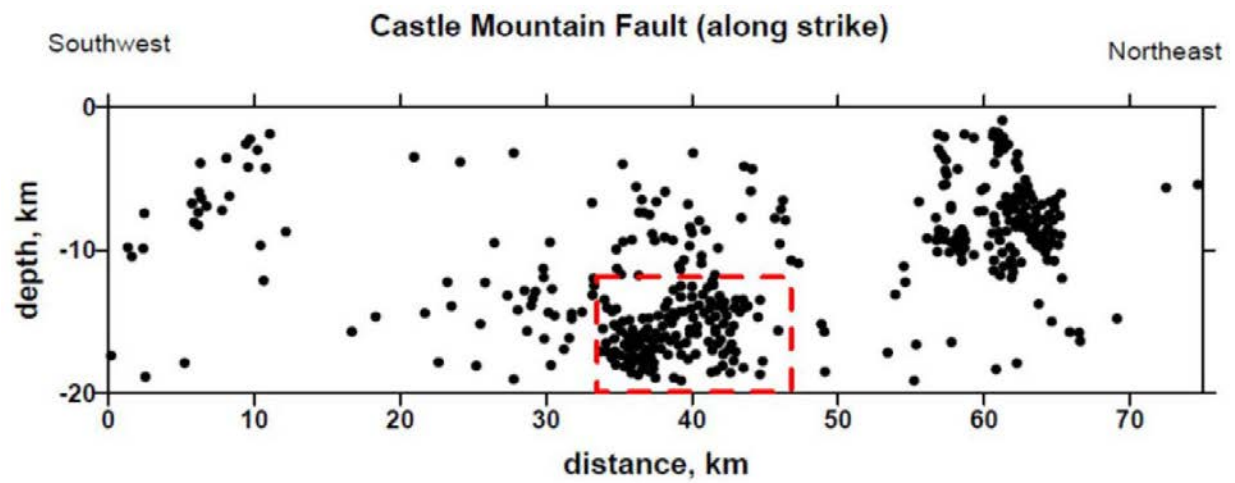


Figure 5. Cross section of seismicity along the Castle Mountain fault (see magenta rectangle in Figure 4a for location). Rectangle contains aftershocks of the 1984 Sutton Sequence.

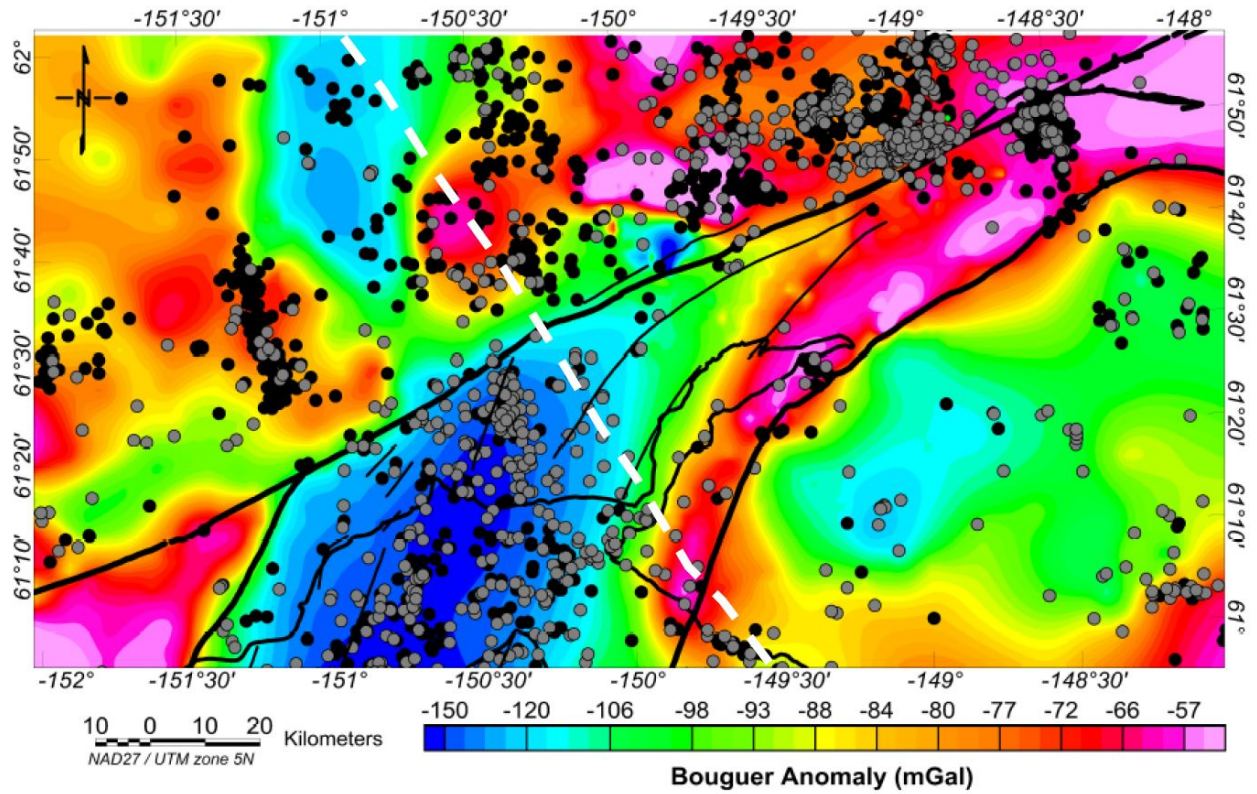


Figure 6. Bouguer gravity anomaly map of study area with relocated seismicity. Black circles are events with depths <10 km and gray circles are events with depths of 10-20 km. Pink indicates zones of high gravitational anomalies while blue indicates zones of low gravitational anomalies. Dashed white line is the inferred southwestern edge of the Yakutat Microplate from Ebert-Phillips et al. (2006).



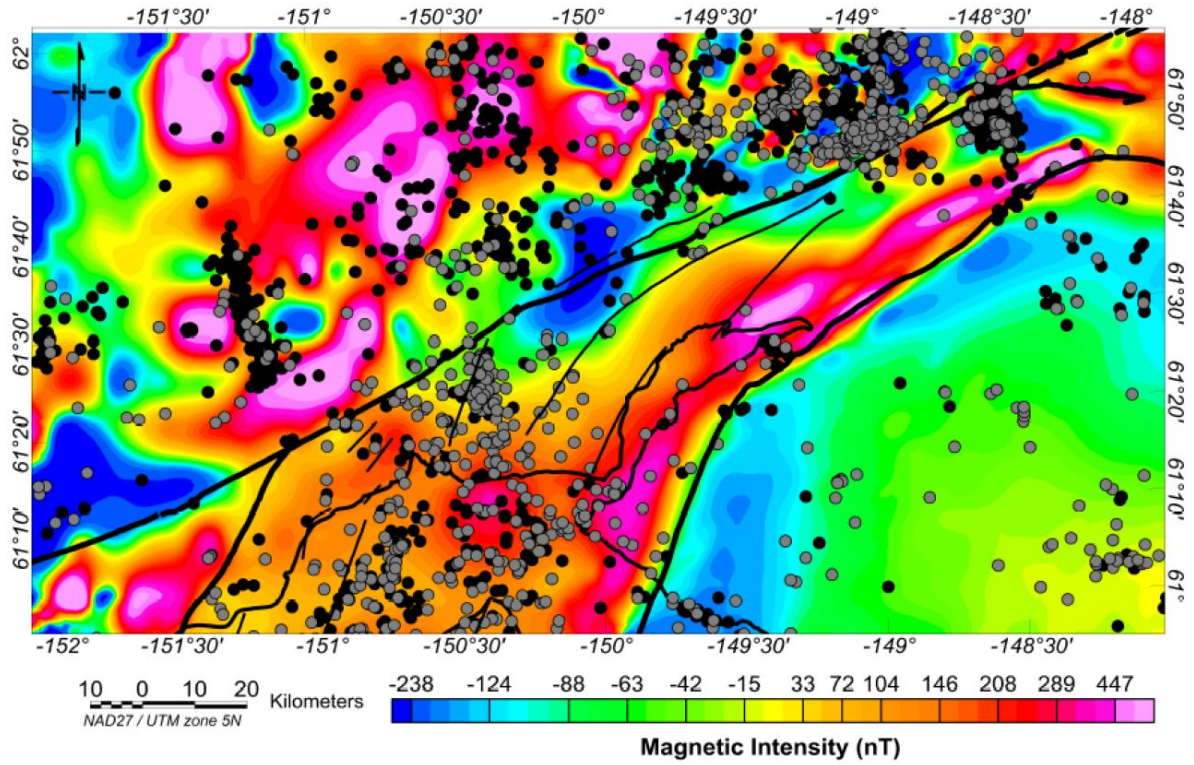


Figure 7. Aeromagnetic map of study area with relocated seismicity. Black circles are events with depths <10 km and gray circles are events with depths of 10-20 km. Pink indicates zones of high magnetic intensity while blue indicates zones of low magnetic intensity. Aeromagnetic data from Saltus et al. (1999).

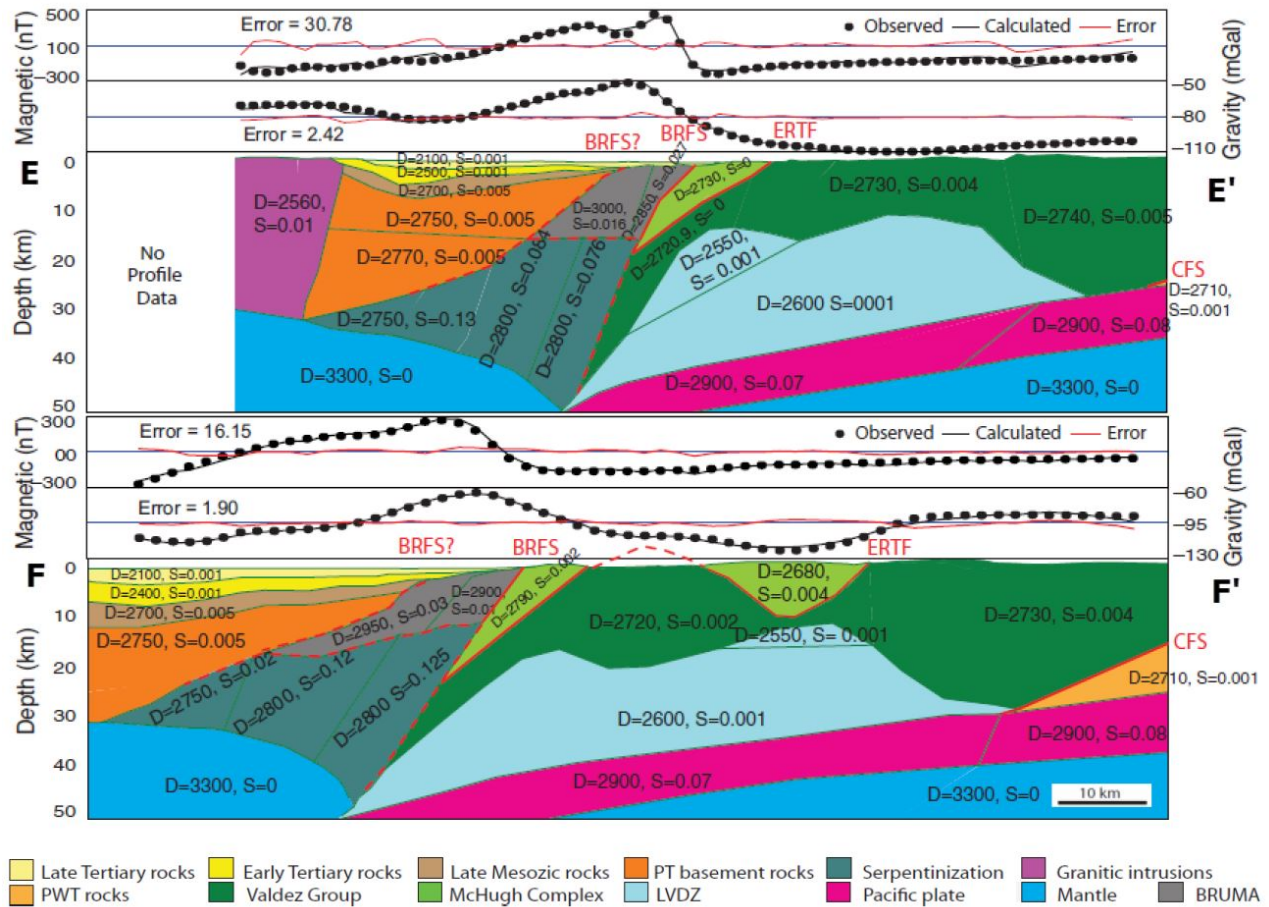


Figure 8. Structural models based on 2.5-D modeling of gravity and magnetic data for the study area (see location of cross sections in Figure 9). Solid red lines indicate known faults that extend to surface. The BRFS is the Border Ranges fault system; CMF is the Castle Mountain fault; ERTF is the Eagle River thrust fault. D is density and S is magnetic susceptibility. Profiles are vertically exaggerated by a factor of 0.4.

## **1.5 METHODOLOGY**

### **1.5.1 GEOPHYSICAL DATA**

We used over 1600 gravity data points to map gravity changes caused by density contrasts across the study area ( $-148^{\circ}$  to  $-152^{\circ}$  longitude and  $61^{\circ}$  to  $62^{\circ}$  latitude) (Figure 9). About 700 of these data points were collected and processed between 2010-2011 by Mankhemthong et al. 2013. The 2010-2011 data were tied to established local absolute gravity stations and corrected to simple Bouguer anomalies. A standard density of  $2670 \text{ kg/m}^3$  was applied for the Bouguer correction to remove the gravity slab effect (Burger et al., 2006). These data were combined with existing gravity data collected by USGS personnel over the western Susitna basin (black closed circles, Figure 9) during the summers of 2011 and 2012 (R. Saltus, pers. commun., 2014) in addition to existing regional U.S. Geological Survey databases collected before 2000.

We utilized aeromagnetic data (compiled and reprocessed from Saltus and Simmons, 1997) to map magnetic intensities corresponding to the distribution of magnetic material and structural features within the study area (Figure 10). These data were extracted from four separate surveys conducted between 1954 and 1977. Flight directions (north-south and east-west), altitudes (120-760 m), and flight line spacings (1600 m to 16,000 m), varied across surveys. Thus, we applied upward or downward continuation corrections and converted from level to drape as necessary. The original survey grids were adjusted to minimize differences at the boundaries resulting in a consistent survey specification of 305 m above ground (Saltus and Simmons, 1997). A reduction to pole filter was applied to the total intensity aeromagnetic data in order to eliminate lateral shift or distortion that might be caused if the magnetization and the ambient field are not both directed vertically (Blakely, 1995). Inclination and declination values of  $73^{\circ}$  and  $25^{\circ}\text{E}$  are presumed values corresponding to the 1954-1977-time interval (Saltus and Simmons, 1997).

### **1.5.2 GRAVITY AND MAGNETIC ANOMALY MAPS**

Reduced gravity and aeromagnetic anomaly maps were created using Geosoft Oasis Montaj software (Figures 9 and 10). Maps were gridded with the same 1000 m grid interval using a minimum curvature interpolation technique. Anomaly gradients were compared with known and inferred geologic features and relocated seismicity (Figures 4a and 4b).

### **1.5.3 GRAVITY ANOMALY INTERPRETATIONS**

The most prominent features of the study area are the gravity lows related to the CIB, Susitna Lowland, and the Chugach Mountains, and the gravity highs associated with the BRUMA, Talkeetna Mountains, and various igneous plutons located north and southwest of the CMF (Figure 9).

The deepest gravity lows (-120 to -150 mGal) correspond well with the CIB boundaries and trend northeast along the basin axis. A northwestern oriented gravity low trends narrowly away from the western portion of the CMF broadening eastward toward the northern portion of the Susitna Lowland. The Susitna Lowland anomaly is bordered by gravity highs to the west and east. Gravity lows occurring within the Chugach Mountains are possibly related to underplated sediments linked to the southwestern edge of the subducted Yakutat microplate (Mankhemthong et al., 2013). The largest gravity highs (>50 mGal) occur within the Talkeetna Mountains just north of the eastern portion of the CMF in a zone of thicker metamorphic and igneous rocks.

Gravity highs are also found in a belt along the eastern margin of the CIB trending sub-parallel to the BRFS. This belt likely represents subsurface high-density rocks of the BRUMA as modeled by Mankhemthong et al., 2013.

Strong gravity gradients occur at the northwestern edges of the CIB corresponding to the locations of the Bruin Bay and Castle Mountain faults (Figure 9). These anomalies are associated with fault juxtapositions of higher density crystalline rocks against lower density sediments of the basin. The CMF appears to be associated with 2 prominent gravity gradients between the CIB and Susitna Lowland, and between the western and eastern portions of the fault. These gradients appear to mark transitional zones from low density forearc basin deposits to high density igneous and metamorphic plutonic zones associated with the surrounding Talkeetna Mountains.

#### **1.5.4 MAGNETIC ANOMALY INTERPRETATIONS**

The CMF area displays a prominent northeast striking magnetic high related to the Cook Inlet basin. This magnetic high is closely correlated to where gravity anomalies are lowest (Figure 10). The magnetic anomaly represents an abnormal feature for basin fill and is known as the Alaska Magnetic High. Saltus et al. (2001) interpreted this zone as the product of fluid serpentinization of altered lower forearc crust and/or mantle at 16-34 km depth. Magnetic highs located to the west of the CIB and directly north of the lower western segment of the CMF are likely related to intrusive and extrusive bodies associated with the active volcanic arc (Saltus et al., 2001) occurring in areas with strong gravity highs (Figure 10). The BRUMA magnetic high anomaly borders the eastern flank of the CIB sub-parallel to the BRFS in the Matanuska valley area and correlates well to strong gravity highs (Figure 10). This feature is clearly a response from Jurassic mafic to intermediate plutonic rocks that exposed throughout the area where the magnetic anomaly is seen over exposed rocks in the northern Chugach Mountains (Burns et al., 1991). Ultramafic bodies at Eklutna and Wolverine also contribute to this anomaly, but these bodies are too small to account for the regional anomaly. Intense magnetic lows over the topographically high Chugach terrane

suggest fewer and/or no magnetic source rocks within the accretionary complex (e.g., Saltus et al., 2007), consistent with exposures of metamorphosed turbidites that comprise this region.

Strong magnetic highs also occur north of the western CMF and likely correspond with both outcropping and buried plutons within the Susitna Lowland area (Figures 2 and 10). A strong magnetic gradient occurs across the western to eastern portions of the CMF and is visible on the unfiltered and Low pass filter maps. Low pass filtering analysis indicates long-wavelength magnetic lows suggesting deeper causative bodies along this part of the CMF. This feature occurs within the middle of the CMF and could be a deep structure transitional zone related to the southwestern edge of the subducting Yakutat block (Figure 6). These anomalies correlate well with highly magnetized igneous and metamorphic zones located within the Talkeetna Mountains.

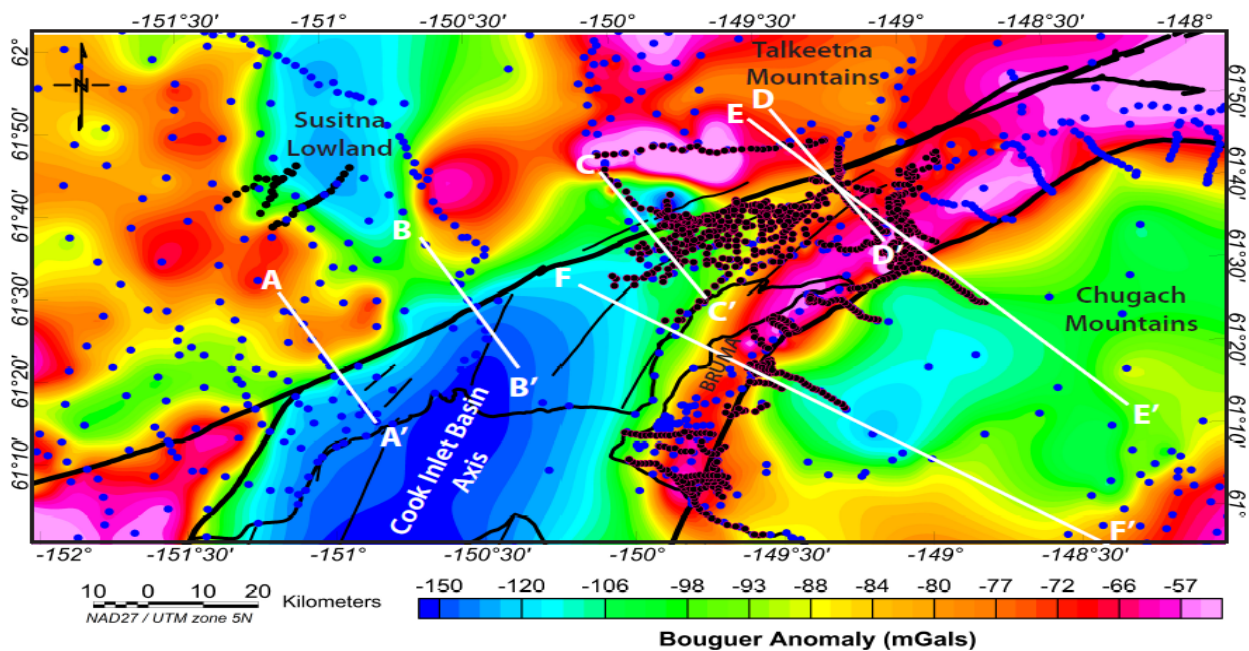


Figure 9. Simple Bouguer anomaly map gridded at 1000 m. White lines A-A', B-B', C-C', and D-D' are locations of 2D integrated gravity and magnetic models analyzed in this study arranged west to east along the Castle Mountain fault. Lines E-E' and F-F' are locations of gravity and magnetic models constructed by Mankhemthong et al., 2013. BRUMA is the Border Range ultramafic and mafic assemblages.



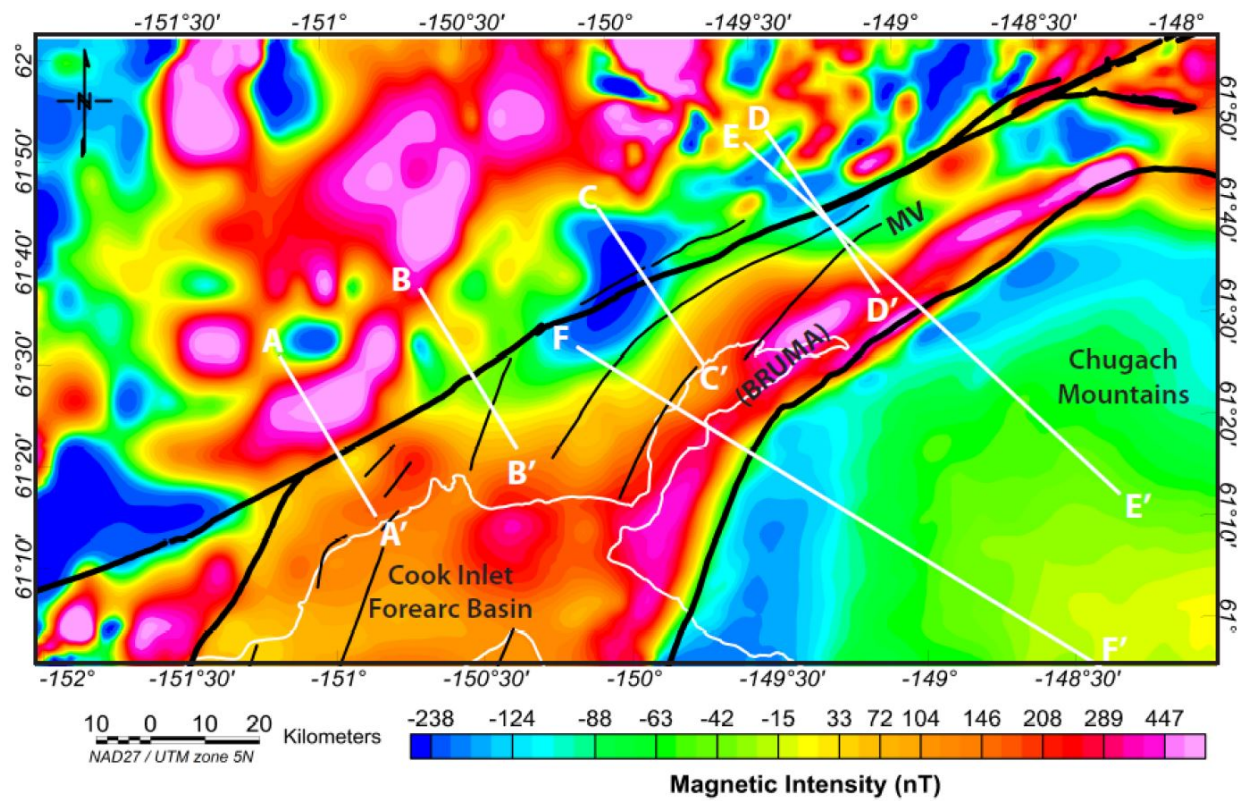


Figure 10. Total intensity aeromagnetic map gridded at 1000 m. White lines show location of 2D integrated gravity and magnetic profiles analyzed in this study. BRUMA - Border range ultramafic and mafic assemblages. MV - Matanuska Valley.

### 1.5.5 DATA CONSTRAINTS FOR 2D FORWARD MODELS

Geosoft GM-SYS modeling software was used to create 2D forward models of the geologic structure across the Castle Mountain Fault. Four parallel transects (profiles A-A', B-B', C-C', and D-D') were selected for the 2D forward modeling shown in Figure 9. All profiles are approximately 32 km in length trending perpendicularly across the CMF in a northwest to



southeast direction. Profiles A-A' and B-B' cross the western CMF from the southern Susitna Lowland to the northwestern CIB. Profiles C-C' and D-D' cross the eastern CMF from the southeastern Susitna Lowland/Talkeetna area to the northeastern CIB/Matanuska Valley area. Structures were modeled to a depth of ~50 km and assuming homogeneous bodies extending orthogonal to the profiles to distances of infinity ( $\pm 30,000$  km).

The modeling software requires reasonable initial estimates of model parameters such as topography, depth, subsurface body shape, density, and magnetization of potential sources. Geologic maps from the U.S. Geological Survey data base compiled by Wilson et al. (2009) were used for geologic contacts and fault constraints. Topographic constraints were applied using digital elevation models from the National Elevation Data set (last updated by Gesch et al., 2002; Gesch, 2007). Geophysical cross-sections from Mankhemthong et al. (2013), Ehm (1983), Shellenbaum et al. (2010), and Li et al. (2013) were used to guide initial depth and thickness estimates for shallow and deep geologic features represented in the 2D models.

Table 1 from Mankhemthong et al. (2013) provides information on subsurface density and magnetic susceptibility variations used in the 2D forward models. Existing profiles E-E' and F-F' created by Mankhemthong et al. (2013) were used as starting models to guide the 2D forward modeling process. All densities and magnetic susceptibilities correspond with Table 1.

Table 1: Densities and Magnetic Susceptibilities used in 2D Forward Modeling

Model bodies	Densities (kg/m <sup>3</sup> )	Data sources	Magnetizations (SI)	Data sources
BRUMA	2900–3000	FV, SH	0.030–0.063	A
Basement rocks of Peninsular terrane	2700–2750	FV, EP, SG	0.005 <sup>†</sup> , 0.027*	SH <sup>†</sup> , Sb*
Granitic intrusions	2500–2700	SH, A	0.010	A
Late Mesozoic rocks	2670–2700	FV	0.005 <sup>†</sup> , 0.027*	A <sup>†</sup> , SH <sup>†</sup> , Sb*
Underplated sediments	2550–2600	FV, Y	0.001	A
Early Tertiary sedimentary rocks	2400–2500	DL, SH	0.001	A
Mantle	3300	Sb	0.000	Sb
McHugh Complex of Chugach terrane	2700–2740	HS, NP	0.001–0.006	A, Sa
Accretionary rocks of Prince William terrane	2600–2700	FV	0.002	SG
Serpentinization	2750–2800	FV, SH	0.03–0.13 <sup>†</sup> , 0.04–0.09*	CM <sup>†</sup> , Sb*
Subducting Pacific plate	2900–3000	Y	0.07–0.09	Sb, SH
Late Tertiary sedimentary rocks	2100–2200	DL, SH	0.001	A, Sa
Valdez Group of Chugach terrane	2690–2720	HS, NP	0.001–0.006	A, Sa
Volcanic arcs	2800	FV, EP	0.025	A
Yakutat microplate	2850	FV	0.017	A

*Note:* Data source abbreviations: NP—calculated from the Nettleton-Parasnis inversion method (Mankhemthong et al., 2012); FV—converted from seismic tomography data (Fisher and von Huene, 1984); Y—converted from seismic tomography data (Ye et al., 1997); EP—converted from seismic tomography data (Eberhart-Phillips et al., 2006); HS—measured from rock hand samples; DL—determined from density logs; SH—based on Saltus and Haeussler (2004); SG—based on Sanger and Glen (2003); A—based on Altstatt et al. (2002); Sa—based on Saltus et al. (2005); CM—based on Carlson and Miller (2003); Sb—based on Saltus et al. (2007).

## 1.6 RESULTS AND INTERPRETATION OF 2D MODELS

The 2D profiles (A-A', B-B', C-C' and D-D', Figures 11 to 14) are developed using initial models with information on rock type, density and susceptibility (figure 8) developed by Mankhemthong et al. (2012). The results of the 2D models show layers of Tertiary and Late Mesozoic sedimentary rocks similar to models developed by Mankhemthong et al. (2012). The upper part of the models shows thick sections of Early and Late Tertiary sedimentary rocks to a maximum range of ~6 km (Figure 11, profile A-A') to ~4 km (Figure 14, profile D-D'). The CMF is modelled in the profile by comparing surface mapped locations of the fault from Haeussler et al. (2000) and sharp magnetic and gravity anomaly gradient across the profiles. The CMF (Figure 12, profile B-B') shows a high angle, reverse, north-side up displacement with the fault cutting through late Mesozoic sedimentary rocks (Figures 12 and 13, profile B-B' and C-C'). The northwestern edge of the Mesozoic sedimentary rock also forms a fault contact with Cretaceous igneous rocks. This Cretaceous igneous rock was modelled to correspond with surface exposure shown on geologic maps, gravity and magnetic anomaly changes across the profiles. Thick sections (~44 km) of the Cretaceous rocks are modelled at west and eastern ends (profiles A-A' and D-D') of CMF and thin (~18 km) close to the Holocene fault scarp (profile B-B'). The Cretaceous igneous rocks are modelled with susceptibility in the range of 0.02 to 0.032 on the WCMF (profile A-A') against a 0.012 to 0.015 susceptibility values in profiles B-B' and D-D'. The Cretaceous igneous rock shares an intrusive contact with the Peninsula-Terrane (PT) basement rocks (Profile A-A', B-B' and D-D'). The thickest section of the PT basement rock is ~30 km (Profile A-A' to C-C') and a thin section ~ 26 km (Profile D-D'). Far southeast of profiles A-A' and B-B' is a modelled serpentinized body with density of 2800 kg/m<sup>3</sup> and susceptibility of 0.08 (Profiles A-A' to C-C'). The section was modelled to constrain the changes in magnetic and gravity anomalies and correlate

2D models from Mankhemthong et al. (2012). It thickens toward the ECMF with susceptibility varying from 0.076 to 0.135 SI in profile D-D'. Towards the ECMF the Border Range Ultra-Mafic Assemblage (BRUMA) block is added to profiles C-C' and D-D' to match the high gravity anomaly and surface exposure in the northern Chugach Mountain fronts. The BRUMA is modelled on top the Serpentinized body with a density of  $3000 \text{ kg/m}^3$  and a susceptibility of 0.027 SI. The maximum thickness is ~14 km (profile C-C') and thins to ~7 km (profile D-D'). The subducting Yakutat microplate is modelled as a low velocity density zone (LVDZ) to a maximum thickness of ~14 km (D-D'). The density of LVDZ is  $2600 \text{ kg/m}^3$  and the susceptibility is 0.001 SI. The LVDZ sits atop the low angle subducting Pacific plate with density of  $2900 \text{ kg/m}^3$  and a susceptibility of 0.07 SI. The Moho is mapped at depth in the range of ~38 to 44 km. Seismic events plot along the profiles indicating higher seismicity (B-B', C-C' and D-D') towards the ECMF. Profiles B-B', C-C' and D-D' are dominated by deep crustal and intermediate seismic events. Shallow crustal events mainly occur within the Talkeetna Mountains (D-D'). Shallow seismic events are plotted along the mapped fault plane on the WCMF (Profile A-A' and B-B'). Folds and faults of Mesozoic sedimentary rocks (profiles A-A' and D-D') are consistent with location and extent as mapped by Detterman and others (1974, 1976a), Clardy (1974) and Haeussler (1998). A modelled Mesozoic anticline (Profile A-A') which fits the gravity and magnetic signature is well aligned with strike orientation of Ivan River anticline. I interpret the anticline as a southwestern continuation of the Ivan River anticline. Cretaceous rocks mapped in profile A-A' are located on the southwestern rim of the Susitna basin and coincide with igneous rocks of the Susitna and Beluga Mountains as modelled by Saltus et al. (2016). The variation in susceptibility and density of the Cretaceous igneous rocks is likely associated with the process of magma mixing. The location and extent of CMF is consistent with location mapped by Detterman

et al. (1974, 1976a), Clardy (1974) and Haeussler (1998) and shows high angle reverse fault. The depth to moho mapped for the models are within previously estimated range of ~32 to 60 km (e.g Ambos et al., 1995; Eberhart-Phillips et al., 2006; Romero, 2011; Miller et al., 2018). The average thickness of Tertiary sedimentary rocks at the northern CIB (~5 km) is less than estimated 8 km suggested by LePain et al. (2013) which is a likely expected estimate for the outer margin of the basin. The region of high seismicity within the vicinity of CMF are in the margin or the path the Yakutat microplate. This collision and subduction of Yakutat microplate produces stress buildup that causes deformation within of the crust. Active seismicity is located within the Cretaceous igneous rocks. Seismic lineament is identified along the ECMF (profile A-A' and B-B') which supports the mapped location of the fault and provides a possibility of the depth extension of the fault.

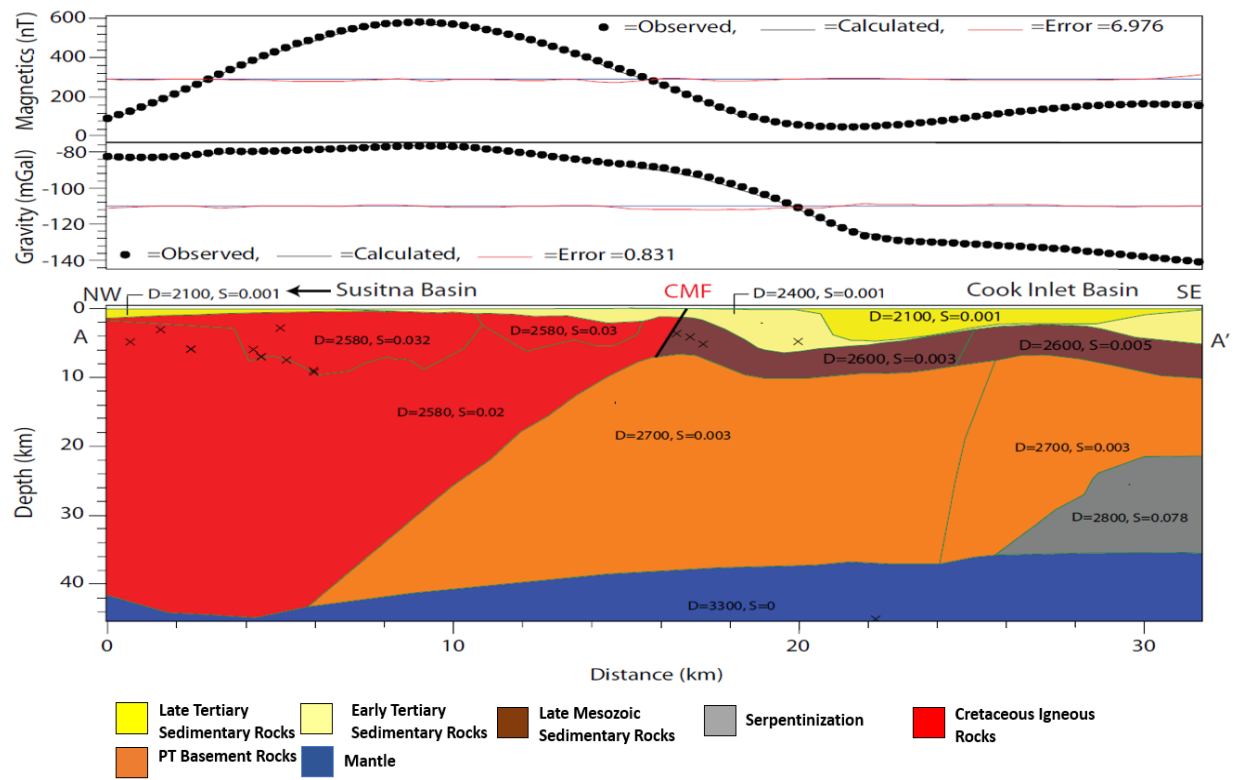


Figure 11: 2D profile A-A' showing the western CMF forming at the contact of Cretaceous igneous rock and Late Mesozoic sedimentary rocks. See table 1 for descriptions of rock units. See figure 10 for location of profiles

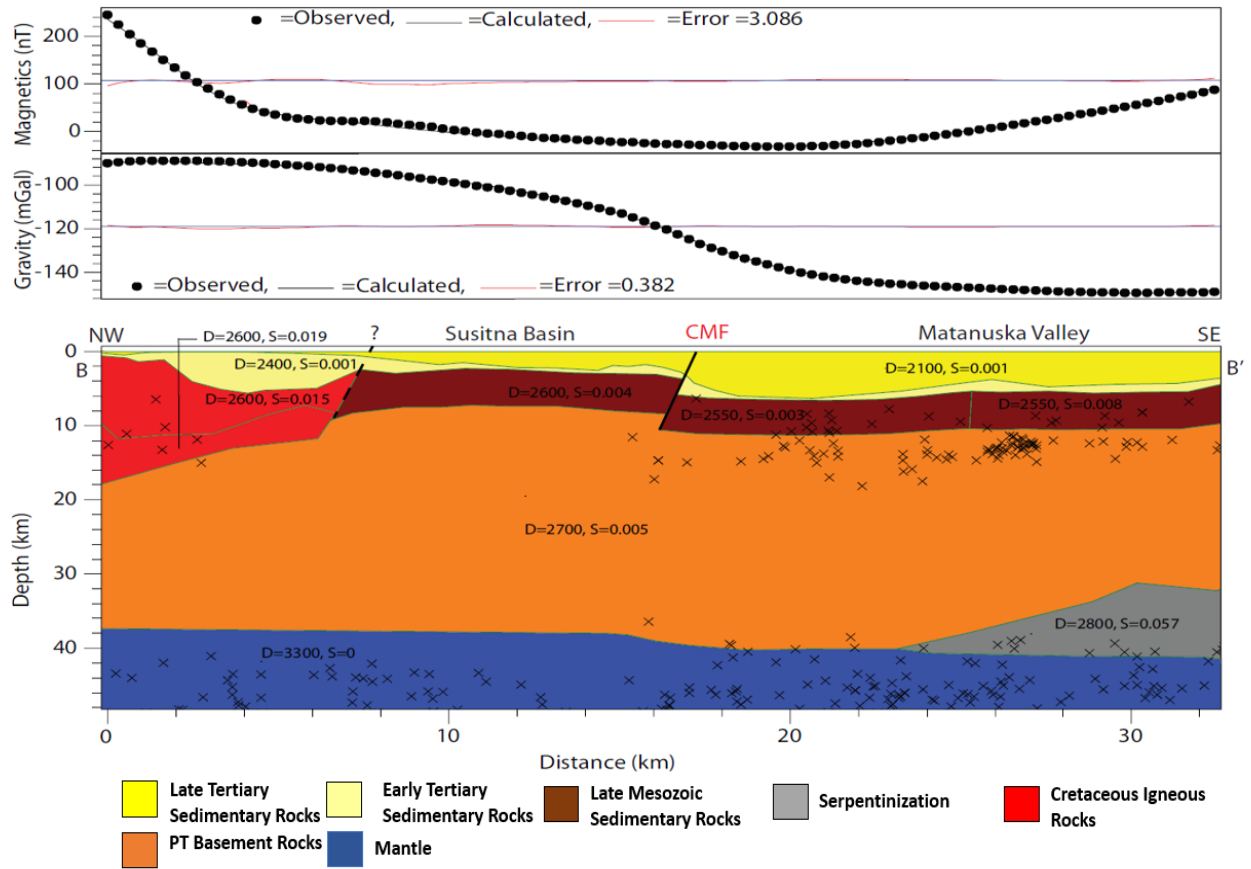


Figure 12: 2D profile B-B' showing the west CMF cutting through the late Mesozoic sedimentary rock.

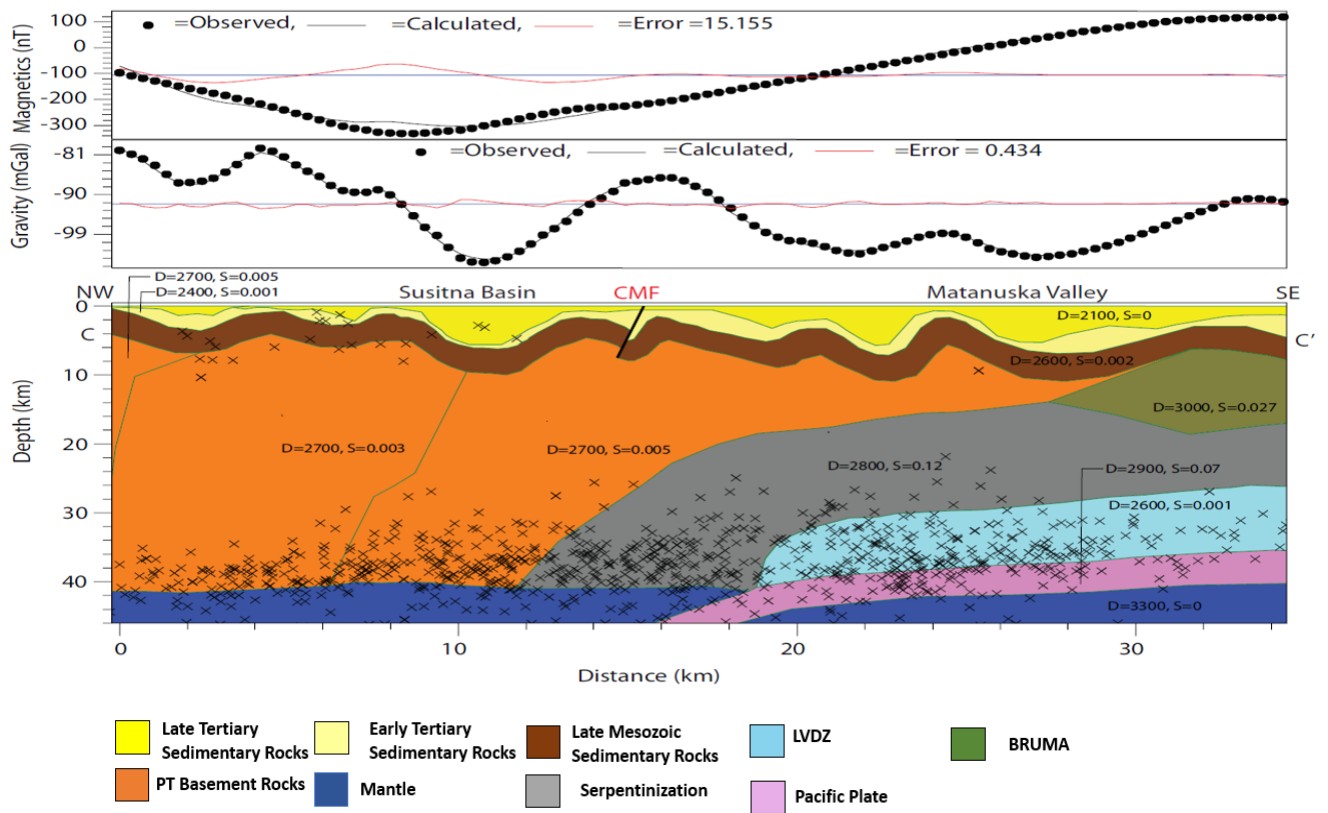


Figure 13: 2D profile C-C' showing eastern CMF cutting through the late Mesozoic sedimentary rock. The high magnetic signature requires the presence of serpentinized rocks and the subducting Pacific plate. The gravity anomaly undulations are associated with folding of the late Mesozoic rocks. BRUMA=Border Range Ultramafic and Mafic Assemblages. LVDZ=Low Velocity and Density Zone. LVDZ is associated with the subducting Yakutat microplate.



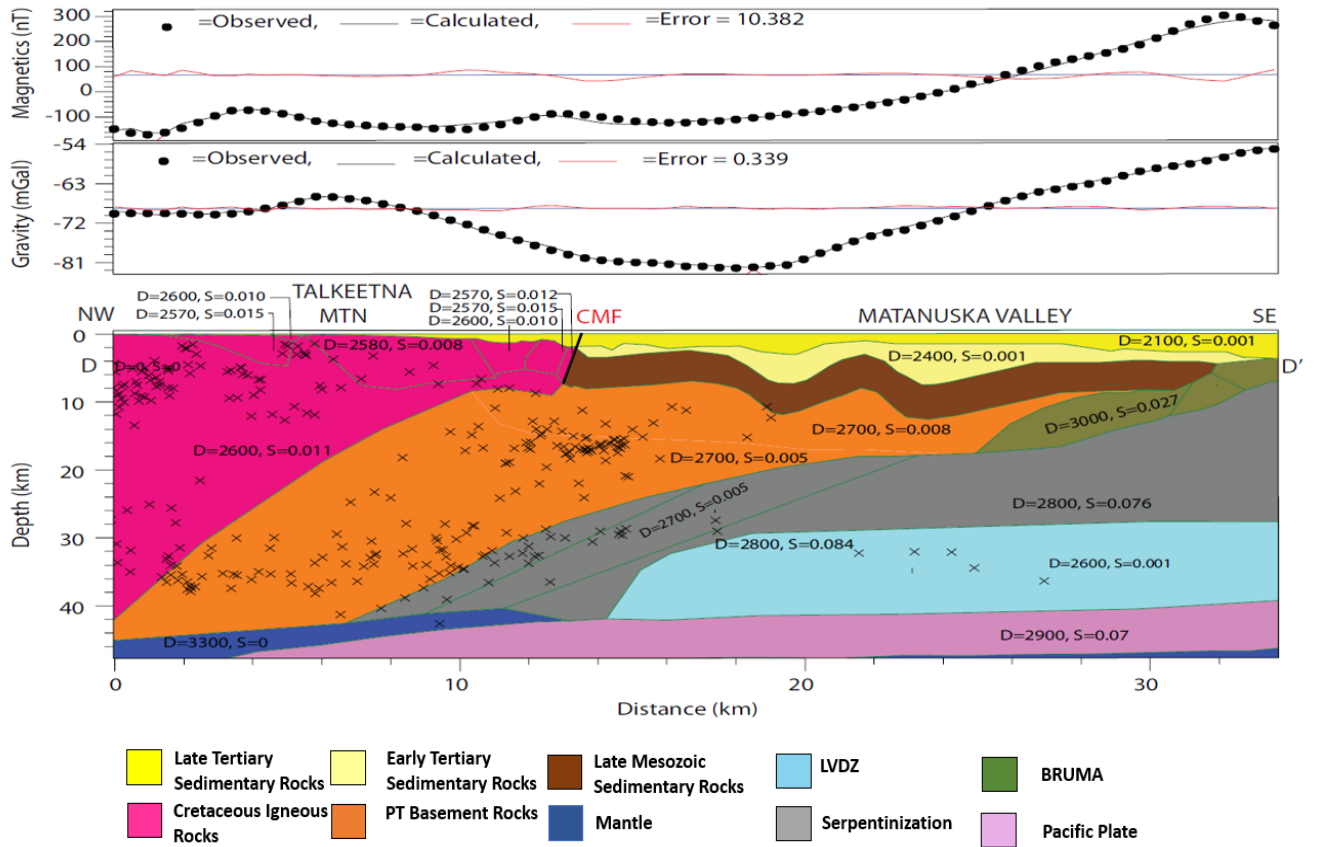


Figure 14: Profile D-D' showing eastern CMF formed at the contact of the Cretaceous igneous rock and the late Mesozoic sedimentary rock. Late Mesozoic rocks are folded. The high magnetic and gravity signatures at the southeast section of the profile are best modelled with extensive serpentinized rocks and the BRUMA.

## 1.7 DISCUSSION

The 2D profiles developed gives geometric and geological description of the subsurface geology within the vicinity of CMF. The profiles only provide a cross section of the CMF and geology lying parallel to the northwest in the direction of motion of the Pacific plate and Yakutat microplate. All the 2D profiles show presence of deposits of Early Tertiary sediments that are unconformably overlain by late Tertiary sediments within the Susitna basin, consistent with recent investigation conducted using well logs, seismic-reflection, gravity and aeromagnetic data (Shah et al., 2014, Stanley et al., 2014; Lewis et al., 2015; Saltus et al. (2016). The thicknesses of the Tertiary sedimentary unit are within ~ 4-5 km within the Susitna Basin (Saltus et al., 2016). The serpentinized block are thicker at ECMF and provides a good match for the varying magnetic and gravity anomalies. The modelled BRUMA along WCMF shows no root within the profiles (C-C' and D-D') indicating it either has a root towards the Border Range fault located at the southeast to the profile or it was carried to the surface before the collision the Peninsula Terrane.

Earthquake are plotted at depth across these profiles to analyze the deformation across the CMF region. The CMF is modelled along the contact between granitic intrusion and Mesozoic sedimentary rocks in A-A' and D-D'. The Cretaceous igneous rocks are characterized by increased seismicity indicating active motion or deformation within these rocks. This deformation may influence or play a role in the fault kinematics. Seismicity along CMF is mainly Models B-B' and C-C' are closest to the area consisting of mapped fault scarps and shows CMF cutting through the Mesozoic sedimentary rock.

Stress studies in southern Alaska Ruppert et al. (2008) reveals that the ECMF is dominated by a SW-NE maximum stress and the WCMF is dominated by vertical maximum stress. The dominant stress along the ECMF controls the right lateral movement along CMF. Surface evidence along

the fault has been identified along the Holocene scarp to supports right lateral motion. Additionally, Haeussler et al., (2000) identified lateral transpressional deformation in the Matanuska Valley and upper Cook Inlet area. The models show NW-SE deformation (Folds and fault) within the Mesozoic and Tertiary sedimentary rocks. This deformation can to attributed to the subduction of the Yakutat microplate resulting in structural complexities within the region (Plafker et al., 1978, Plafker, 1987 and Plafker et al., 1994). The folds are located in the Susitna basins and Matanuska valley with a combination of symmetric and asymmetrical axes similar to folds identified by Haeussler et. al. (2000). The CMF angle of the align well with the earthquake locations along profiles A-A' and B-B'. The presence of the earthquakes along the WCMF signifies its continuous motion. Profile B-B' is the zone of recorded Holocene movement, shows linear vertical seismicity pattern that aligns with the fault, I infer that there is a possibility of a deeper vertical extent of CMF. There is clear evidence of higher seismicity within the crust, a zone of zero coupling, towards the ECMF but there is no clear structural deformations that can be linked to this high rate of seismicity. This is high seismicity is likely produced by compressional stress produced by the collision of the Yakutat microplate.

With a high angle reverse fault that lies along Cretaceous igneous rocks and Mesozoic sedimentary with some sections cutting through the Mesozoic sedimentary rocks, there is likely high rate of coupling along this fault. This fault lies within a zone of low angle. These could inhibit fluid movement to the eastern edge of the Yakutat block.

## 1.8 CONCLUSIONS

Four detailed 2D forward models were created across the Castle Mountain Fault using newly collected gravity data with constraints from existing aeromagnetic data and previous geological and geophysical studies. The profiles provide a NW-SE cross section of the CMF as well as the geology surrounding the fault. The CMF is bounded by Cenozoic igneous rocks and Mesozoic rocks that can produce high rate of coupling along the fault. The models show thick Tertiary and Mesozoic sediments within the Susitna basin, Cook Inlet and Matanuska basin. The Mesozoic sedimentary rock show a high rate of deformation consisting of folds and faults along the ECMF than the WCMF. I infer that the oblique transpressional stress subjected across the fault played a major role in the varying deformations. Serpentinized rocks and BRUMA blocks provide a good fit for high magnetic and gravity anomaly. Our profile estimates a thickness of ~14 km for the LVDZ which represents the zone of the subducting Yakutat microplate. Thick Cretaceous igneous rocks were modelled along the WCMF and WCMF. The susceptibility variation of the Cretaceous suggest that they may have been formed by different melt or there is some influence produce due to magma mixing.

Plotted seismic events across the profiles provides a possible continuous Holocene motion mainly along the ECMF. There is a high rate seismicity within the crust within the margin of the subducting Yakutat microplate. The Cretaceous igneous rocks are also associated with high rate of seismicity. I infer that this seismicity plays a major role the fault kinematics. The models show the high angle CMF cutting through the Mesozoic sedimentary rocks and a possible deeper extension based on seismicity around the ECMF zone with emphasis in the region of exposed Holocene scarp. Deformed Mesozoic sedimentary rocks are modelled across all the regions of

CMF. The model shows high rate of seismicity within the crust possibly due to the collision of the Yakutat microplate.

## 1.9 REFERENCES

- Alaska Earthquake Information Center, 2014, AEIC earthquake database search: [http://www.aeic.alaska.edu/html\\_docs/db2catalog.html](http://www.aeic.alaska.edu/html_docs/db2catalog.html) (accessed January 2014).
- Blakey, R.J., 1995, Potential theory in gravity and magnetic applications: Cambridge, UK, Cambridge University Press, 136 p.
- Burger, R.H., Sheehan, A.F., and Jones, C.H., 2006, Introduction to applied geophysics: Exploring the shallow subsurface: New York, W.W. Norton, 554 p.
- Brocher, T.M., G.S. Fuis, M.A. Fisher, G. Plafker, M.J. Moses, J.J. Taber, and N.I. Christensen, 1994, Mapping the megathrust beneath the northern Gulf of Alaska using wide-angle seismic data, *J. Geophys. Res.* 99, 663-686.
- Cardenas, R., M. Ceberio, 2012, Efficient geophysical technique of vertical line elements as a natural consequence of general constraints techniques, *J. Uncert. Syst.* 6, 86-88.
- Doser, D.I., N.A. Ratchkovski, P.J. Haeussler, and R. Saltus, 2004, Changes in crustal seismic deformation rates associated with the 1964 Great Alaska earthquake: *Bull. Seismol. Soc. Amer.* 94, 320-325.
- Debari, S.M., and Coleman, R.G., Exhumation of the deep levels of an island arc, the Tonsina ultramafic assemblage, Tonsina, Alaska: *Journal of Geophysical Research*, v. 94, p.4373-4391, doi:10.1029/JB094iB04p04373.
- Detterman, R.L., Plafker, G., Tysdal, R.G., and Pavoni, N., 1974, Surface geology and Holocene breaks along the Susitna segment of the Castle Mountain fault, Alaska: U.S. Geological Survey Miscellaneous Field Studies Map MF-618, 1 plate, scale 1:24,000.
- Ehm, A., 1983, Oil and gas basins map of Alaska: Alaska Division of Geological and Geophysical Surveys Special Report 32, 1 sheet, scale 1:2,500,000

- Flores, C. and D. I. Doser, 2005, Shallow seismicity of the Anchorage, Alaska region: Bull. Seismol. Soc. Am., 95, 1865-1879.
- Gesch, D.B., Oimoen, M., Greenlee, S., Nelson, C., Steuck, M., and Tyler, D., 2002 The National Elevation Dataset: Photogrammetric Engineering and Remote Sensing, v. 68, p. 5-11.
- Gesch, D.B., 2007, The National Elevation Dataset, *in* Maune, D., ed., Digital elevation model technologies and applications: The DEM user's manual (second edition): Bethesda, Maryland, American Society for Photogrammetry and Remote Sensing, p.99-118.33
- Haeussler, P. J., 1994, Possible active fault traces on or near the Castle Mountain fault between Houston and the Hatcher Pass Road: in Till, A., and T. Moore, eds., Geologic studies in Alaska by the U.S. Geol. Surv. 1993, U.S. Geol. Surv. Bull. 2107, 49-58.
- Haeussler, P., and R. Saltus, 2011, Location and extent of Tertiary structures in Cook Inlet Basin, Alaska, and mantle dynamics that focus deformation and subsidence, Prof. Paper 1776-D.
- Haeussler, P., R. L. Bruhn, and T.L. Pratt, 2000, Potential seismic hazards and tectonics of Upper Cook Inlet Basin, Alaska, based on Pliocene and younger deformation: Geol. Soc. Am. Bull. 112, 1414-1429.
- Haeussler, P.J., T.C. Best and C.F. Waythomas, 2002, Paleoseismology at high latitudes: Seismic disturbance of upper Quaternary deposits along the Castle Mountain fault near Houston, Alaska: Geol. Soc. Am. Bull. 114, 1296-1310.
- Lahr, J.C., R.A. Page, C.D. Stephens and K.A. Fogleman, 1986, Sutton, Alaska, earthquake of 1984: evidence for activity on the Talkeetna segment of the Castle Mountain fault system: Bull. Seism. Soc. Am. 76, 967-983.

Mankhemthong, N., Doser, D.I., and Baker, M.R., 2012, Practical estimation of near surface bulk density variations across the Border Ranges fault system, central Kenai Peninsula, Alaska, *Journal of Environmental & Engineering Geophysics*, v. 17, p. 151-158, doi:10.2113/JEEG17.3.151.

Mankhemthong, N., D.I. Doser, M.R. Baker and R. Cardenas, Constraints on the structure of the Border Ranges fault system, south-central Alaska, from the integrated 3-D inversion of gravity data, *Geol. Soc. Amer. Rocky Mtn. Section Meeting*, Albuquerque, NM, abstract 34-10, May 2012b.

Mankhemthong, N., Doser, D.I., and Pavlis, T.L., 2013, Interpretations of gravity and magnetic data and development of 2.5D cross sectional models for the Border Ranges fault system, south-central Alaska, *Geosphere*, v. 9, p. 242-259, doi:10.1130/GES00833.1.

Merritt, R.D., 1986 Paleoenvironmental and tectonic controls in major coal basins of Alaska, *in* Lyons, P.C., and Rice, C.L., eds., *Paleoenvironmental and Tectonic Controls in Coal-Forming Basins in the United States: Geological Society of America Special Paper 210*, p. 173-200.

Meyer, J.F. and Boggess, P.L., 2003, Principal facts for gravity data collected in the Susitna area, southcentral Alaska: Alaska Division of Geological & Geophysical Surveys Preliminary Interpretive Report 2003-3, 13 p.

Nokleberg, W.J., Plafker, G. & Wilson, F.H., 1994, Geology of south-central Alaska, *in* Plafker, G., and Berg, H.C., eds., *The Geology of Alaska*; Boulder, Colorado, Geological Society of America, *Geology of North America*, v. G-1, p. 311-366.34

Pavlis, T.L., and Roeske, S.M., 2007, The Border Ranges fault system, southern Alaska, *in* Ridgway, K.D., et al., eds., *Tectonic growth of a collisional continental margin: Crustal evolution of southern Alaska: Geological Society of America Special Paper 431*, p. 95-128, doi:10.1130/2007.2431(05).



Plafker, G., Nokleberg, W., and Lull, J., 1989 Bedrock geology and tectonic evolution of the Wrangellia Peninsular, and Chugach terranes along the Trans-Alaska Crustal Transect in the Chugach Mountains and southern Copper River Basin, Alaska: *Journal of Geophysical Research*, v. 94, p. 4255-4295, doi:10.1029/JB094iB04p04255.

Ratchkovski, N.A., R.A. Hansen, J.C. Stachnik, T. Cox, O. Fox, L. Rao, E. Clark, M. Lafevers, S. Estes, J.B. MacCormack, and T. Williams, 2003, Aftershock sequence of the Mw 7.9 Denali fault, Alaska, earthquake of 3 November 2002 from regional seismic network data: *Seismol. Res. Lett.*, 74, 743-752.

Saltus, R.W., G.G. Connard and P.L. Hill, 1999, Alaska Aeromagnetic Compilation-Digital Grids and Survey Data, U.S. Geol. Surv. Open File Rept. 99-502.

Saltus, R.W., P.J. Haeussler, R.E. Bracken, J.P. Doucette, and R.C. Jachens, 2001, Anchorage urban region aeromagnetics (AURA) project: preliminary geophysical results, U.S. Geol. Surv. Open-File Rept. OF 01-0085, 21 pp.

Saltus, R.W., and Simmons, G.C., 1997, Composite and merged aeromagnetic data for Alaska: A website for distribution of gridded data and plot files: U.S. Geol. Surv. Open-file Rept. 97-520, <http://geology.cr.usgs.gov/pub/open-file-reports/ofr-97-0520/>.

Saltus, R.W., Hudson, T.L., and Wilson, F.H., 2007, The geophysical character of southern Alaska-Implications for crustal evolution *in* Ridgway, K.D., et al., eds., *Tectonic growth of a collisional continental margin: Crustal evolution of Southern Alaska*: Geological Society of America Special Paper 431, p. 1-20, doi:10.113/2007.2431(01).

Sanger, E.A., and Glen, J.M.G., 2003, Density and magnetic susceptibility values for rocks in the Talkeetna Mountains and adjacent region, south-central Alaska: U.S. Geological Survey Open-File Report 03-268, 42 p.

- Shellenbaum, D.P., Gregersen, L.J., and Delaney, P.R., 2010, Top Mesozoic unconformity depth map of the Cook Inlet basin, Alaska: Alaska Division of Geological and Geophysical Surveys Report of Investigation 2010-2, 1 sheet, scale 1:500,000.
- Swenson, R.F., 1997, Introduction to Tertiary tectonics and sedimentation in the Cook Inlet Basin, *in* Karl, S. M., Vaughn, N.R., and Ryherd, T.J., eds., 1997 Guide to the geology of the Kenai Peninsula, Alaska: Geological Society, p. 18-27.35
- Trop, J.M., and Ridgway, K.D., 1999, Sedimentology and provenance of the Paleocene-Eocene Arkose Ridge Formation, Cook Inlet-Matanuska Valley forearc basin, southern Alaska: Short notes on Alaskan geology, Alaska Division of Geological and Geophysical Surveys: Professional Report, v. 119, p. 129–144
- Trop, J.M., Szuch, D.A., Rioux, M., and Blodgett, R.B., 2005, Sedimentology and provenance of the Upper Jurassic Naknek Formation, Talkeetna Mountains, Alaska: Bearings on the accretionary tectonic history of the Wrangellia composite terrane: Geological Society of America Bulletin, v. 117, p. 570-588, doi:10.113/B25575.1.
- Tysdal, R.G., Plafker, G., 1978, Age and continuity of the Valdez Group, southern Alaska, *in* Sohl, N.F., and Wright, W.B., eds., Changes in stratigraphic nomenclature by the U.S. Geological Survey, 1977: U.S. Geological Survey Bulletin 1457-A, p. A120-A124.
- Wesson, R.L., A.D. Frankel, C.S. Mueller, and S.C. Harmsen, 1999, Probabilistic seismic hazard maps of Alaska: U.S. Geol. Surv. Open File Rept. 99-36, 20 pp.
- Willis, J.B., P.J. Haeussler, R.L. Bruhn, and G.C. Willis, 2007, Holocene slip rate for the western segment of the Castle Mountain fault: Alaska, Bull. Seism. Soc. Am. 97, 1019-1024.

Wilson, F.H., Hults, C.P., Schmoll, H.R., Haeussler, P.J., Schmidt, H.M., Yehle, L.A., and Labay, K.A., 2009, Preliminary geologic map of the Cook Inlet region, Alaska: U.S. Geological Survey Open-file Report 2009-1108, <http://pubs.usgs.gov/of/2009/1108/>.

## **SECTION 2**

### **GEOPHYSICAL INVESTIGATION OF STRUCTURAL AND TECTONIC VERTICAL MOTION WITHIN COOK INLET BASIN AND KENAI MOUNTAIN, ALASKA**

#### **2.1 ABSTRACT**

In southcentral Alaska, Cook Inlet basin (CIB) is undergoing subsidence while Kenai Mountain is uplifting. Shortening and collision of the buoyant Yakutat microplate have produced focused deformation within CIB. The Kenai Mountain uplift has been attributed to the subduction of the Yakutat microplate and/or isostatic rebound. The subsidence has been suggested to be related to the formation of an unusually hydrated and serpentinized mantle wedge with lateral variations in heat flow due to a shallow-eastward subducting slab. Serpentinization would produce a subsurface body of increased magnetic susceptibility and reduced density and velocity compared to the surrounding ultramafic rocks. The focus of this research is to locate such a body by using 3D inversion of a long wavelength magnetic anomaly and a low amplitude gravity anomaly within the CIB to determine whether both anomalies are associated with the serpentinization.

The magnetic inversion shows that the source of the long wavelength magnetic anomaly varies across the basin. The maximum depth to the bottom of the magnetic source is ~37 km at the southwestern section of the basin, the shallowest depth of ~15km trends from the middle of the basin toward the northern boundary. The inversion of the gravity anomaly shows the source is thin and the depth to the top of the low amplitude gravity source is ~ 15 km throughout the CIB. However, the location of the gravity source appears to be in the same area where the magnetic source is shallow with the depth to the bottom of the magnetic source at ~15 km. This result indicates the magnetic anomaly source overlies the gravity anomaly source and thus the two

anomalies cannot be from the same rock unit. This result does not support the presence of a large region of serpentinization beneath the CIB. The long axis of the thin crust, mapped by the low gravity anomaly, lies along a possible axial plane of a major syncline causing a shortening and subsidence within the CIB.

## 2.2 INTRODUCTION

Cook Inlet Basin (CIB) and the Kenai Peninsula of Alaska are located on the North American plate directly above the subducting Pacific plate (Figure 1). To the east, the relatively buoyant Yakutat microplate is being subducted with the Pacific plate and this complicates regional deformation. Earthquake and controlled source seismic data (e.g. Haeussler et al., 2000; Doser et al., 2004, Bauer et al., 2014) show the subducting plate descending at an angle of less than 2 degrees beneath the Alaskan margin of North America. This results in the transmission of stresses into the overlying North American plate producing some of the most intense deformation and largest earthquakes observed in the world (Doser et al., 2004). The deformations caused by the subduction of the Yakutat microplate have been linked to the uplift of Kenai Mountain (Pavlis and Bruhn, 1983; Doser 2004; Finzel et al., 2011).

As the Pacific plate moves beneath the North American plate, water in the rocks and sediments of the Pacific plate is expelled due to increasing pressure and heat producing serpentinization of lower crustal rocks of the North American plate (Hydman and Peacock 2003). Because the serpentinized rocks (Haeussler et al., 2011; Mankhemthong, 2012; Shinagel, 2015) have a lower density than the surrounding rocks, they tend to rise buoyantly. If serpentinization is causing uplift along coastal Alaska, then the currently rising Kenai Peninsula is one potential place where that may be occurring. However, there is no evidence of serpentinization beneath the Kenai Peninsula. Haeussler and Saltus (2008) have attributed serpentinization to the subsidence of the CIB. They suggest the presence of fluid flow within the slab margin as it subducts underneath the North American plate and that fluid flows into the adjacent mantle wedge which decreases viscosity and enhances corner flow to drive subsidence.

The focus of this research was to determine whether serpentinization was occurring beneath the CIB (Haeussler et al., 2011; Mankhemthong, 2012; Shinagel, 2015). Results from gravity and magnetic inversions are compared to earthquake locations (Silwal et al., 2018) and time series GPS data (figure 28; from 2006 to 2016) downloaded from the University NAVSTAR consortium (UNAVCO) website (<ftp://data-out.unavco.org/pub/products/>) to determine how current seismic and non-seismic deformations are related to the crustal structure and the presence of serpentinized rocks. The results of this study suggest no significant serpentinization is occurring beneath the CIB and the subsidence of the basin may be due to folding generated by the shallow subduction of the Yakutat microplate.

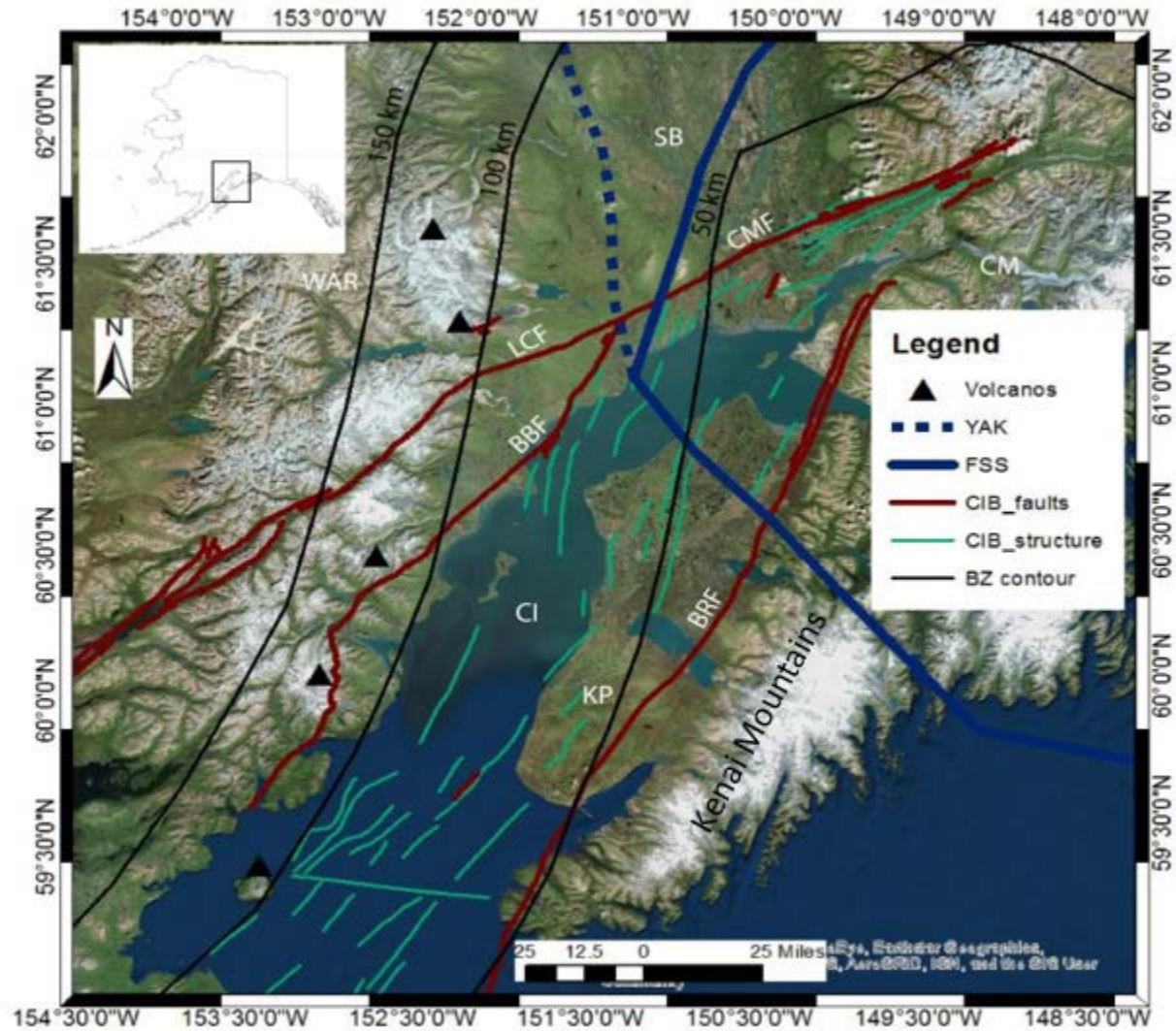


Figure 1: Map of the Cook Inlet Basin, Alaska, showing recent faults and folds related to deformation in the region. CI=Cook Inlet, KP=Kenai Peninsula, WAR= Western Alaska Range, BRF=Border Ranges fault, FSS=region of flat slab subduction, SB=Susitna Basin, CMF=Castle Mountain fault, CM=Chugach Mountains, YAK= Interpreted subsurface extent of the Yakutat microplate. Yakutat outline and Benioff zone contour modified from Eberhart-Phillips et al., (2006), Faults traced from Haeussler et al., (2011)



## **2.1 BACKGROUND**

### **2.1.1 TECTONICS OF COOK INLET BASIN**

Southcentral Alaska (Figure 1) is dominated by a convergent plate boundary with an oceanic arc in the west and a continental arc in the east. The CIB is a forearc basin located directly above the transition from normal to flat-slab subduction. It is bounded by the Chugach and Kenai Mountains in the southeast and by the Alaska Range and Aleutian volcanic arc in the northwest. The basin sits about 50-60 km (Page et al., 1991) above the subducting Pacific plate and Yakutat microplate (Pavlis et al., 2004). Folds in the CIB are described (Haeussler et al., 2000) as complex, discontinuous structures with variable shape and vergence that are speculated to have been formed by right transpressional deformation along oblique-slip faults.

Tectonic events within the CIB started in the Paleocene-Eocene with subduction of an oceanic spreading center (Bruhn et. al., 2006). This was followed by right-lateral strike-slip faulting along the northeastern section of the CIB which ended in the Oligocene (Bruhn et al., 2006). In the late Neogene through Holocene, the CIB underwent several episodes of faulting and folding (Bruhn et. al., 2006) with subsequent erosion of horst blocks leaving grabens that were filled with syn-faulted fluvial deposits (Haeussler et al., 2008; Kirschner et al., 1973; Calderwood et al., 1972). Kirschner and Lyon (1973) indicate a relationship between the regional strike-slip faulting and folding by observing that the orientation of the fold hinge lines align with the strike of the right-lateral Castle Mountain fault at the northeastern end of the basin. Bruhn and Haeussler (2006) suggested the basin is subjected to a compressional stress between the Bruin Bay and Border Ranges faults due to right-lateral motion along the Castle Mountain fault causing a right-transpressional deformation of the basin (Haeussler and Saltus, 2011).

### **2.1.2 GEOLOGY OF THE COOK INLET BASIN**

The CIB is filled with Mesozoic to Quaternary sediment and sedimentary rocks forming the main forearc basin stratigraphy that represents the sequence cover of the Peninsular Terrane (Plafker et al., 1994; Trop et al., 2005). The CIB is a 200 Ma forearc basin with Late Paleocene to Quaternary non-marine strata up to 8 km thick (LePain et al., 2013).

The Tertiary rocks are predominantly alluvial with some tidal inclusions (Calderwood and Fackler, 1972; Flores and Stricker, 1993; Flores and others, 1994, 1997, 1999). The Quaternary deposits consist of glacial and alluvial deposits which lie unconformably on Late Eocene to Upper Pliocene sedimentary rocks classified as the Kenai Group (fig. 2). The average thickness of Quaternary deposits is about 180m (Plafker et al., 1989) which increases to about 1200 m within the basin (Swenson, 1997). The Late Mesozoic sequence consists of shallow marine sedimentary rocks of Early Jurassic and non-marine Cretaceous strata with an approximate thickness of 8500 m, extending eastward from the Cook Inlet basin beyond the trailing edge of the Kenai Peninsula (Plafker et al., 1989, Trop and Ridgeway, 1999). Late Triassic to Early Jurassic Talkeetna Formation is present underneath the shallow marine sedimentary succession (Trop et al., 2005). This formation consists of approximately 3000 m of clastic, volcanic, and volcanoclastic rocks with a volcanic cover whose age agrees with the Early Jurassic intrusive assemblages of the Peninsular Terrane basement (Trop et al., 2005; Saltus et al., 2007).

The majority of the rocks within the Chugach and the Kenai Mountains belong to the Mesozoic and early Tertiary accretionary complex deposited in the Pacific Ocean basin and accreted to North America via subduction accretion (Plafker and others, 1994). This accretionary complex is referred to regionally as the Chugach terrane and was carried with the Wrangellia superterrane

prior to, during, and after its late Mesozoic accretion to the northern Cordillera (Plafker et. al., 1994a; Bruhn et. al., 2006; Amato et al., 2013).

### **2.1.3 PREVIOUS RESEARCH**

Haeussler et al., (2000) speculated that dextral transpression of the CIB was driven by coupling between the North American and Pacific plates along the Alaska-Aleutian subduction zone, and by lateral escape of the forearc to the southwest due to collision and indentation of the Yakutat terrane 300 km to the east of the basin. Global Positioning System data (e.g. Zweck et al., 2002) and a stress orientation study from earthquake seismicity (e.g. Flores and Doser, 2005) show that a change in coupling across the Alaska-Aleutian megathrust occurs near the Border Ranges Fault which suggests a possible link between the Neogene Border Ranges Fault and the current subduction processes (e.g. Fuller et al., 2006). This observation supports an earlier hypothesis of Pavlis and Bruhn (1983) that suggests a relationship between the forearc ridge and the viscous flow at the base of the accretionary complex.

Bruhn and Haeussler (2006) suggested the migration of the Chugach and Kenai Mountains towards the Alaska Ranges has been driven by the collision and subduction of the Yakutat microplate. This deformation produces belts of anticlines. Bruhn and Haeussler (2006) developed a tectonic model that suggests collision of the microplate as the driving force of dextral shearing and shortening within the CIB.

Haeussler and Saltus (2011) compiled the location and extent of folds and faults in the CIB using previously published maps, well locations, and seismic-reflection data (Haeussler et al., 2000).

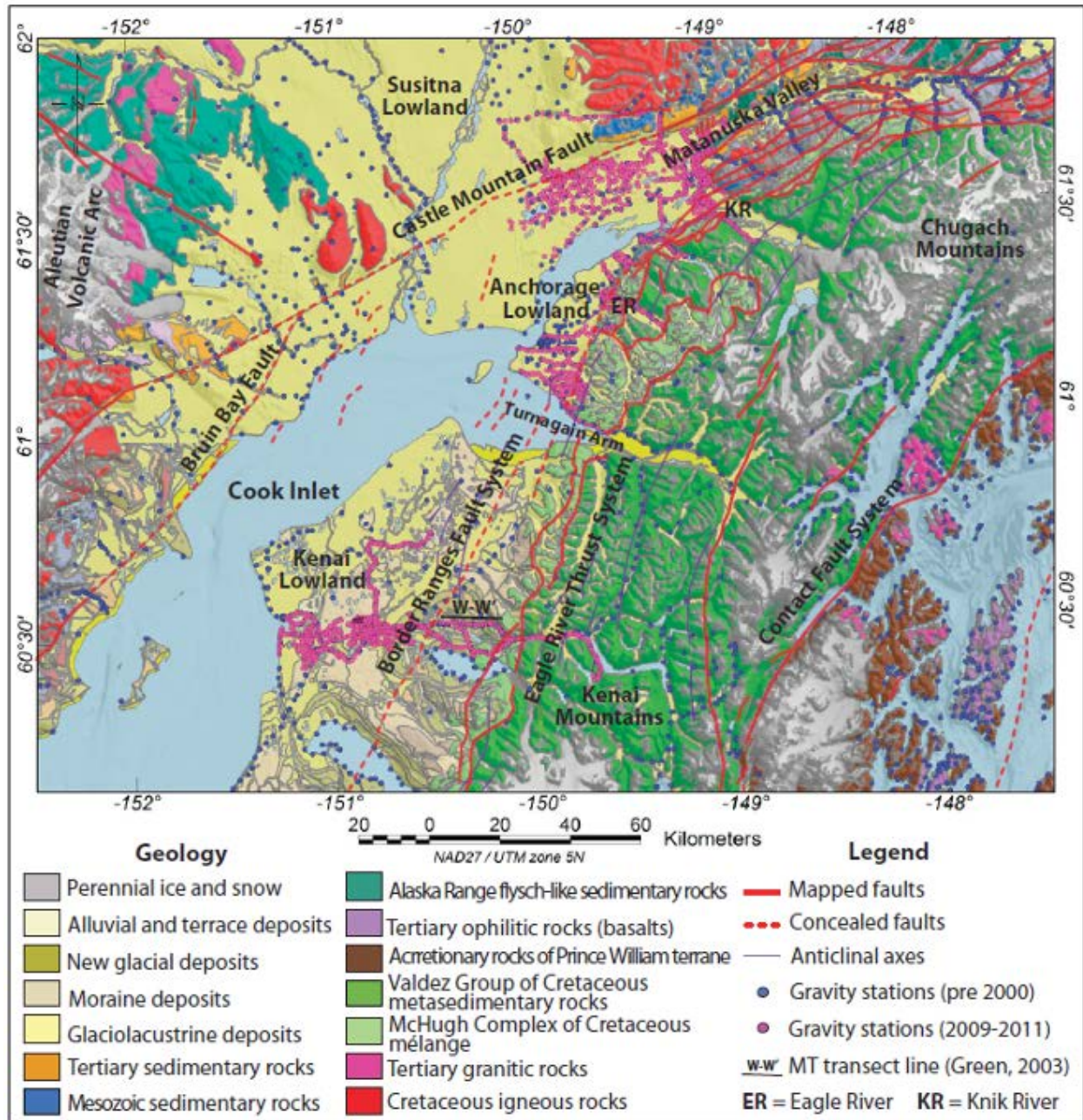


Figure 2: Geologic map of CIB, Kenai Peninsula and Chugach Mountains, locations of gravity points and mapped faults and folds. (modified from Mankhemthong 2012)

The research showed high amounts of deformation within upper CIB with counterclockwise rotation and northeast bending of the basin bounding faults creating a pattern of right-transpressional deformation (Haeussler and Saltus, 2011). The focus of deformation shows that the greatest shortening coincides with the deepest section of the Neogene basin in the Upper CIB. Magnetic, gravity, electrical and seismic signatures suggest fluids from the mantle wedge may produce serpentinization of ultramafic rocks which are expressed as a long-wavelength magnetic anomaly. From the results of the research, Haeussler and Saltus (2011) suggested that the buoyant Yakutat slab drives the fluid flow to concentrate at the margins of the slab. In this model, the adjacent mantle wedge is fluxed by these leftover fluids that not only serpentinize the uppermost mantle but decrease wedge viscosity and enhance greater corner flow, which drives subsidence within the forearc region. Haeussler and Saltus (2011) also inferred that gravity data within the upper CIB are consistent with the dynamic component of basin subsidence. This observation supports the sharp topographic change along the Cook Inlet-Susitna lowlands to the Kenai Mountains which has been related to motion along the BRFS and inferred to have generated the topographic transition within a region of active glacial and fluvial erosion (Pavlis and Bruhn, 1983; Pavlis and Roeske, 2007).

Doser and Veilleux (2009) conducted a comprehensive study by relocating ~34,000 earthquakes extending from Prince William Sound to Cook Inlet. The result was integrated with magnetic, gravity, tomographic, GPS-geodesy, and geologic information to image the geometry of the regional subduction. The integrated data show that the contrast in upper plate rheology influences changes in density, magnetic susceptibility, and velocity that serve to concentrate seismicity. The density and velocity contrasts corresponding to varying lower plate rheology also influences the

location of deeper (>30 km) seismicity and the occurrence of a double seismic zone within the subducting Pacific plate (Doser and Veilleux, 2009).

Mankthemthong et al., (2012) used gravity, aeromagnetic and other geophysical data to examine the geometry of the Border Ranges Fault System, the Border Range ultramafic and mafic assemblages and other forearc-arc boundary structures in south-central Alaska. Their models showed a thick sequence of Late Mesozoic sedimentary rocks and defined the extent of a serpentinized body overlain by a Peninsular Terrane basement (Mankthemthong et al., 2012). None of the previous research within CIB has directly focused on comparing the depth of gravity and magnetic anomalies to help explain the tectonic controls for the low density and high magnetic anomalies previously suggested to be evidence for serpentinization (Haeussler et al., 2011). The 3D inversion of magnetic and gravity data integrated with spectral analysis of magnetic data and temperature models could help determine whether serpentinization is the cause of the observed anomalies or if there are other possible explanations for these observations.

## **2.2 INVESTIGATING THE PRESENCE OF SERPENTINIZATION BENEATH COOK INLET BASIN**

Serpentinization is inferred to be a common feature of the subsurface below a forearc because a subducting oceanic plate releases H<sub>2</sub>O-rich fluid which could migrate into and hydrate the overlying forearc mantle (Hydman and Peacock 2003). The physical and mechanical properties of a forearc mantle are affected by the presence of serpentine and other hydrous minerals, which are strongly influenced by the thermal structure of the forearc. Serpentinization, in turn, changes the physical and mechanical properties of the region and result in decreased seismic velocities, increased Poisson's ratios, generation of seismic reflectivity, increased magnetization, reduced density, increased electrical conductivity, and reduced mechanical strength compared to the surrounding ultramafic and mafic rocks (Hydman and Peacock 2003).

The change in properties of a serpentinized region can produce mantle wedge flow which enhances melt generation, arc volcanism, and heating at the top of the subducting slab to generate dehydration (Wada et al., 2011). Wedge flow in the forearc region is primarily controlled by viscous coupling between the subducting slab and the overriding plate (Wada et al., 2011). Weak hydrous minerals produced by serpentinization at the interface of the shallow slab and mantle cause decoupling (Wada et al., 2008, 2011).

Several heat flow and temperature studies have been conducted in Alaska to understand tectonic processes (eg. Peacock, 1996; Abers et. al., 2006) and to assess geothermal prospects within the region (e.g. Waring 1917, Lachenbruch and Marshall 1969, Lachenbruch 1970, Miller et. al., 1975, Lachenbruch et. al, 1982, Motyka et al., 1983, Denig-Chakroff et al., 1985, Sass et al 1985, Miller 1994, Blackwell and Richards 2004b, Kolker 2007, Erkan et al 2008, Kolker 2008, Kolker et al., 2012, Batir et al 2013, Batir et al., 2016). Peterson (2013) calculated average thermal gradient

within the CIB using bottom hole temperature and drill stem test data, within a true vertical depth between ~2.4 to 3.6 km, the geothermal gradient ranged from 12.87 to 15.94°C/km. In this research he identified a high thermal gradient adjacent to the Bruin Bay fault due to its proximity to the volcanic arc and an increasing gradient from the north to the south of CIB. Temperature profiles within CIB region and its vicinities were generated to a depth of 10 km using parameters from Batir et al. (2016) and a method adopted by Blackwell et al. (2007).

Seismic tomography (e.g. Kissling and Lahr, 1991; Eberhart-Phillips et al., 2006) reveals a pronounced low P-wave velocity anomaly beneath the forearc mantle of southern Alaska. Ambient noise tomography conducted by Fliedner and Klemperer (1999) proposed the presence of pyroxene-rich cumulates to be influencing the low velocity but suggested serpentinization as the possible cause of low velocity in the forearc mantle that generated the observed mantle reflectivity. Increasing the rate of serpentinization produces a substantial decrease in density of unaltered ultramafic rocks from ~ 3200kgm<sup>-3</sup> to 2600 kgm<sup>-3</sup>.

The large density variation and velocity change, which is expected in a region with a high degree of serpentinization, are such that forearc mantle serpentinites are difficult to distinguish from greater crustal thickness in gravity modeling. The gravity modeling process for a subduction zone is further complicated by the influence of dynamic topography that affects the ability to detect the reduced density of the forearc mantle. Serpentinization reduces the density of the affected rock, which becomes lower than normal mantle rocks. This affects the isostatic balance leading to uplift. To eliminate the effect of dynamic topography on a Bouguer gravity anomaly, an isostatic gravity anomaly approach can be used.

Increasing serpentinization can result in a corresponding increase in magnetic susceptibility (i.e from about 10<sup>-3</sup> SI to about 3x10<sup>-2</sup> SI) to as much as 30 times the initial value because magnetite



is produced by the serpentinization of olivine (Toft et al., 1990). Magnetized rocks have different Curie temperatures depending on the extent of magnetization and the type of magnetic minerals found within them. The process of serpentinization of ultramafic rocks generates the mineral magnetite (Hydman and Peacock, 2003) whose commonly used Curie temperature is  $\sim 580^{\circ}\text{C}$  for Curie point depth analyses (Haggerty, 1978).

## 2.3 METHODOLOGY

To test for the presence of serpentinization I used three geophysical methods; magnetics, gravity and temperature. The first approach to identify serpentinization was to estimate the depth to the top and bottom of the sources of magnetic anomalies using three-dimensional (3D) inversion of aeromagnetic data (e.g. Hussein et al., 2012; Mickus and Hussein, 2015). The second approach was to constrain these depths using spectral analysis conducted across long wavelength anomalies to calculate the depth to the bottom of the magnetic sources within CIB (e.g. Hussein et. al., 2012; Mickus and Hussein, 2015). The estimated depths from spectral analysis are compared with those from the 3D inversion. Another approach to constraining the depth to bottom of the magnetic sources is to generate temperature profiles to estimate the depth to the Curie temperature (580°C) across the CIB. Three-dimensional inversion of gravity data was also conducted to identify the location of the long wavelength anomalies and compare these to the position of the magnetic sources to see if they coincide or are found at different locations. The aeromagnetic map (figure 3) shows a long wavelength anomaly trending SW to NE within the basin. Similarly, the gravity anomaly map (Figure 4) also shows a long wavelength low gravity anomaly trending north to south. These anomalies have been interpreted to indicate the presence of a serpentinized body underneath the Cook Inlet basin (e.g. Haeussler and Saltus 2011 and Mankhemthong et al., 2013). To perform the 3D inversion for magnetic and gravity data, the study area was divided into twenty-one blocks of 1° X 1° dimension (figure 3). To avoid errors introduced by edge effects, I assigned an additional 0.25° to the blocks' dimensions. Therefore, input data dimension is 1.25°X1.25° for the 3D inversion. Twenty-one blocks labeled from 1 to 21 were generated. For 3D inversion of both magnetic and gravity, I used Mag3D and Grav3D software developed by the University of

British Columbia Geophysical Inversion Facility. These software packages are based on the work of Li and Oldenberg (1997; 1978).

### **2.3.1 MAGNETIC DATA**

The magnetic anomaly map (figure 3) is composed of four separate surveys conducted from 1957 to 1977 (Saltus and Simmons, 1997). Flight directions vary from N-S to E-W with altitudes from 120 to 760 m. Flight lines spacing ranges from 1600 m to 16000 m. Upward or downward continuation was applied to the data to minimize the boundary differences for flight spacing and altitudes of the original surveys to generate a consistent elevation of 305 m above the ground (Saltus and Simmons, 1997).

### **2.3.2 MAGNETIC INVERSION**

Magnetic prospecting is a widely used geophysical method for mapping geological structures and buried objects. Inversion of magnetic data estimates the depth and shape of the magnetic source based on the wavelength of the anomalies. Magnetic inversion is one of the techniques commonly used to estimate Curie point depth (CPD) by modeling the magnetic anomalies of isolated magnetic sources (Hussein et al., 2012; Mickus and Hussein, 2015). A variety of geometric shapes have been modeled using this technique (e.g. Bhattacharyya and Leu ,1975; Byerly and Stolt, 1977; Shuey et al., 1977; Hong ,1982; Mickus, 1989). The separation of regional from residual magnetic anomalies is necessary to compute the depth of the isolated magnetic source (Hussein et al.,2012; Mickus and Hussein, 2015). Bhattacharyya and Leu (1975), Byerly and Stolt (1977) and Shuey et al. (1977) assumed flat surfaces for the top and bottom of the geometric shape of the magnetic source which introduces errors in the depth estimates. Modelling of the positive anomalies using the above method requires identifying isolated anomalies from deep sources with

allowable thickness for CPD estimation (Hussein et al., 2012). One inherent problem with the inversion is that a broad shallow source may mimic a deep narrow source and be misplaced by the inversion. These problems are addressed in 3D inversion software based on the algorithm of Li and Oldenburg (1990) as applied by Hussein et al. (2012) and Mickus and Hussein (2015). Inversion parameters must be carefully varied to obtain a reliable solution as suggested in Li and Oldenburg (1990) to insure consistency of the models to the geology (Hussein et al., 2012; Mickus and Hussein, 2015).

### **2.3.3 MAGNETIC INVERSION RESULT AND INTERPRETATION**

The CIB cuts diagonally across total area with dimensions equivalent to twenty-one,  $1^\circ \times 1^\circ$ , blocks (figure 3). Magnetic data of blocks intersecting with CIB were selected, blocks 4, 6, 7, 10, 11 and 16) (Figure 3, 5a,5b, 5c) were selected and inverted to analyze the extent of the basin. The result of magnetic inversions were analyzed by constructing vertical slices along E-W (line 1) and S-N (line 2) directions of the 3D blocks (Figures 6a, 6b, 6c) to determine the depth of the sources. At the north of CIB, east and south slices of block 4 (Figures 6a; labeled 1 and 2 under block 4), show high amplitude magnetic anomaly south of the western CMF. The depth to the top of this anomaly is ~2.5 km and the bottom ~26 km. North to the western CMF is a high magnetic anomaly that extends from the southwestern rim of the Susitna basin and extend towards the Talkeetna mountains. The high magnetic anomaly extends into the Matanuska Valley, block 6 (figure 8b and figure 9: labelled 1 and 2 under block 6) and block 7 (figure 5b and figure 6b: labelled 1 and 2 under block 7) with the eastern CMF at the northern boundary and the BRF on its southern boundary. The depth to top and bottom of the high magnetic anomaly in block 6 is ~1 km to ~21 km respectively (figure 6a: labelled 1 and 2 under block 6). The depth to top and bottom of the high magnetic anomaly in block 7 is ~1 km and ~23 km respectively (Figure 11: labelled

1 and 2 under block 7). Thin slivers of high magnetic anomaly located south to BRF (block 6 and 7) beneath Chugach Mountains. The high magnetic anomaly continues at the central towards the south of the basin, block 11 (figure 5b and figure 6b: labelled 1 and 2 under block 11), 10 and 16 (figure 5c and figure 6a). The eastern extent of the high magnetic anomaly (block 11) is along the eastern boundary of the basin with a depth to top and bottom of ~1 km and 18.5 km respectively. This anomaly thickens westward and get deeper into the basin as shown in block 10 (figure 5c and figure 6a: labelled 1 and 2 under block 10). The depth to top and bottom of the anomaly is ~3 km and 36 km respectively. The deepest depth to top the anomaly in the center of the basin is ~10 km. The southern basin shows the high magnetic anomaly located at a depth of ~1 km with a bottom at ~37 km. Western slice of the block 16 shows a nice basin geometry with the deepest depth to top of the high magnetic anomaly ~10 km. The western and southern section of CIB shows thick magnetic anomalies ~21 km (block 10 and 16) at the southern basin. The magnetic anomalies thins out ( $\leq 15$  km) towards the eastern and northern section of CIB.

The inversion identifies a zone of large-amplitude magnetic high within CIB. This anomaly corresponds to the basin component of the Southern Alaska Deep Magnetic High (e.g. Saltus et al., 1999a, Saltus et al., 2001). High magnetic anomaly north to the western CMF (block 4) coincides with the highly magnetic igneous rock within the Beluga-Susitna Mountain and within deep basement of the Susitna basin (Saltus et al., 2016). A narrow basement with a trough on top of the high magnetic anomaly within Matanuska basin (block 6) is consistent with the Matanuska geosyncline named by Payne (1995) and differentiated in the Middle Jurassic as a deeply subsiding nonvolcanic depositional trough (Grantz 1964). The high magnetic anomaly coincides with the Knik Arm anomaly (Grantz et al., 1963; Fisher and Von Huene, 1984), a high magnetic anomaly associated with the Border Range ultramafic and mafic assemblages (BRUMA) (e.g.

Mankhemthong et al., 2012). The high magnetic anomaly north of the eastern CMF reflects magnetic igneous and metamorphic rocks forming the Talkeetna Mountains. Thin slivers of high magnetic anomaly consistent with anomalies associated with accretionary complex of the Chugach terrane (Saltus et al., 2007). Thick (~21km) magnetic anomalies at the southern section of CIB, corresponds to responses from Jurassic and younger arc-related rocks that forms part of the Wrangellia composite terrane of Plafker and Berg, (1994). The thickness of the anomaly is comparable to the highly magnetized zone of crustal scale with thickness of over 20 km in CIB modelled by Saltus et al.(1999b).

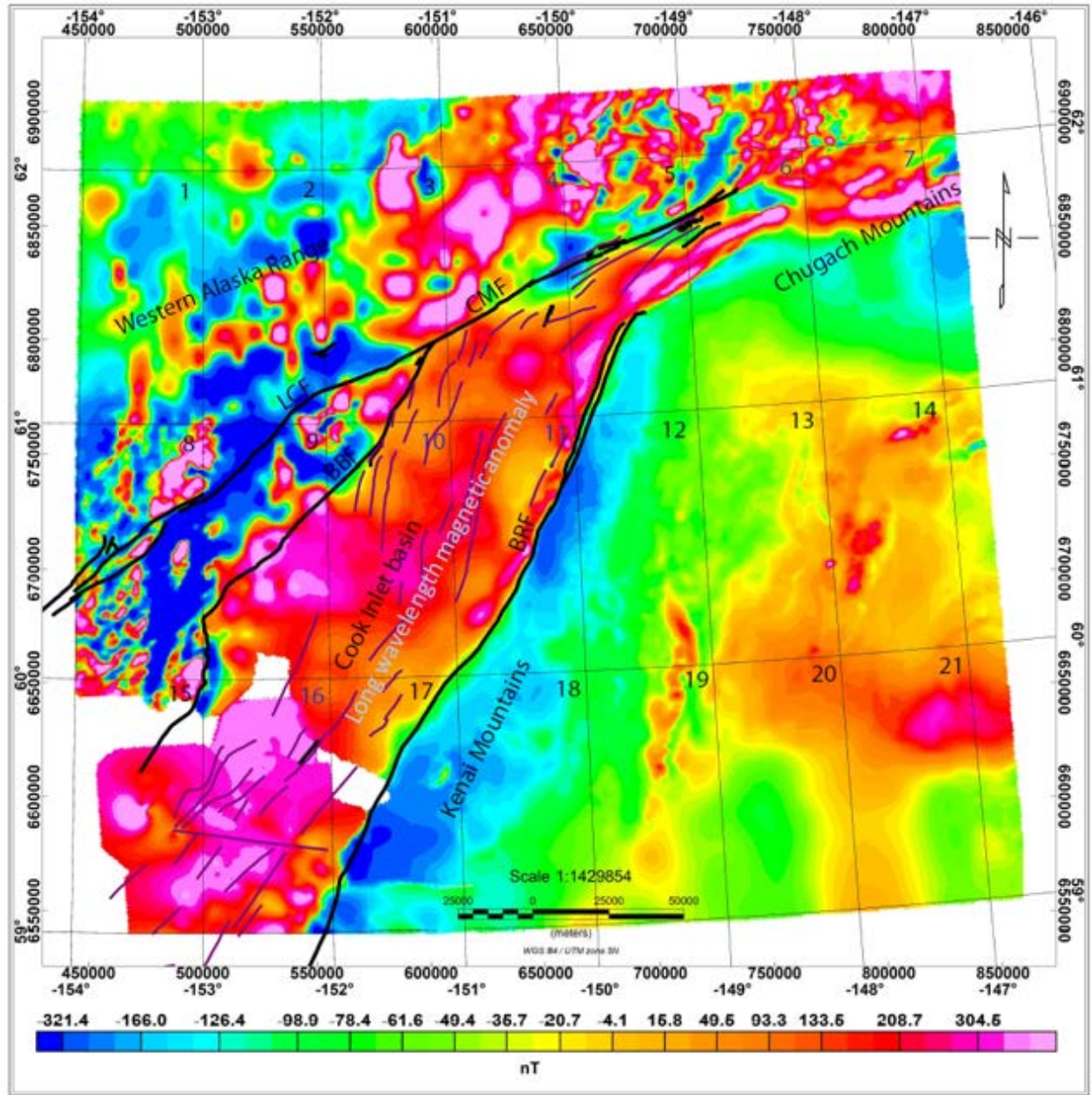


Figure 3: The aeromagnetic map shows long wavelength anomalies trending SW to NE within the CIB. The map is subdivided into 21 blocks as labeled.



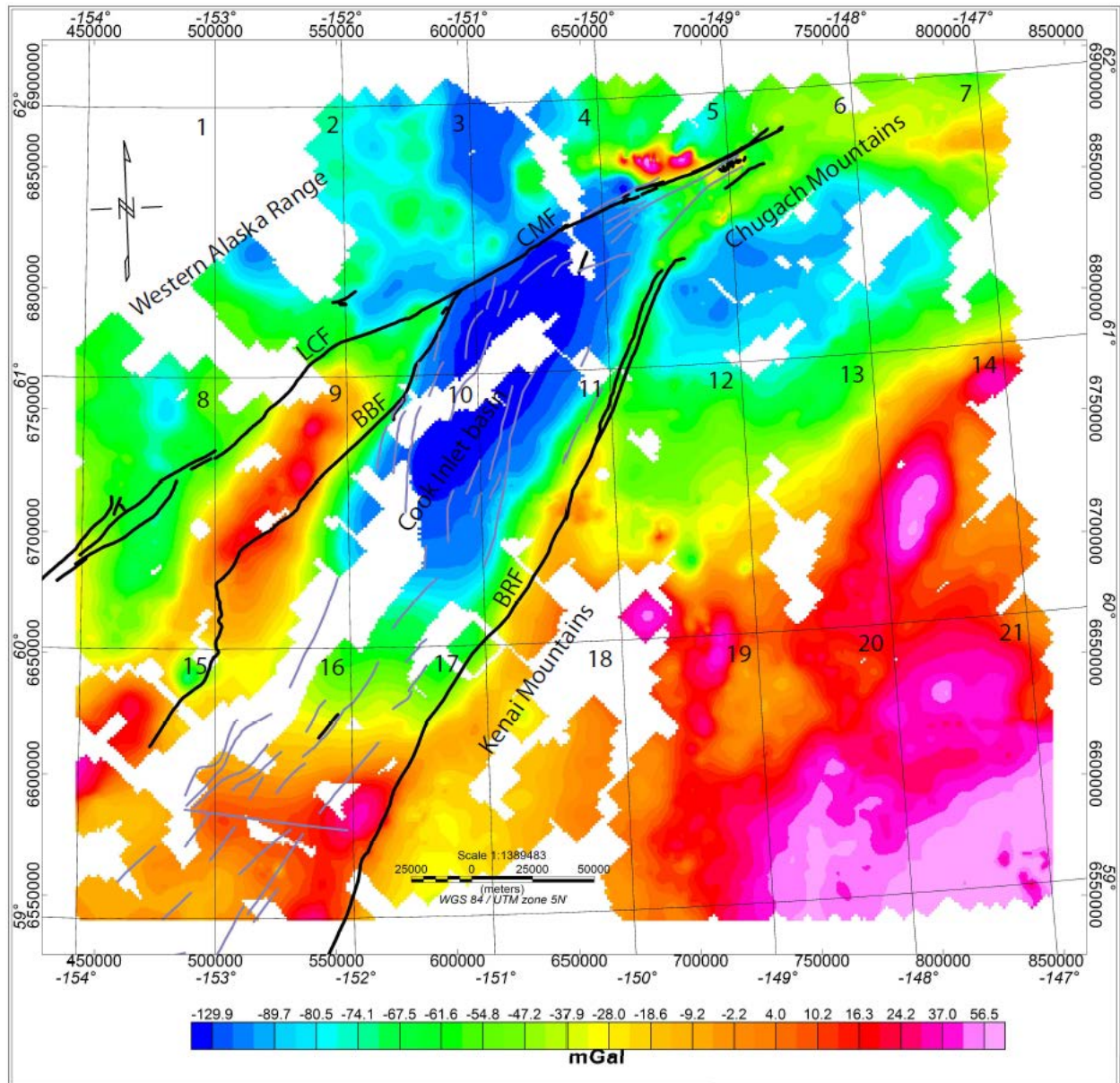


Figure 4: Complete Bouguer anomaly map of CIB showing a southwest to northeast trending long wavelength low gravity anomaly. Selected blocks for 3D inversion are 4, 6, 7, 10, 11 and 16.



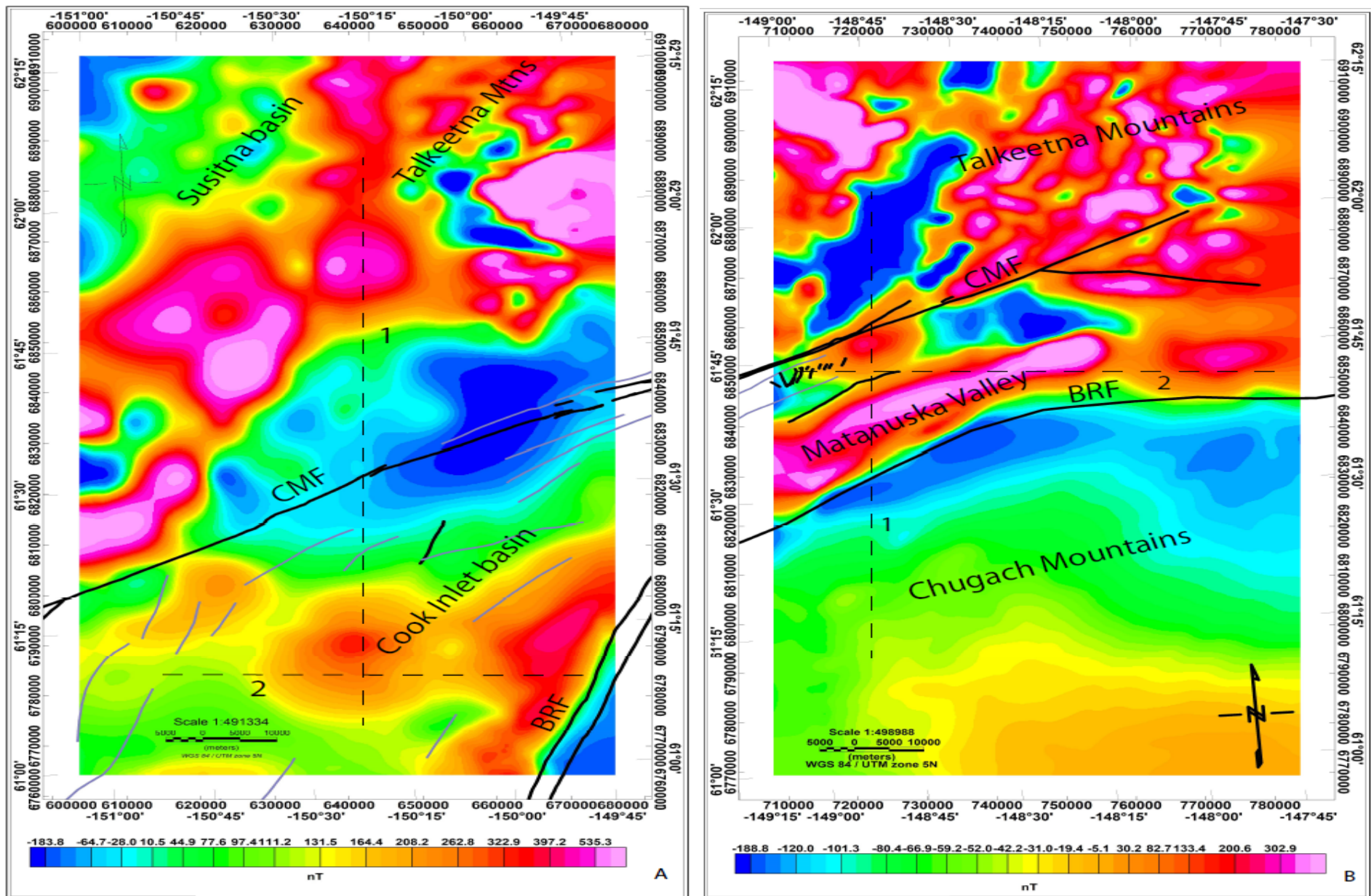


Figure 5a: Aeromagnetic map of block 4(A) and 6 (B). Lines 1 and 2 are used to show a west/east cross section and a north/south cross section of the inversion models (Figures 6a) respectively. CMF=Castle Mountain Fault, BRF=Border Range Fault.

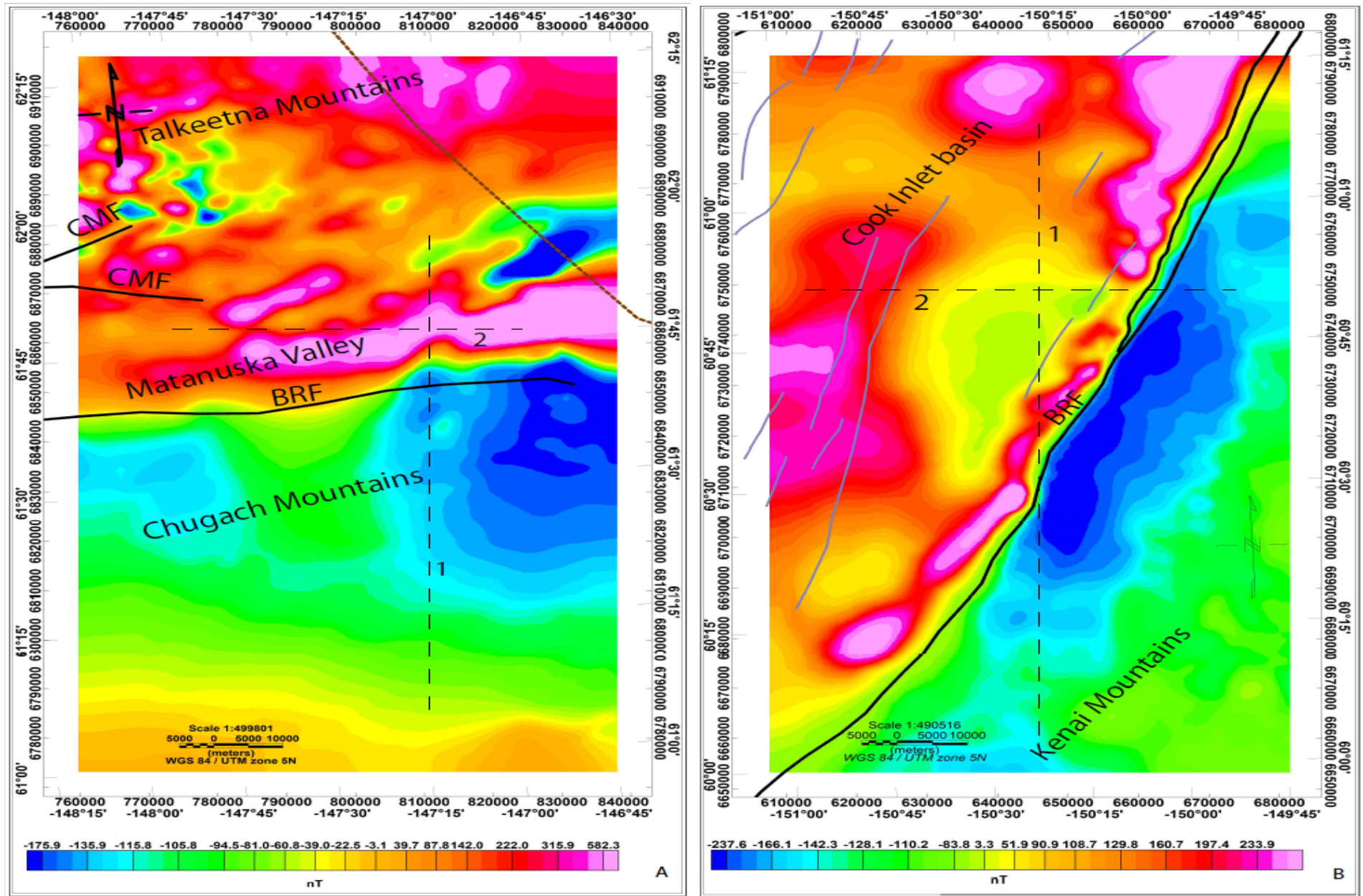


Figure 5b: Aeromagnetic map of block 7(A) and 11(B). Lines 1 and 2 are used to show the west/east face and north/south face cross sections of the inversion models (Figure 6b) . CMF=Castle Mountain Fault, BRF=Border Range Fault



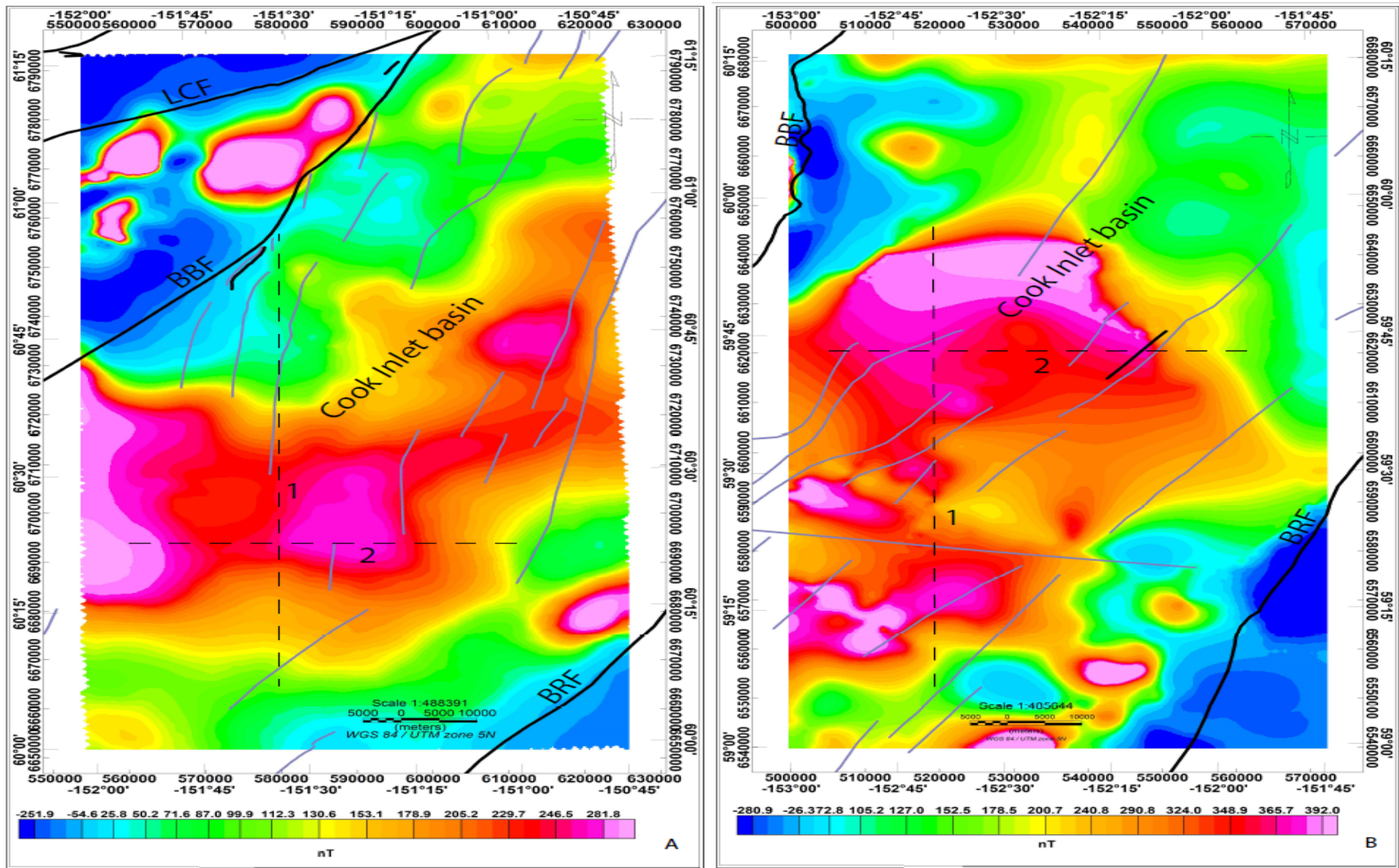


Figure 5c: Aeromagnetic map of block 10 and 16. The map on the on the left is block 10 and the map on the right is block 16. Lines 1 and 2 are used to indicate the west/east face and north/south cross sections of inversion models (Figure 6c). BRF=Border Range Fault, LCF= Lake Clark Fault, BBF= Bruin Bay Fault

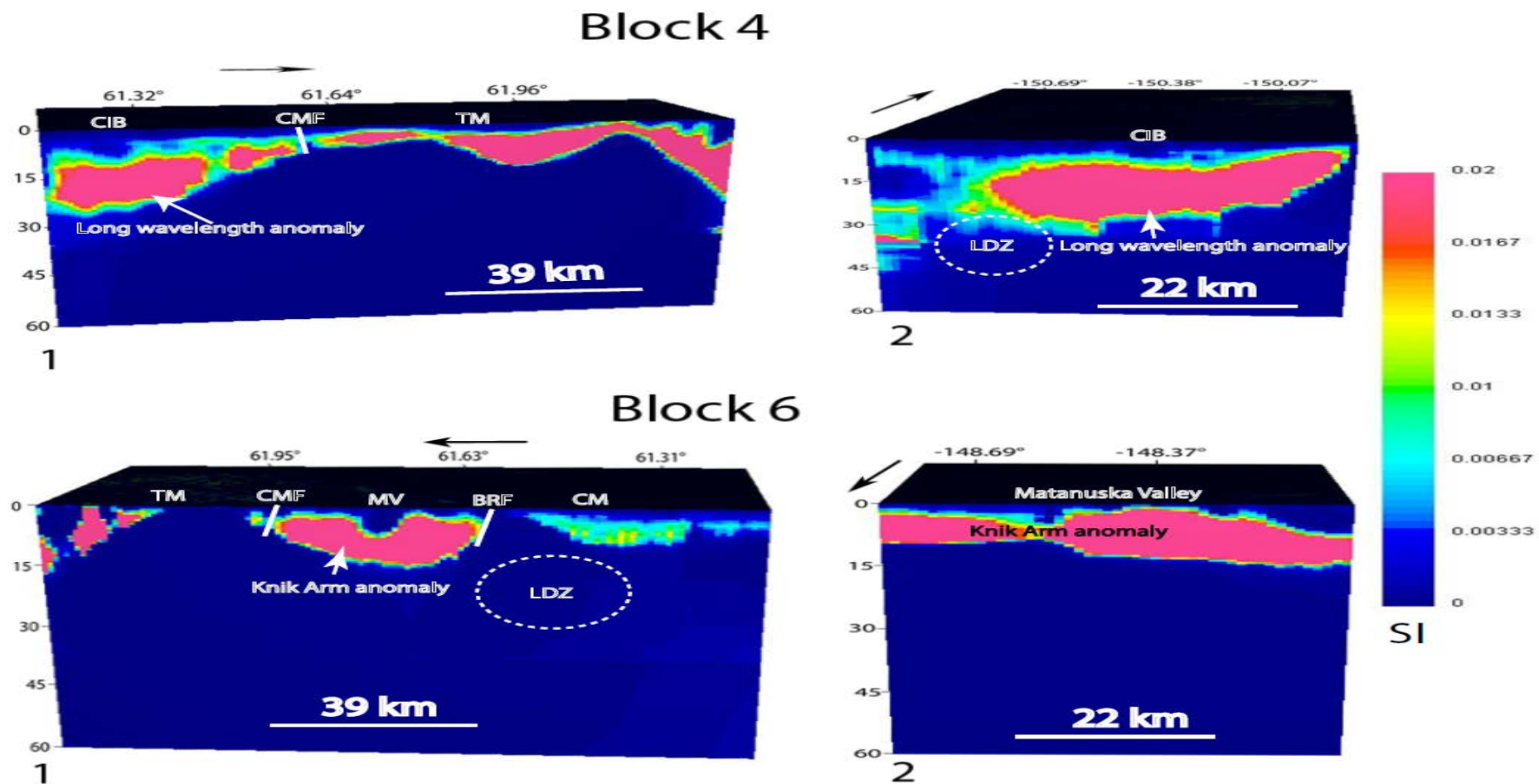
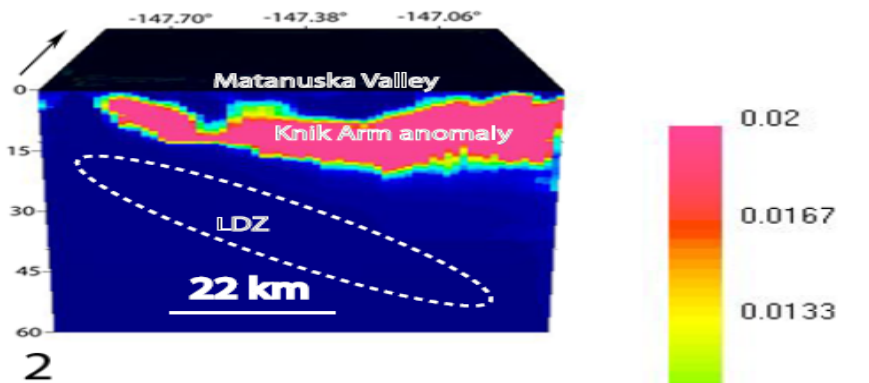
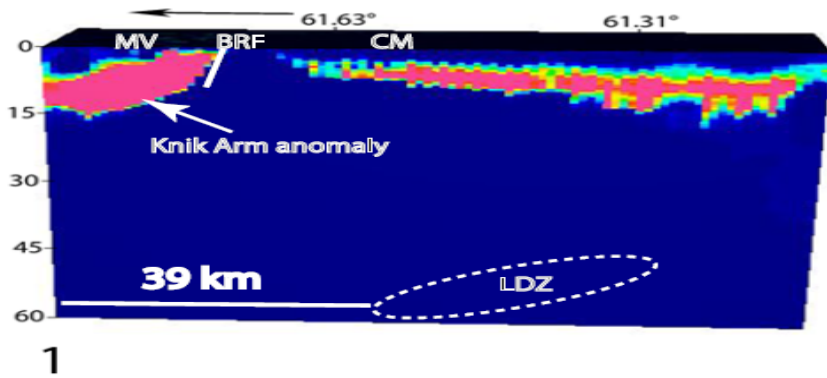


Figure 6a: Cross sections of 3D inversion models showing depth and geometry of magnetic susceptibility sources determined from inversion of magnetic anomaly data. Block 4(1) is the east face and block 4(2) is the south face, showing long wavelength anomalies within CIB and Talkeetna Mountains. Block 6(1) is the west face and block 6(2) is north face, showing long wavelength anomaly within Matanuska Valley. The black arrows point to the north and the scale of the vertical axis is in km. MV=Matanuska Valley, LDZ=Low Density Zone, CM=Chugach Mountains, BRF=Border Range Fault, CMF= Castle Mountains Fault, TM= Talkeetna Mountains, CIB= Cook Inlet Basin.

## Block 7



## Block 11

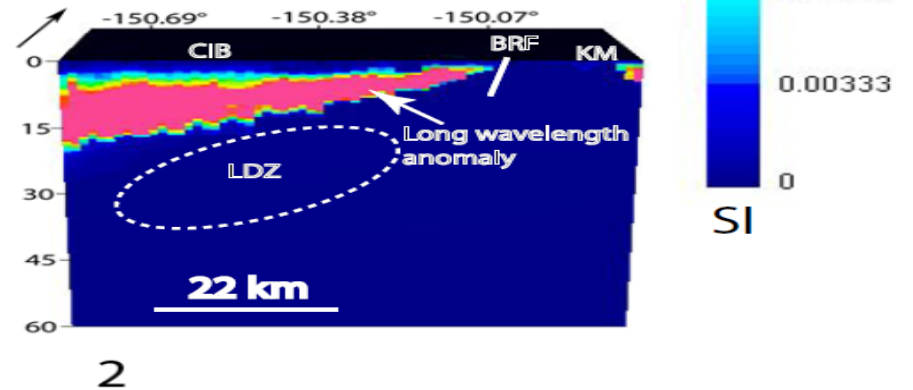
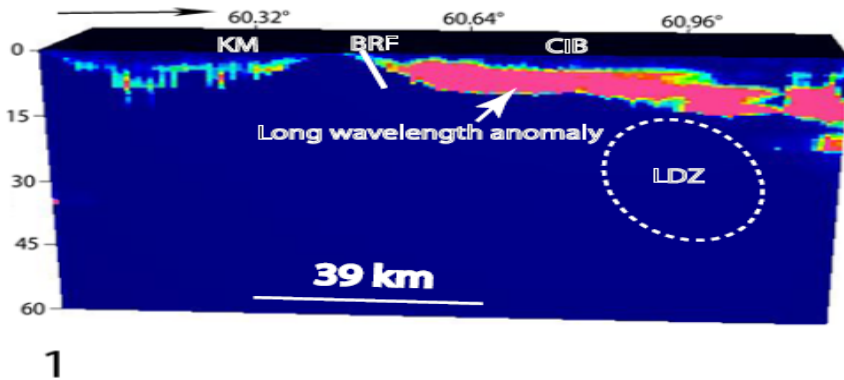
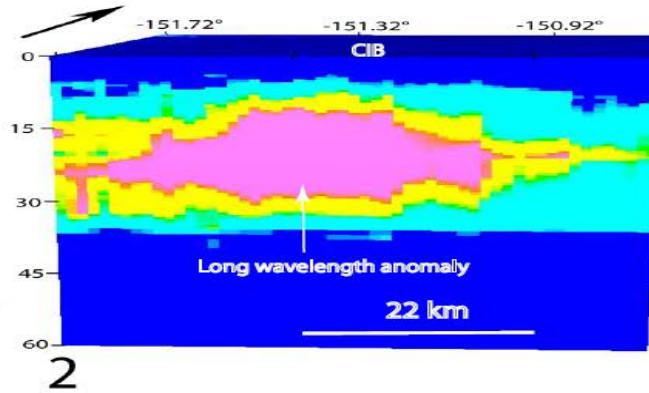
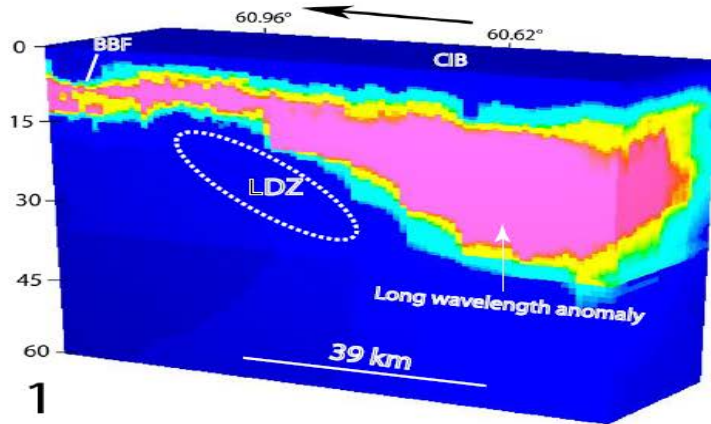


Figure 6b: Cross sections of 3D inversion models showing depth and geometry of magnetic susceptibility sources determined from inversion of magnetic anomaly data. Block 7(1) is the west face and block 7(2) is the south face, showing long wavelength anomalies within Chugach Mountains and Matanuska Valley. Block 11(1) is the east face and block 11(2) is south face, showing long wavelength anomaly within CIB and Kenai Mountains. The black arrows point to the north and the scale of the vertical axis is in km. MV=Matanuska Valley, LDZ=Low Density Zone, CM=Chugach Mountains, BRF=Border Range Fault, CIB=Cook Inlet Basin, KM=Kenai Mountains



## Block 10



## Block 16

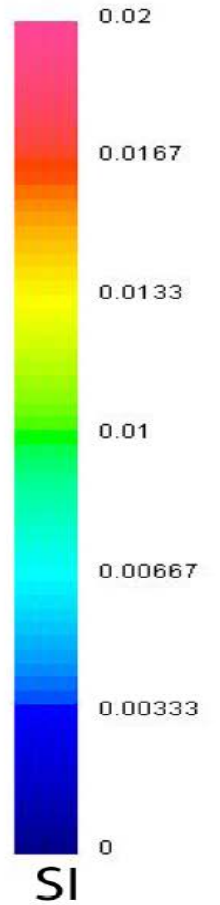
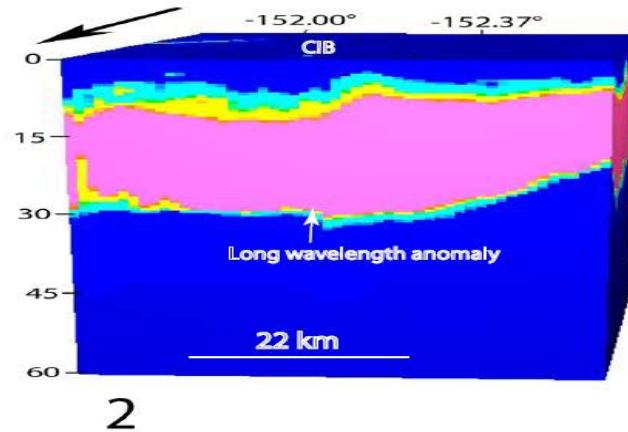
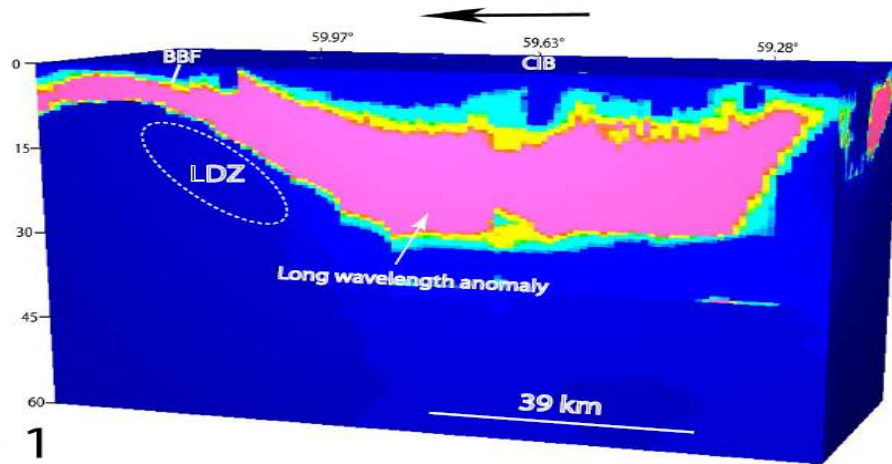


Figure 6c: Cross sections of 3D inversion models showing depth and geometry of magnetic susceptibility sources determined from inversion of magnetic anomaly data. Block 10(1) is the west face and block 10(2) is the south face, showing long wavelength anomalies within CIB. Block 16(1) is the west face and block 16(2) is north face, showing long wavelength anomaly within CIB. The black arrows point to the north and the scale of the vertical axis is in km. LDZ=Low Density Zone, BBF=Bruin Bay Fault, CIB= Cook Inlet Basin

### 2.3.4 POWER DENSITY SPECTRAL ANALYSIS

The Curie depth at which rocks lose their magnetic susceptibility is commonly determined using a spectral analysis method (Hussein et al., 2012, Mickus and Hussein, 2015). This method is very effective for determining the regional Curie depth by examining the spectral properties of the magnetic anomalies over a relatively large area (Shuey et al. 1977; Blakely 1988).

To calculate the depth to the bottom ( $Z_b$ ) of the magnetic source I used the technique described by Tanaka et al., (1999), Manea and Manea (2011), Hussein et al. (2012) and Mickus and Hussein (2015). This technique involves first estimating the depth to the top ( $Z_t$ ) of the magnetic source as described by Spector and Grant (1970) using a magnetized rectangular prism. Bhattacharyya and Leu (1975 and 1977) further determined the depth of the centroid ( $Z_c$ ) for the magnetic source. The depth to the bottom of the magnetic source corresponding to the Curie depth was estimated using the technique of Okubo et al. (1985) that was based on the spectral analysis method of Spector and Grant (1970).

The depth to the top of the magnetic source can be estimated by calculating the slope ( $s$ ) of a straight-line fitting the higher wavenumber portions ( $|k|$ ) of a plot of the radially averaged power density spectra ( $\ln [\Phi_{\Delta T} (|k|)^{1/2}]$ ) against wavenumber. The depth to the centroid can be estimated in a similar manner by first taking the slope of the straight-line fitting the lower wavenumber portions ( $|k|$ ) of the plot of the frequency-scaled power density spectra ( $\ln [(\Phi_{\Delta T} (|k|)^{1/2})/|k|]$ ) against wavenumber.  $\Phi_{\Delta T}$  is the total magnetic field anomaly. The depth to the top and centroid of the anomalies (in km) is estimated using the equation  $(-s/(4\pi))$  where  $s$  is given in cycles/km. The depth to bottom  $Z_b$  of the anomaly is calculated using the relation  $2Z_c - Z_t$ .

In this research, I used the 2D power density spectral method to estimate the depth of the source of the magnetic signature within the basin. Seven profile lines (figure 7) longer than the width of the anomaly are used to determine a reasonable estimate of the depth to bottom of these magnetic sources.



### 2.3.5 POWER DENSITY SPECTRUM ANALYSIS RESULT AND INTERPRETATION

The aeromagnetic anomaly maps show a dominating long wavelength, magnetic maximum over the CIB. The extent of the magnetic anomaly within CIB requires use of large size grid which is

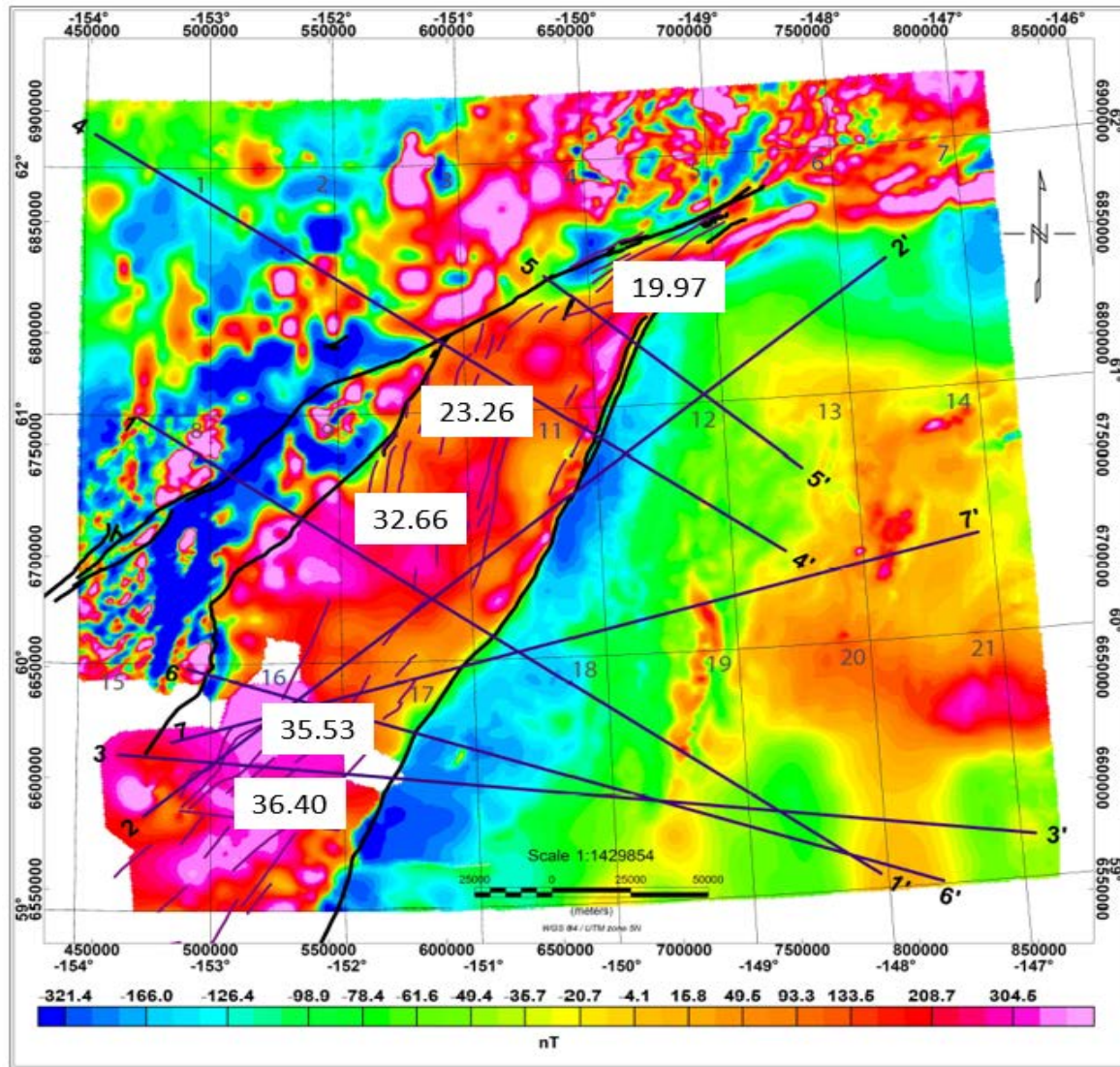


Figure 7: Aeromagnetic anomaly map randomly drawn white lines across positive long wavelength anomalies. There are seven lines labeled 1-1', 2-2', 3-3', 4-4', 5-5', 6-6' and 7-7'. The numbers in the white box are estimated depth to bottom from table 1 ( $Z_b$ , unit is kilometers).

equivalent to the total map area. Using the whole area only gives the highest value rather than the varying changes in intensity across the length of the whole basin. To get a reasonable estimate of  $Z_t$  as the source of the anomalies at various locations, profile lines were drawn across the sections of long wavelength anomalies with high magnetic amplitudes. Seven profile lines were drawn across the highest amplitude anomalies within the selected block used for the 3D magnetic modelling (Figure 7). Lines 4-4' and 5-5' are along the northeastern part of the CIB and 1-1', 2-2', 3-3', 6-6' and 7-7' are lines selected across the southwestern part of the CIB. The depth to top of the magnetic source is estimated from the slope along the plot of the two-dimensional radially averaged power density spectra ( $\ln(\text{Power})$ , Figure 8) for the high wavenumber (0.07 to 0.43 cycles/km) portion of the spectrum. Similarly,  $Z_c$  was also estimated using the same approach but with a low wavenumber (0.005 to 0.05 cycles/km). Figure 8 is an example of the power spectrum analysis showing the computed  $Z_t$  and  $Z_c$  of the magnetic source along the profile 4-4'. Identifying the position of where to measure the slope can influence calculation of the depth (Ravat et al., 2007). Several slope positions and measurements were conducted to ensure consistency. The errors for the estimates ranges from 0.2 to 0.5 km.  $Z_b$  of the anomaly is calculated using the relation  $2Z_c - Z_t$ . Table 1 shows the calculated values of the various lines selected across the anomalies. The  $Z_b$  value of lines 4-4' and 5-5' shows a shallow depth of ~23 km and 20 km respectively, consistent with the range of depths 14 to 26 km from the 3D inversion depths within blocks 4 to 7.  $Z_b$  of lines 1, 2, 3, 6 and 7 are in the range of 28.10 to 36.40 km (Table 1 and Figure 7). This range is consistent with the depths from the 3D inversion of blocks 10 to 16. In general, the spectral analysis shows  $Z_b$  is shallower in the northeastern part of CIB and deeper in the southwestern section corresponding to the trend identified in the 3D magnetic inversion.

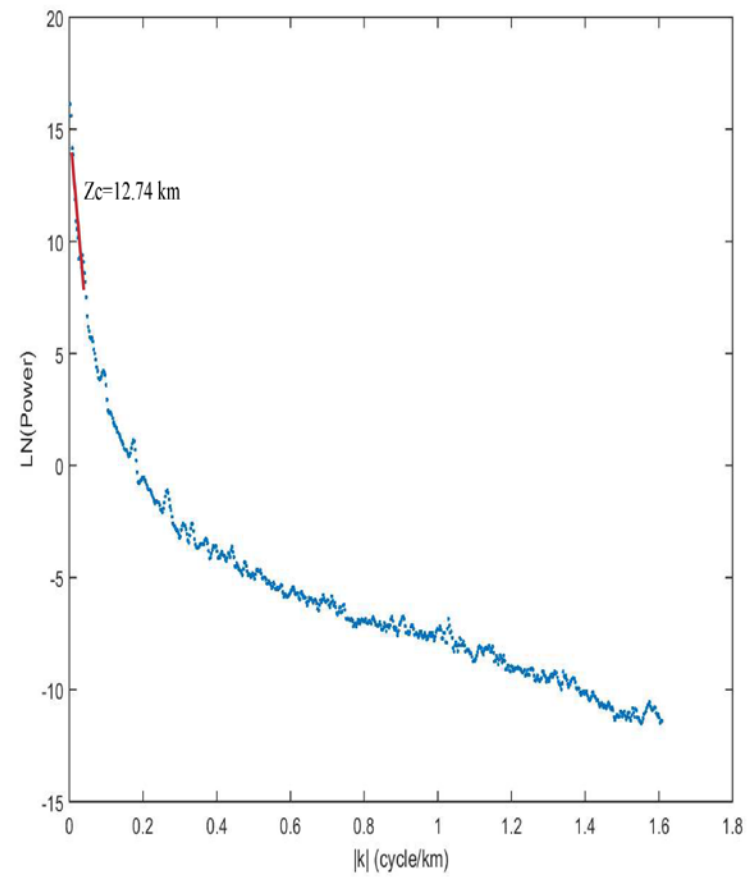
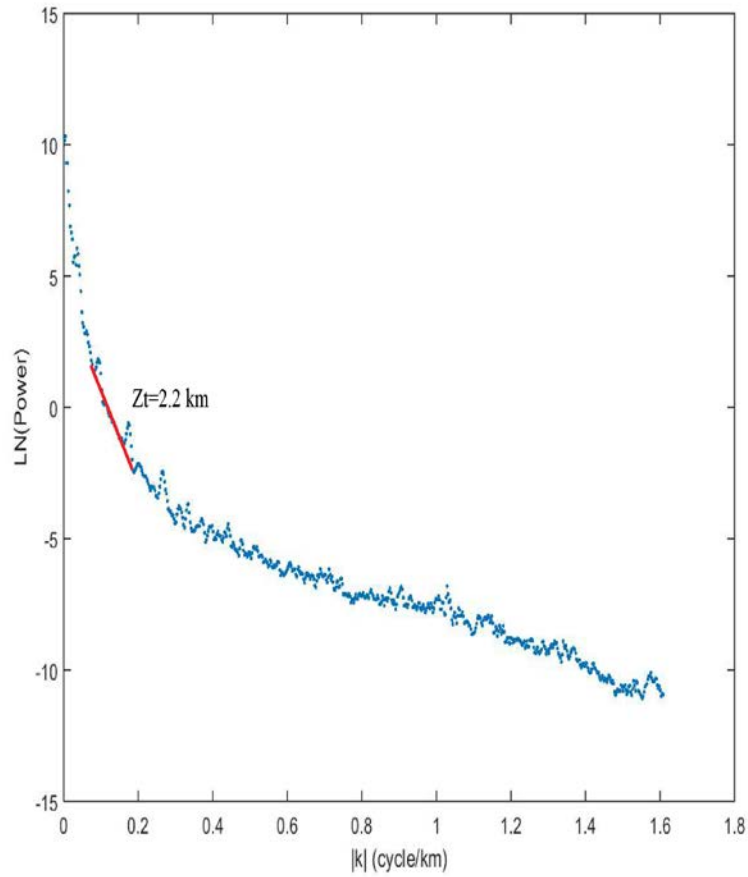


Figure 8: Example of the spectral analysis technique for line 4-4' (Figure 7). The left graph shows the depth estimate for the top of the magnetic source and the right graph shows the depth estimate of the centroid of the magnetic source. These depths are used to compute depth to bottom of the magnetic source or the Curie isothermal depth.

Table 1: Estimated depths of depth to top ( $Z_t$ ), centroid ( $Z_c$ ) and bottom ( $Z_b$ ) of high magnetic anomalies within the CIB.

Line Number	$Z_t$ (km)	$Z_c$ (km)	$Z_b$ (km)
1-1'	1.28	16.97	32.66
2-2'	1.45	18.49	35.53
3-3'	0.89	18.46	36.40
4-4'	2.24	12.74	23.26
5-5'	1.37	10.67	19.97
6-6'	1.40	14.75	28.10
7-7'	1.11	15.79	30.47

### 2.3.6 TEMPERATURE-DEPTH CURVES

Temperature variation with depth influences the rheological properties of the lithosphere (Chapman and Furlong, 1992). Batir et. al. (2016) calculated heat flow by determining the geothermal gradient and thermal conductivity from equilibrium temperature logs and borehole temperatures. These calculated parameters were also used to generate temperature-depth curves to a depth of 10 km. In this research, I used the parameters from Batir et al. (2016) to generate temperature-depth curves to a depth of 40 km to estimate the temperature at the bottom of the anomalies. Temperature values were computed using the technique developed by Blackwell et al. (2007) and Stutz et al. (2012). This technique incorporates heat flow, radiogenic heat generation and thermal conductivity (Carslaw and Jaeger 1959; Blackwell et al., 2007) of various rocks to estimate the temperatures at depth. The temperature values were computed using equations of Batir et al. (2016) and shown in appendix B.

Table 2: Values for temperature calculations for Alaska. Data for Anchorage were used in the temperature calculation for CIB and its vicinities). (Modified from Batir et al., 2016)

City	Sediment thickness (m)	Sediment conductivity ( $\text{W mK}^{-1}$ )	Basement conductivity ( $\text{W mK}^{-1}$ )	Sediment conductivity below 4 km ( $\text{W mK}^{-1}$ )	Surface heat flow ( $\text{mW m}^{-2}$ )	Mantle heat flow ( $\text{mW m}^{-2}$ )	Thickness of heat producing section (km)	Heat production of sediments ( $\mu\text{W m}^{-3}$ )	Heat production of basement ( $\mu\text{W m}^{-3}$ )
Anchorage	5000	2.5	2.4	2.7	64 – 55	30	10	1	2.9 – 2.0
Fairbanks	1000	2.5	2.4	N/A	100 – 87	60	10	1	3.9 – 2.6
Juneau	0	N/A	4.0	N/A	62 – 55	50	10	N/A	1.2 – 0.5
Alaska Peninsula	7000	1.8	2.4	2.7	73 – 53	30	13	1	3.6 – 1.6
Bristol Bay	7000	1.8	2.4	2.7	84 – 59	30	13	1	4.7 – 2.2
Copper River Basin	3000	2.5	2.4	N/A	85 – 60	60	10	1	2.2 – 0.3

### 2.3.7 TEMPERATURE-DEPTH CURVES RESULT AND INTERPRETATION

Temperature-depth curves (Figures 9) were generated for the CIB, Susitna basin and regions with igneous intrusions that are classified as basement or crustal rocks. A thickness of 5 km was used for the sedimentary units within the CIB as suggested by Kirschner and Lyon (1973). I used an estimated sedimentary thickness of 4 km to compute temperature values for the Susitna basin based on depths of 4-5 km estimated by Stanley et al. (2014). The curves generated consist of low and high limits based on a range of surface heat flow data and basement heat production. Temperatures at the base of sediments within CIB and Susitna basin varied due to different sediment thickness within these forearc basins. Temperatures at the bottom of sediments using 5 km (appropriate for CIB) is in the range of 97.8°C to 115.8°C using surface heat flow values of 55 mWm<sup>-2</sup> and 64 mWm<sup>-2</sup> (Batir et al., 2016). At the bottom of the Susitna basin temperature values range between 81.2°C to 95.6°C using the same range of surface heat flows that were used in the CIB. Using the Curie temperature of magnetite (~580°C), the corresponding depth of this temperature is reached within CIB, Susitna basin and areas of exposed basement rocks or intrusions were estimated. The depth of the Curie point within CIB ranged between 33.1 km and 39.4 km. The Curie isothermal depth within Susitna basin ranged between 33.6 km and 39.4 km. The Curie isothermal depth in the regions of exposed basement ranges from 36.8 km to 39.6 km. The depth range within the CIB from the temperature-depth profile is consistent with maximum estimated depth of 37 km from the magnetic inversion (Figure 6c) and 36.4 km from the spectral analysis on the southern divide of CIB (line 2-2' and 3-3' in Table 1 and Figure 7).

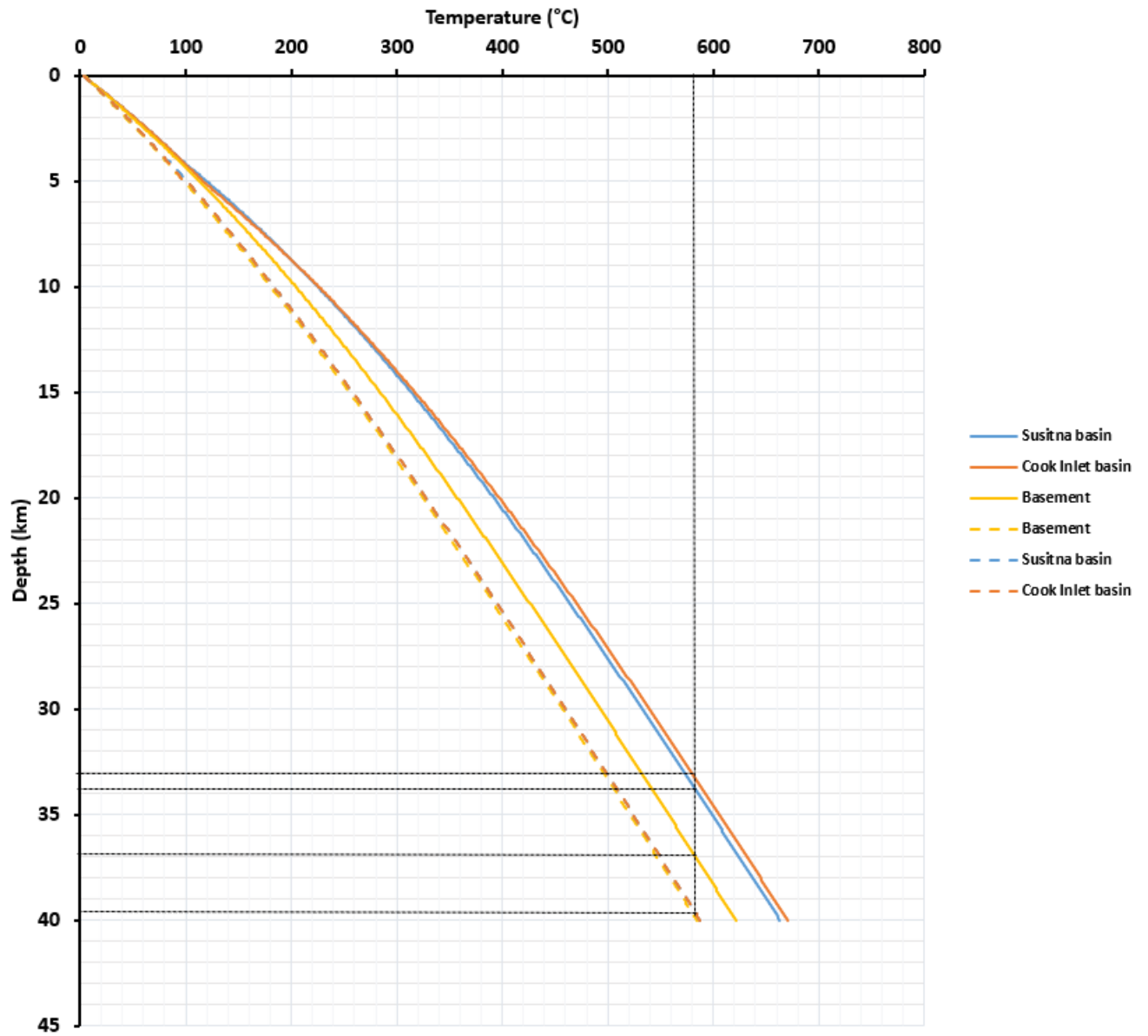


Figure 9: Temperature curves showing changes with depth. Black dotted lines show the estimated depths for approximate Curie temperature of 580°C. The dotted lines represent the temperature-depth curves using a surface heat flow value of 55 mWm<sup>-2</sup> and the solid lines represent temperature-depth curves using a surface heat flow value of 64 mWm<sup>-2</sup>.

### **2.3.8 GRAVITY METHOD**

Crustal thickness from magnetic and gravity studies in southcentral Alaska has been estimated to be between 40-50 km (Saltus et al., 2007). Isostatic gravity anomalies can be used to examine the structural features (He et al., 2014; Simpson et al., 1986; Zhang et al., 2010) within the CIB and to remove the effect of the Bouguer slab approximation in areas of varying crustal thickness (e.g., Haeussler and Saltus, 2011). Previous isostatic gravity anomaly maps have been developed by Haeussler and Saltus (2011) to define the location and extent of Tertiary structures and the mantle below the CIB. The isostatic residual anomaly map (Haeussler and Saltus, 2011) shows a large region of low anomalies related to Neogene deposits in the northern section of the basin.

The existing gravity data base (figure 4) has a total of 6300 stations with about 1400 gravity stations collected across the BRFS, the Kenai and Anchorage Lowlands from 2009 to 2011 by Mankhemthong et al., (2013) with the remainder obtained from land and marine regional gravity observations made before 2000 by the U.S. Geological Survey or extracted from the University of Texas at El Paso ( <https://research.utep.edu/default.aspx?tabid=37229> ) database Gravity data were also collected in 2013 over the western Susitna basin by U.S. Geological Survey (Saltus et al., 2016) With addition of recent gravity data within CIB, I generated a complete Bouguer anomaly map (Figure 4). To investigate the geometry and depth of deeper structures, the complete Bouguer anomaly data were inverted to estimate the depth to the source of the low gravity anomaly.

### **2.3.9 GRAVITY INVERSION**

Gravity analyzes are also used to investigate the nature of geological structures, for mapping bedrock topography, estimating thickness of sedimentary units and for natural resource exploration



purposes. Gravity data collected at the surface of the earth, are due to density contributions from a variety of shallow and deep structures within the earth. Even for noise-free gravity data, the interpretation is non-unique, as there are an infinite number of density models that can be generated to fit the observed data. There are several approaches to tackle the interpretation of gravity data including introduction of *a priori* (e.g., densities, depths to various bodies) into the inversion to constrain the model space or assigning variable densities to invert for the geometric shape of a model (Li and Oldenburg, 1998). Examples of studies that use density variations as a function of depth to invert for thickness of sedimentary structures include Oldenburg (1974), Pedersen (1977), Chai and Hinze (1988), Reamer and Ferguson (1989) and Guspi (1990). On the other hand, some inversions have been conducted on isolated anomalies using constant densities for 2D and 3D geometries (e.g., Pedersen, 1979). Additional *a priori* information has also been added to improve inversion models (e.g., Green 1975; Last and Kubik, 1983). The CIB is a structurally complex region and requires a complex 3D inversion approach that incorporates different types of *a priori* information and user-imposed constraints to generate density models that best define its geologic structures.

### **2.3.10 GRAVITY INVERSION RESULT AND INTERPRETATION**

Figure 4 is a complete Bouguer gravity anomaly map showing a long wavelength low gravity anomaly trending (blue region) south to north over the CIB. Inversion of Bouguer gravity anomaly data for blocks 4, 6, 7, 10, 11 and 16 (Figures 4, 10a, 10b and 10c) selected for the 3D magnetic inversion generates a density model (Figures 11a, 11b, 11c, 11d and 11e) of the crustal heterogeneities within the CIB. East or west face (line1) and north or south face (line 2) vertical slices along the same or close to the location of the magnetic inversion slices were analyzed to compare depth location of these anomalies. Like the magnetic inversions, the blocks are modelled

from gravity data, and profile lines are selected to show the side faces. Lines 3 (east or west face) and 4 (north or south face) were chosen as additional lines to analyze the sources of the Bouguer gravity minima. The above lines are only assigned for blocks 7, 10, 11 and 16.

The Bouguer gravity anomaly maps generated for the selected blocks (Figures 11a, 11b and 11c) shows zones of high intermediate and low gravity anomalies. This 3D inversion maps out the geometry and location of high and low gravity anomalies within the blocks. Block 4 shows CIB (Figure 10a) dominated by low to intermediate Bouguer anomaly. The inversion, at southern face, show low density zone (LDZ) beneath CIB at  $>20$  km. The Susitna Basin north of the western CMF intermediate Bouguer anomaly with the southwestern and eastern rims dominated by high Bouguer anomaly (figure 16a). Block 6 and 7 (Figures 10a and 10b) shows high Bouguer anomaly within the Matanuska Valley and the Talkeetna Mountains. The Chugach Mountains are controlled by low to intermediate Bouguer anomalies. The inversion result of block 6 shows a high density zone (HDZ) beneath Matanuska Valley (depth to top  $\sim 5$  km) and LDZ (depth to top  $\sim 15$  km) located below Chugach Mountains (Figure 11a). Block 7 inversion (Figure 11b) shows an extension of the HDZ and the LDZ (the depth to top  $\sim 12$  km below BRF). High, intermediate and low Bouguer anomalies are seen at the center of CIB basin within blocks 11 and 10 and 16 (Figure 10b and 10c). The southern edge also shows high Bouguer anomaly as shown in block 10 and 16 (Figures 10c). The LDZ beneath CIB is mapped within block 11 (Figure 11c) at a depth  $> 15$  km. This LDZ extends west and south into block 10 (Figure 22) and 16 (Figure 23) respectively with an average depth to top  $\sim 15$  km. HDZ are mapped in block 11 and extends into the block 16 at the eastern edge of the southern CIB and extends into Kenai Mountain. Block 10 also shows a mapped HDZ towards the western edge, beneath BBF, of CIB at a depth  $>5$  km.

The intermediate Bouguer anomalies within the Susitna basin shows anomaly with approximate range of -128.4 to -112.7 mGal and likely reflects response of thicker sedimentary basin strata with estimated thickness of ~4-5 km (Stanley et al., 2014). The high Bouguer anomaly at the southwestern rim of Susitna basin corresponds to igneous and metavolcanics rocks of the Susitna and Beluga Mountains. High Bouguer anomaly east of the Susitna basin, Talkeetna Mountain, reflects the presence of igneous and metamorphic rocks. The high Bouguer anomaly beneath the Matanuska Valley corresponds to a linear trending gravity high within the valley (e.g Barnes, 1977; Barnes et al., 1994) and coincides with the location of the Knik Arm magnetic anomaly. The southern CIB, block 10 and 16 (Figure 11c), with Bouguer anomaly > -93 mGal are likely controlled by thick crustal rocks based on interpretation from magnetic inversion of block 10 and 16. The high Bouguer anomaly > south of CIB, block 11 and 16 (Figure 11b and 11c), along the eastern edge of the basin into the Kenai Mountain corresponds to border range ultramafic and mafic assemblages (BRUMA).

The low Bouguer anomaly values within CIB can be interpreted as gravity response from thick sedimentary basin or the presence of low density zone at depth. Ambient noise tomography results from Ward (2015) shows low velocity zone beneath CIB mapped within a depth 10.5 to 34.5 km with a northward migration of the anomaly depthwise. The results interpreted as an effect of the presence of a thick sedimentary basin. This supports an earlier interpretation by Eberhart-Phillips et al. (2006). Both authors extended interpretation to Susitna basin and argued a possibility of similar basin properties and thickness to CIB but the low velocity zone mapped beneath the CIB is widely extensive and pronounced compared to a very little defined low anomaly below Susitna basin. In contrast, Saltus et al. (2016) argued variation in characteristics of CIB, a 200 Ma with 8 km thick (LePain et al., 2013), and Susitna basin, a 60 Ma with 4-5 km thick (Saltus et al., 2014).

If the CIB is older, sedimentary rock in this basin will be more compacted and will have higher density which will reduce smearing of seismic waves. Therefore, low velocity zone should be well pronounced under Susitna basin than CIB. Additionally, Mankhemthong et al. (2012) modelled a serpentinized block beneath the basin within a range of 16 to 34 km with a density of 2.8 g/cc. If there is serpentinized rocks below there should be high velocity perturbation below the CIB. In contrast, gravity inversion from the block 4, 10, 11 and 16 shows a LDZ > 15 km. Block 4 cuts through two basins (Susitna and CIB) but the inversion only images the low density zone beneath the CIB and not Susitna basin. Similarly, the gravity inversion of block 6 and 7 shows a low density zone at a depth >12 km beneath the Chugach Mountains. This zone has been imaged by Eberhart-Phillips et al. (2006) and Ward (2015) as Yakutat subducting plate. The Bouguer anomaly values within the Chugach Mountains are < -101.1 mGal compared to <-139.0 mGal beneath CIB. Estimating density of the LDZ from the density contrast scale of the inversion, using intrusive rocks mapped in the inversion as constraint, gives values in the range of 2.1 to 2.4 g/cc. Seismic imaging of the along the EDGE transect further south of CIB conducted by Ye et al., (1997) shows the presence of a thick low velocity zone interpreted as a thick underplated continental fragment, seamounts or plateau involved in the development of the terrane. Based on the results from the inversion, I argue that it is highly possible the Bouguer anomaly with the CIB is controlled by not only the basin but also deeper source at an estimated depth >15 km along the SW to NE axis of the low Bouguer anomaly within the basin. Further analysis of the result is done by comparing the LDZ with earthquake and GPS data.

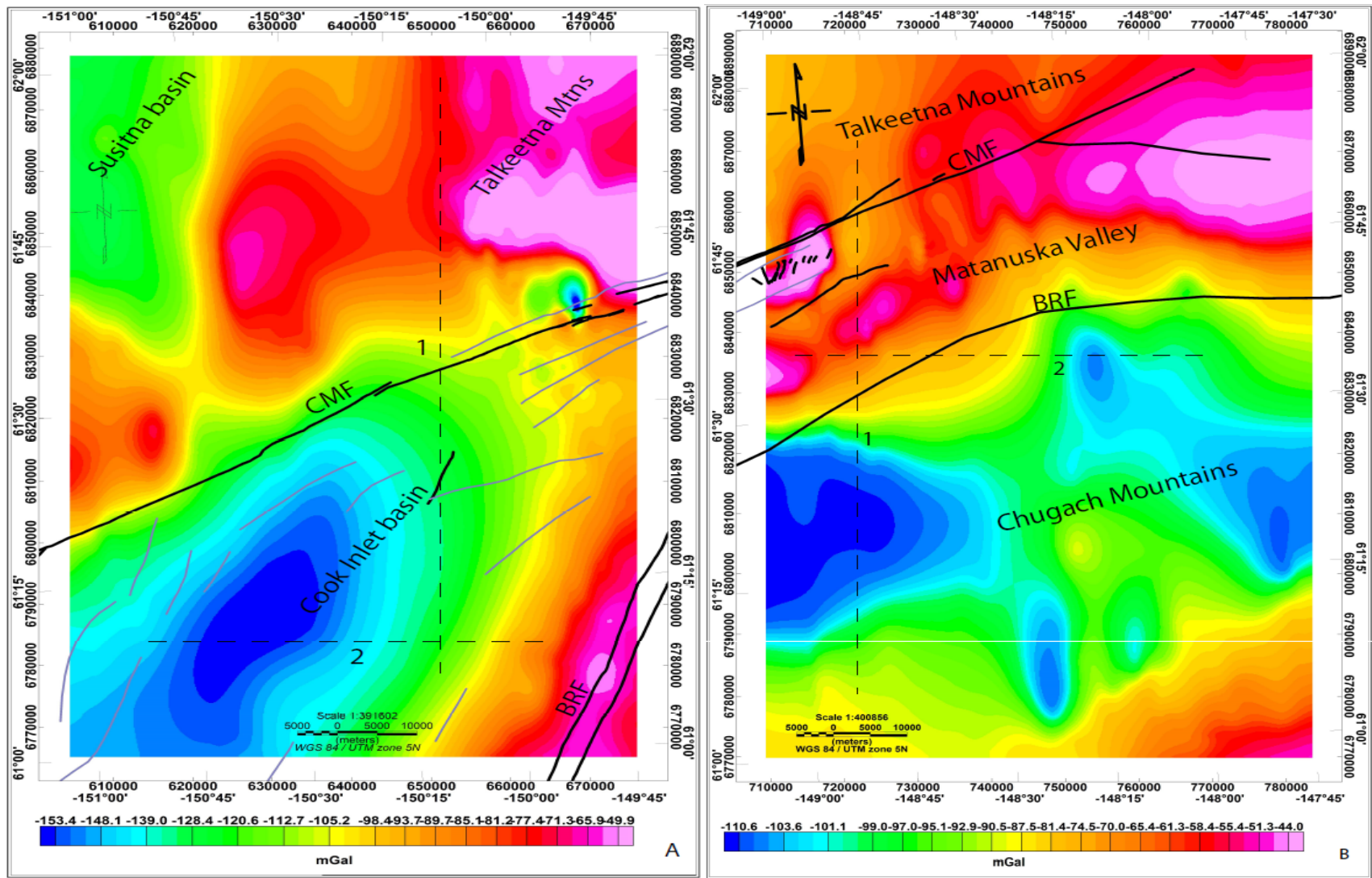


Figure 10a: The Bouguer gravity anomaly maps for block 4 (A) and 6 (B). Lines 1 and 2 are used to indicate the west/east face and north/south cross sections of inversion models (Figure 11a). CMF=Castle Mountain Fault, BRF=Border Range Fault

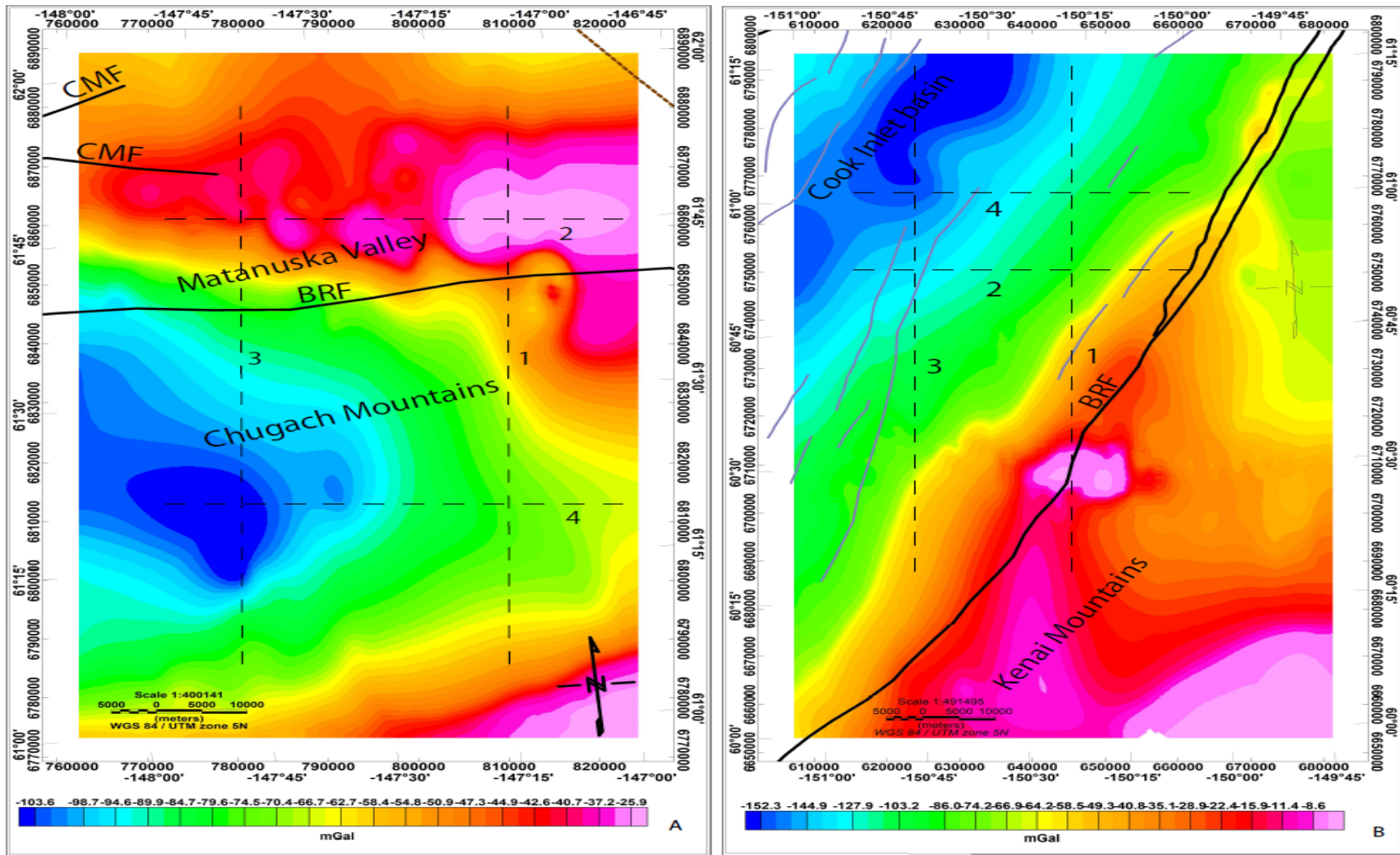


Figure 10b: Bouguer gravity anomaly maps for blocks 7 (A) and 11 (B). Line 1, 3 represents west/east faces and 2, 4 represents north/south cross sections of inversion models (Figures 11b and 11c). CMF=Castle Mountain Fault, BRF=Border Range Fault



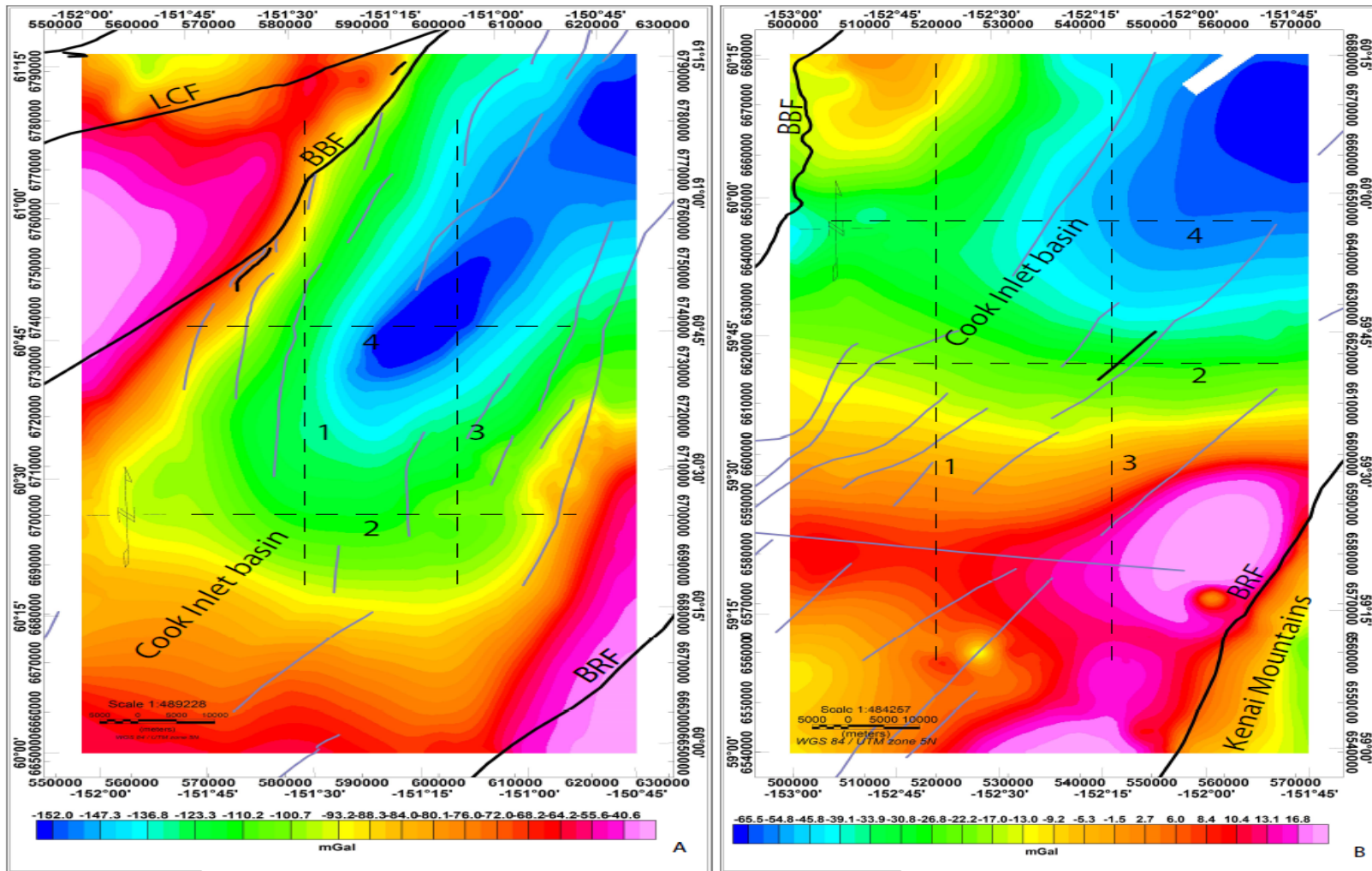


Figure 10c: Bouguer anomaly maps for blocks 10 (A) and 16 (B). Line 1, 3 represents west/east faces and 2, 4 represents north/south cross sections of inversion models (Figures 11d and 11e). BRF=Border Range Fault, LCF= Lake Clark Fault, BBF= Bruin Bay Fault

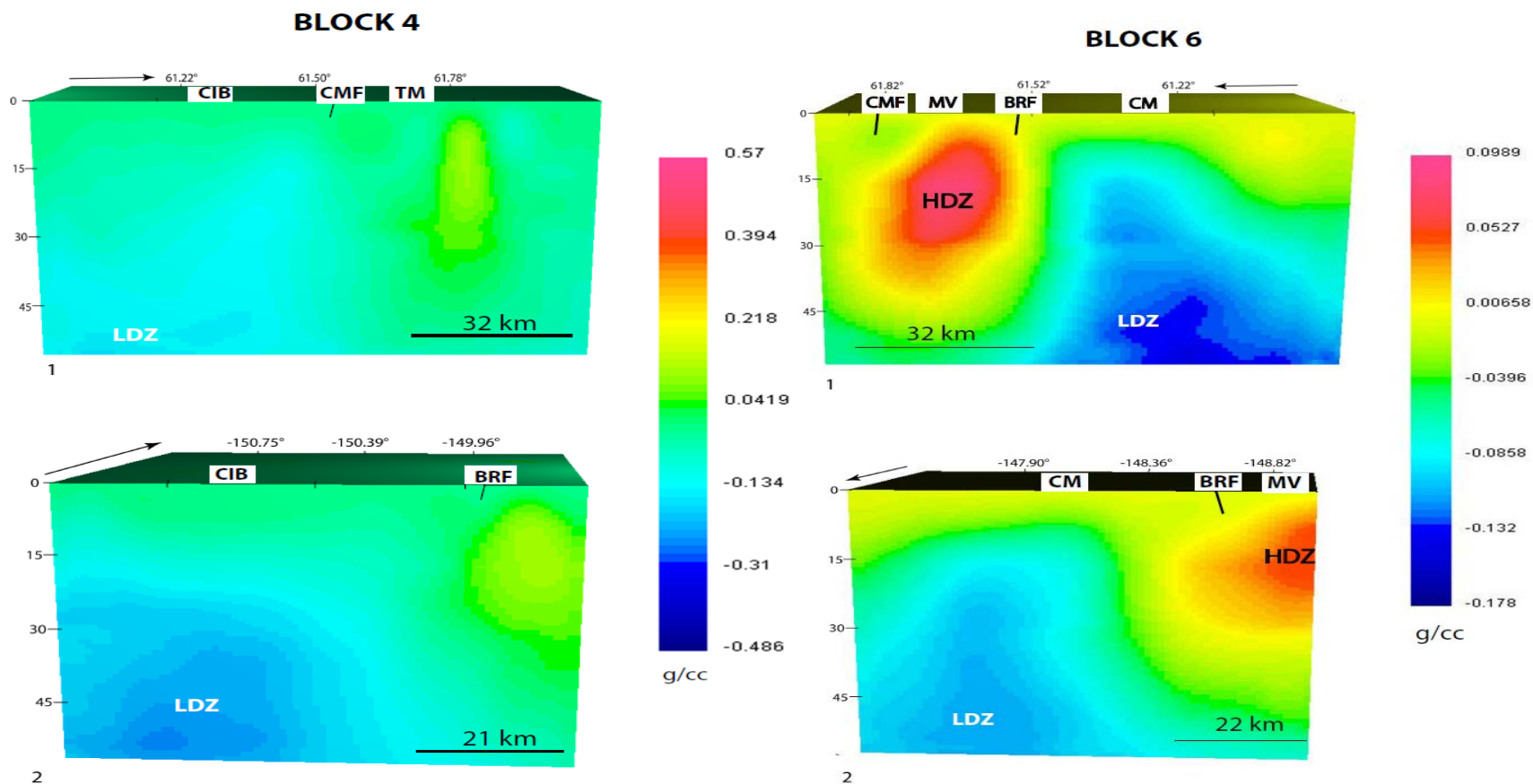


Figure 11a: 3D gravity inversion models. 1 and 2 on the left side are the east and south cross sections of the block 4. 1 and 2 on the right side are the west and north faces respectively of block 6. The black arrows point to the north and the scale of the vertical axis is in km. MV=Matanuska Valley, LDZ=Low Density Zone, CM=Chugach Mountains, BRF=Border Range Fault, HDZ=High Density Zone, CMF= Castle Mountains Fault, TM= Talkeetna Mountains, CIB= Cook Inlet Basin



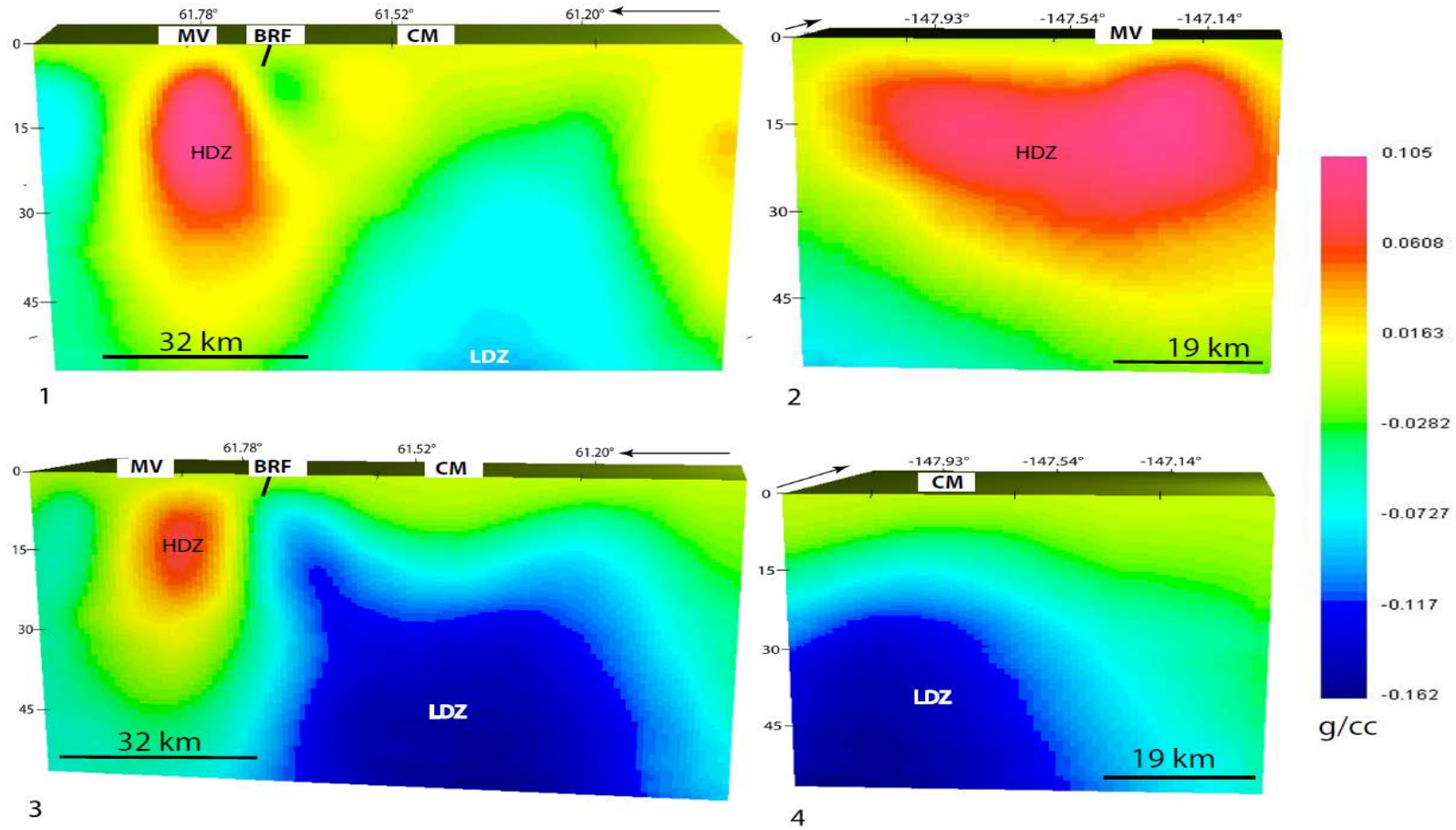


Figure 11b: 3D gravity inversion model for block 7. 1 and 3 are west cross sections. 2 and 4 are the south cross sections. The black arrows point to the north and the scale of the vertical axis is in km. MV=Matanuska Valley, LDZ=Low Density Zone, CM=Chugach Mountains, BRF=Border Range Fault, HDZ=High Density Zone.

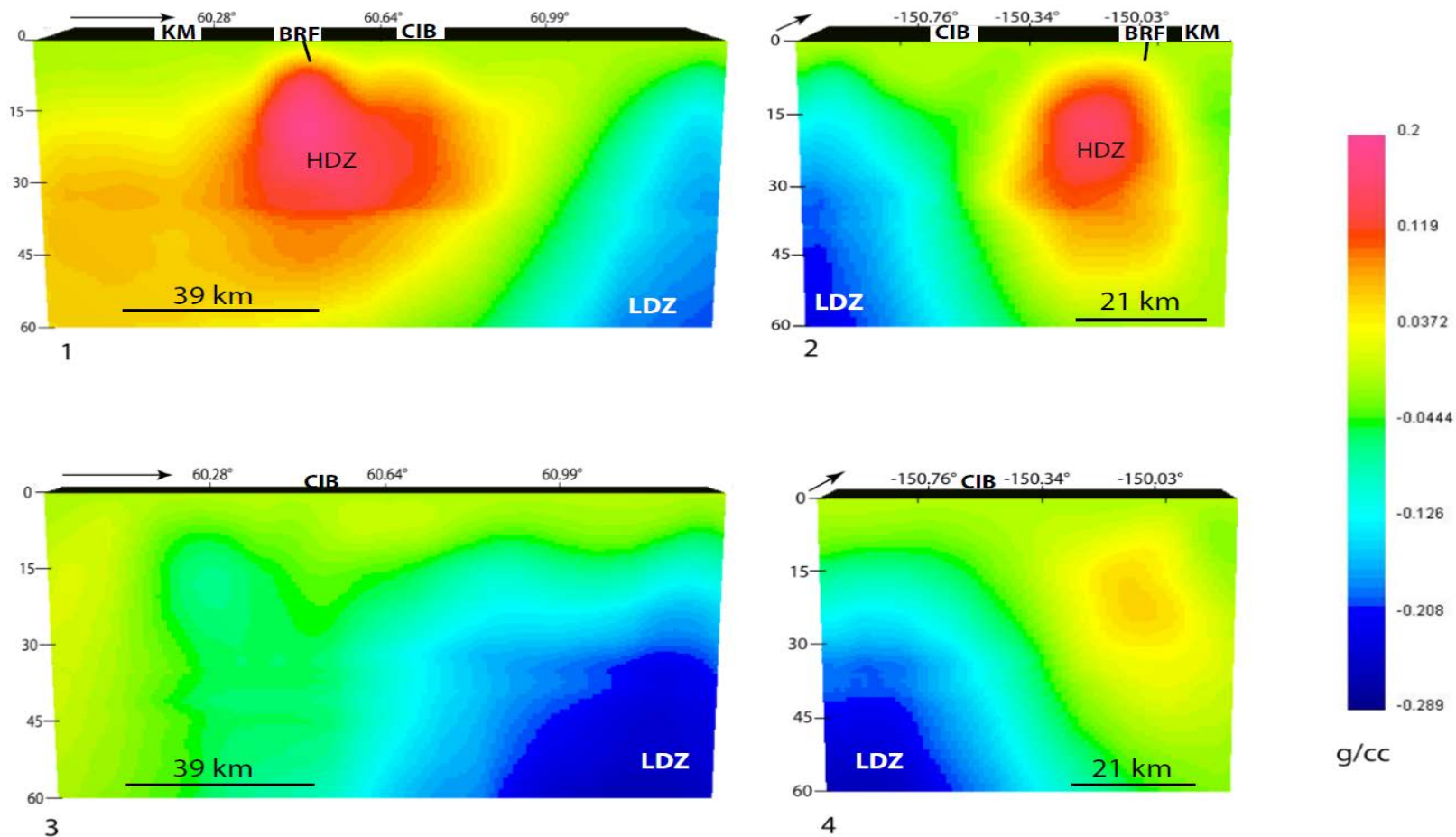


Figure 11c: 3D gravity inversion model for block 11. 1 and 3 are east cross sections. 2 and 4 are the south cross sections. The black arrows point to the north and the scale of the vertical axis is in km. CIB=Cook Inlet Basin, LDZ=Low Density Zone, KM=Kenai Mountains, BRF=Border Range Fault, HDZ=High Density Zone

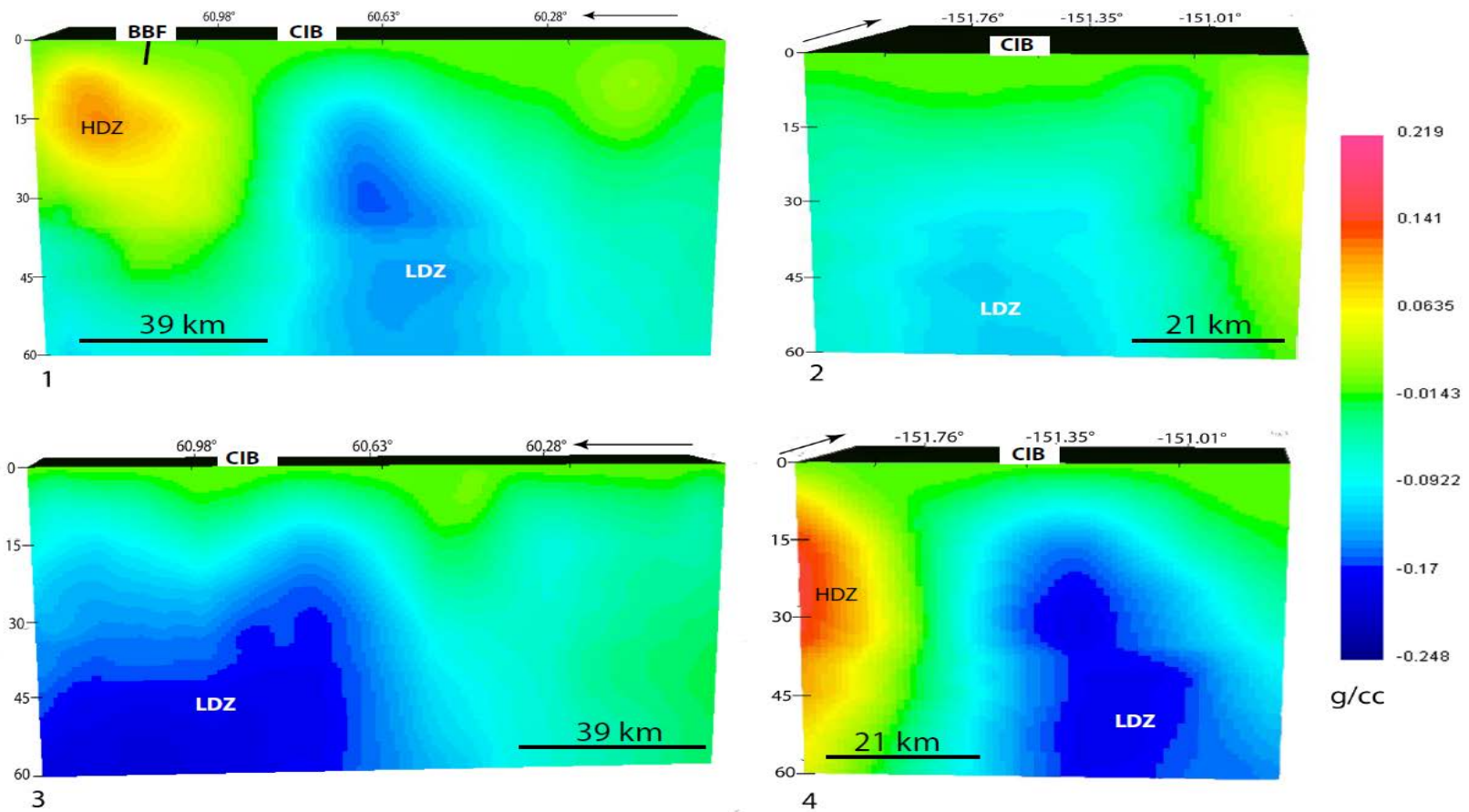


Figure 11d: 3D gravity inversion model for block 10. 1 and 3 are west cross sections. 2 and 4 are south cross sections. The black arrows point to the north and the scale of the vertical axis is in km. LDZ=Low Density Zone, BBF=Bruin Bay Fault, HDZ=High Density Zone, CIB= Cook Inlet Basin

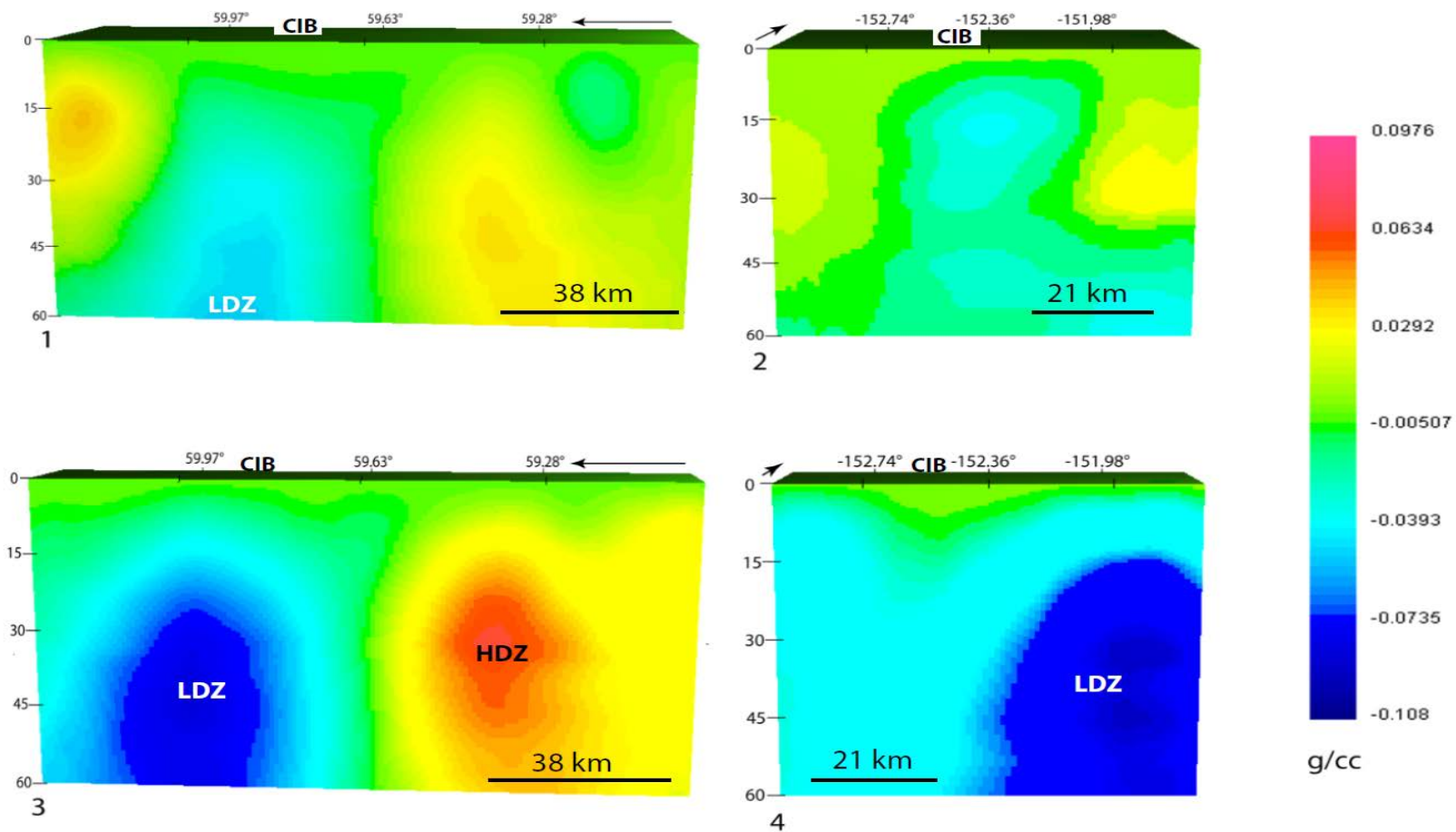


Figure 11e: 3D gravity inversion for block 16. 1 and 3 are west cross sections. 2 and 4 are south cross sections. The black arrows point to the north and the scale of the vertical axis is in km LDZ=Low Density Zone, HDZ=High Density Zone, CIB= Cook Inlet Basin

## 2.4 COMPARING RESULTS WITH EARTHQUAKE AND GPS INFORMATION

The results from the magnetic and gravity inversions are compared with Silwal et al. (2018) relocated seismic events that occurred from 1971 to 2001 and shown in figure 12. Generally magnetic anomalies lie above the Curie depth and magnetic inversion within CIB shows depth of magnetic sources, identified as section of the Southern Alaska Deep Magnetic High, within crustal thickness. Shallow earthquakes within CIB have been associated with the underlain high magnetic anomalies (e.g. Doser and Veilleux, 2009). Figure 12 is a complete Bouguer anomaly map overlain by earthquake events. The events are in three categories, the black cross represents events at a depth less than 10 km, the black dots represent events between 10 to 20 km and the chocolate colored triangles represents events at a depth  $>20$  km. Three profiles are selected on the map to look at the location of the earthquakes with mapped estimate of the low-density zone within CIB based on the 3D inversion results. Figure 12 shows intense shallow seismic events occurring within a depth of  $< 20$  km in the region of low Bouguer anomaly beneath CIB. Doser and Veilleux (2009) also identified seismicity at depth  $< 20$  km within CIB and noted that this region is characterized by greater relaxation (i.e coupling coefficient  $>0$ ). Profile 1 (Figure 13a) shows concentration of earthquakes on the overriding north American plate with a shallow depth of approximately 18 km, increasing to  $\sim 40$  km toward the eastern boundary of the low-density zone beneath CIB. There is a large concentration of upper crustal seismicity corresponding to the result from Flores and Doser (2005). The low-density zone is mainly characterized by less seismic activities. South to the low-density zone is a cluster of seismic events at a depth  $>20$  km (Figure 12). Profile 2 (Figure 13b) shows these events delineating the downgoing plate beneath CIB with the depth range of seismicity inferring the earthquakes are a combination of lower crust, interplate and intraslab events. Profile 3 (Figure 13c) is a south to north vertical profile that is parallel to and cut through the strike of the



downgoing plate. The three profiles show little amount of seismic events within the LDZ and is possible the material formation within this zone is dominantly aseismic.

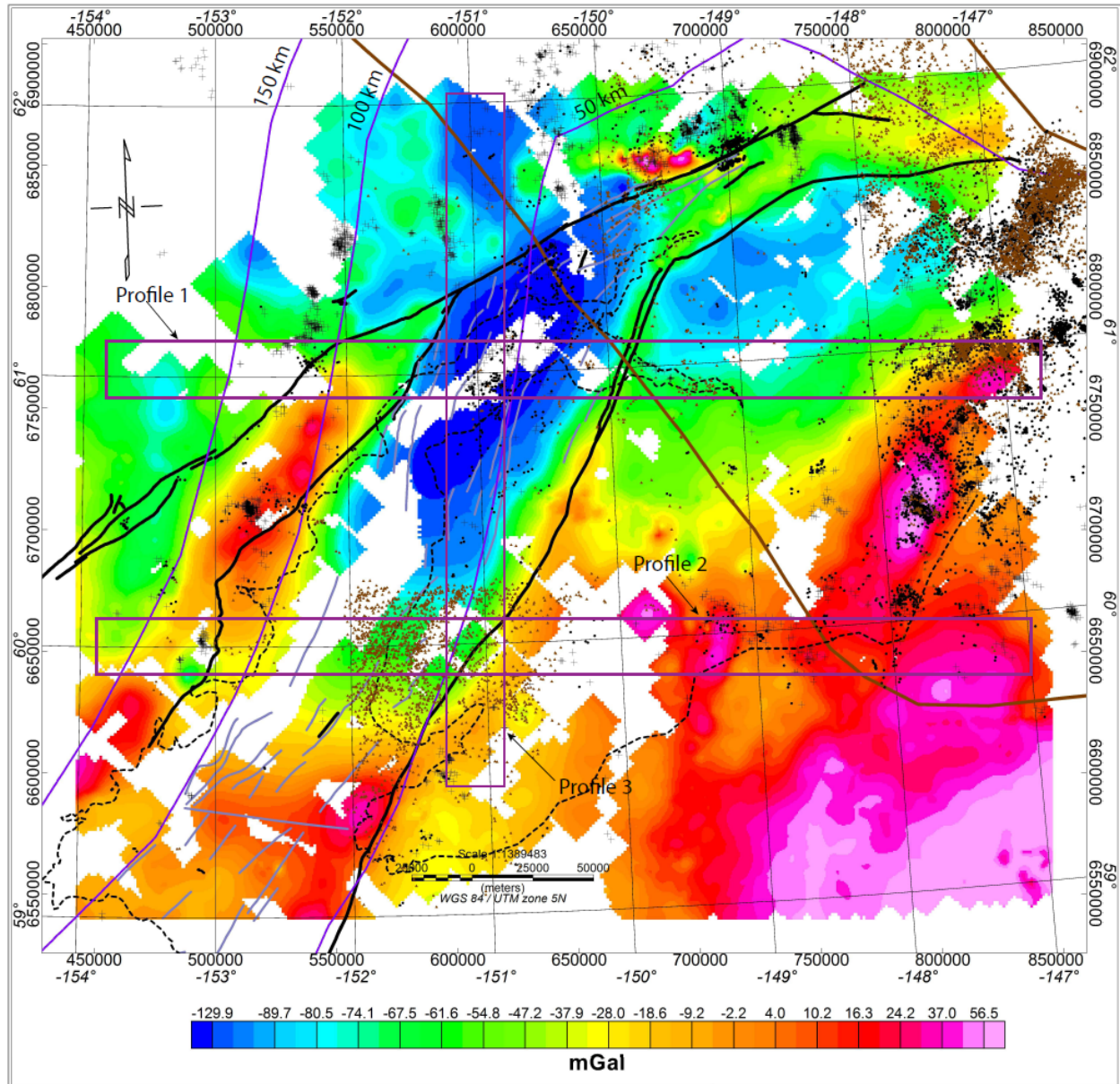


Figure 12: Earthquake relocated events superimposed on the Complete Bouguer gravity map: black plus symbols are shallow depth of <10 km, black dots are depths between 10 to 20 km and the chocolate dots are greater than 20 km. Blue rectangles are profiles shown in figures 13a, 13a and 13c.

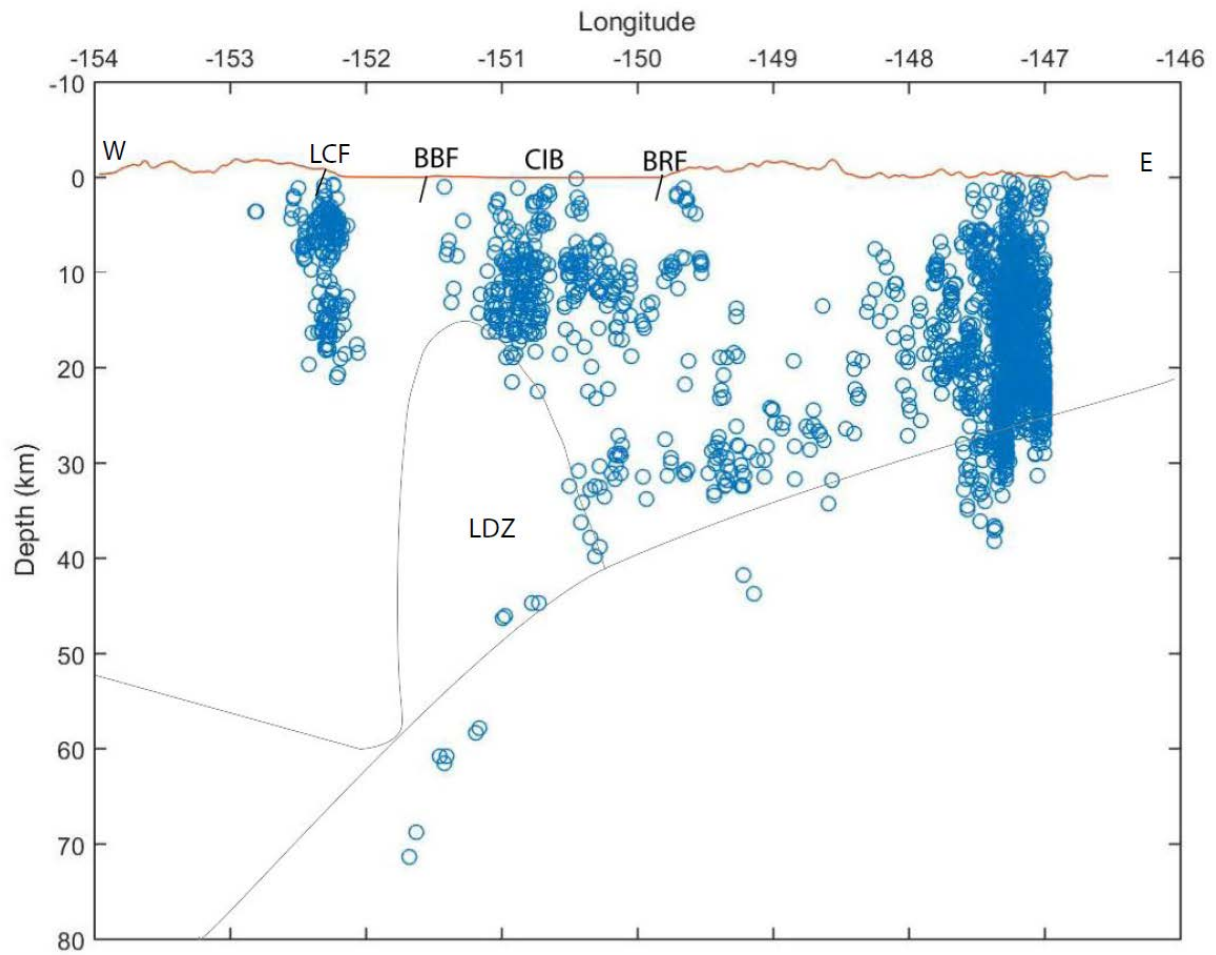


Figure 13a: East west profile showing hypocenter of seismic events with a map zone of LDZ (low density zone) and subducting plate.

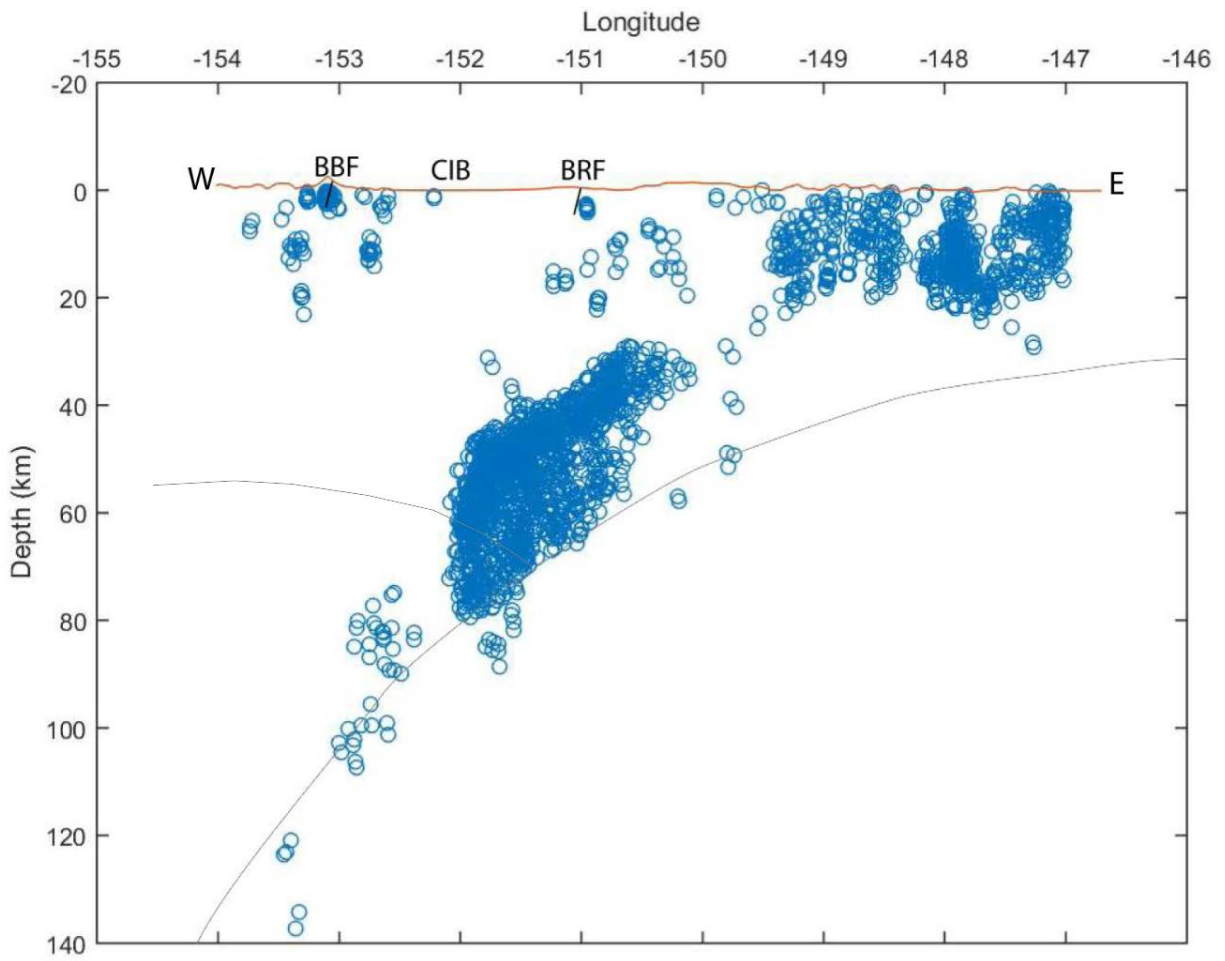


Figure 13b: Profile 2 is a west east vertical profile south along the southern boundary of the low Bouguer anomaly within the basin.



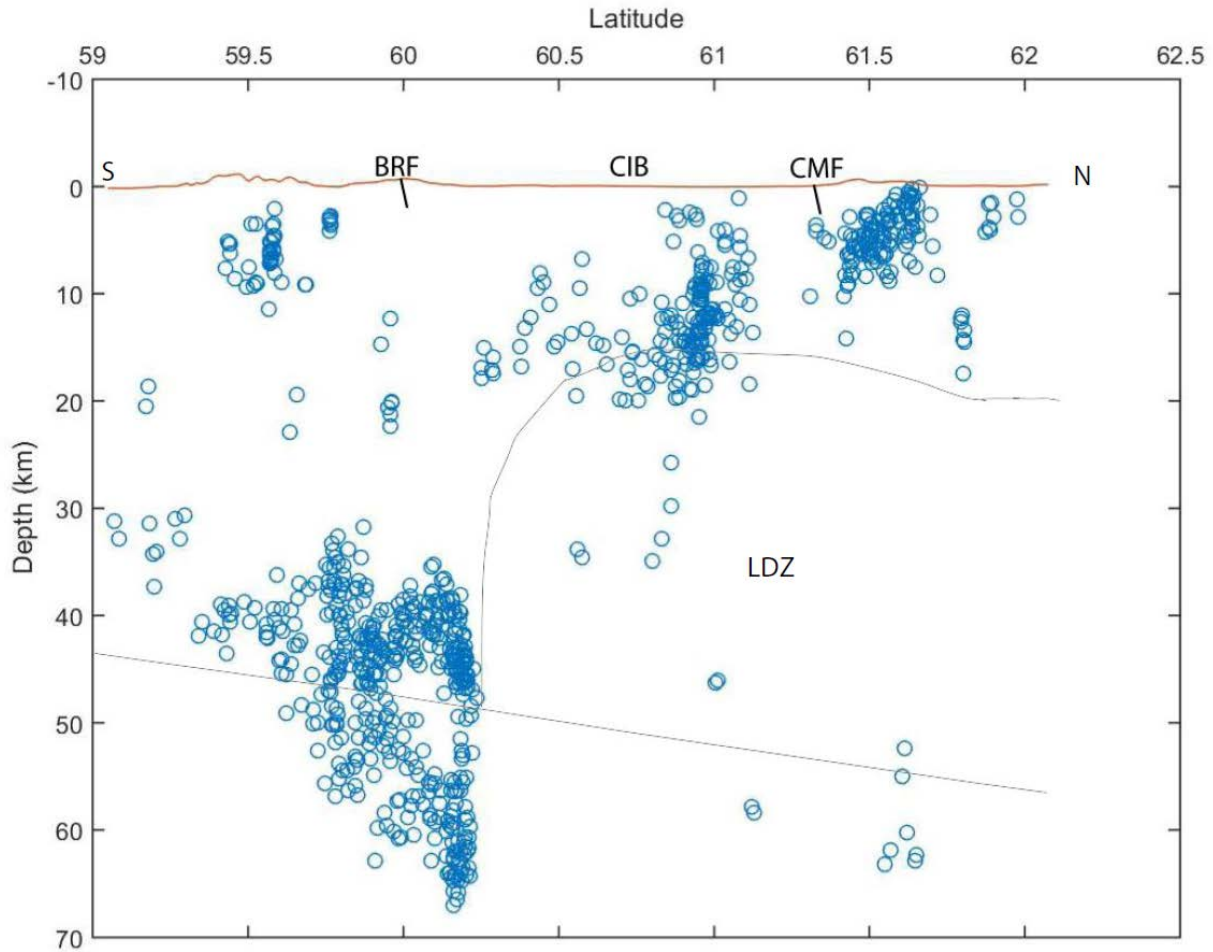


Figure 13c: Profile 3 showing seismic events running north south through CIB. LDZ=Low density zone

Rate of uplift within CIB was estimated using time series GPS data (Figure 14; from 2006 to 2016) downloaded from the University NAVSTAR consortium (UNAVCO) website (<http://data-out.unavco.org/pub/products/>). The rate of uplifts is used to generate contours and superimposed on the Complete Bouguer anomaly map to see if the uplift rate is controlled by low Bouguer anomaly within CIB. From the map the highest rate of uplift is 10 mm/yr located at two positions

(i.e. the northeastern and southernmost sections of the map). Both locations of the highest rate of uplift are associated with intermediate to high Complete Bouguer anomaly (from -40 mGal to 10.2 mGal). The lowest rate of uplift (~1.5 mm/yr) is in the southeast section of the map with very high Complete Bouguer anomalies (~16.3 to ~45 mGal). Along the low Complete Bouguer anomaly within CIB with southwest to northeast orientation, rate of uplift is high (~9.5 mm/yr) at the southeast and reduces towards the northeastern edge (~4.5 mm/yr). The uplift rates are lower compared with Cohen et al. (1997) average uplift rate of 30 mm/yr estimated from a combined GPS measurement (collected in 1993 and 1995) and leveling observations (measured in 1964). Cohen et al. (1997) high uplift rates were interpreted as rapid post seismic uplift from the occurrence of the magnitude 9.2 1964 earthquake. The trend variation in uplift (not magnitude) shown in figure 15 identifies very well with the results of Cohen and Freymueller (2004). A research on cumulative uplift rates within the southern Alaska led to Suito et al. (2003) identifying that the calculated uplift values (e.g. Cohen et al., 1997; Cohen and Freymueller, 2004) were influenced by the choice of viscoelastic model used for the uplift rate. Further research by Suito et al. (2009) identified the estimated uplift rates within Kenai Peninsula by computing postseismic deformation models using a range of mantle viscosities with Maxwell relaxation time of 1 to 50 yrs. Their results indicated that predicted cumulative uplift is less than 40% of the observed uplift. This research does not put much emphasis on the magnitude but the relative extent of uplift across CIB. Therefore, observed uplift will provide a good model to use for analysis. The high rate uplift along the east CMF (northeastern section of the map) corresponds to the zone of high exhumation patterns associated with flat slab subduction (Valentino et al., 2016). CIB is controlled by active northeastern shortening due to compressional stress from the subduction of the Pacific plate and the Yakutat plate. This deformation processes produced series of Pliocene to Quaternary folds

within the basin with an east-northeast trend bounded on north by dextral and reverse slip along Castle Mountain and Bruin Bay faults (Hartman et al., 1974; Cohen and Freymueller, 1997; Haeussler et al., 2000; Parry et al., 2001; Bruhn and Haeussler, 2006; Willis et al., 2007). The folds along the west side of the basin record greater shortening than the eastern folds (Haeussler et al., 2000). Finzel et al., (2015) identified detrital records of spreading-ridge and flat slab subduction processes that discovered sediments deposited in CIB which increases in the southwest of the basin has been transported from the older terranes from the interior Alaska and exhumed eastern. Valentino et al., (2016) conducted rock uplift studies of the Kenai Mountains using apatite (U-Th)/He low temperature thermochronometry. The results indicate low exhumation rates (average rate of ~0.05 mm/yr since 50 Ma) within Kenai mountain compared to the Chugach Mountains. The southwest trend of increment in the uplift rates is likely a contribution of compressional stress and rate of sediment deposition along CIB.

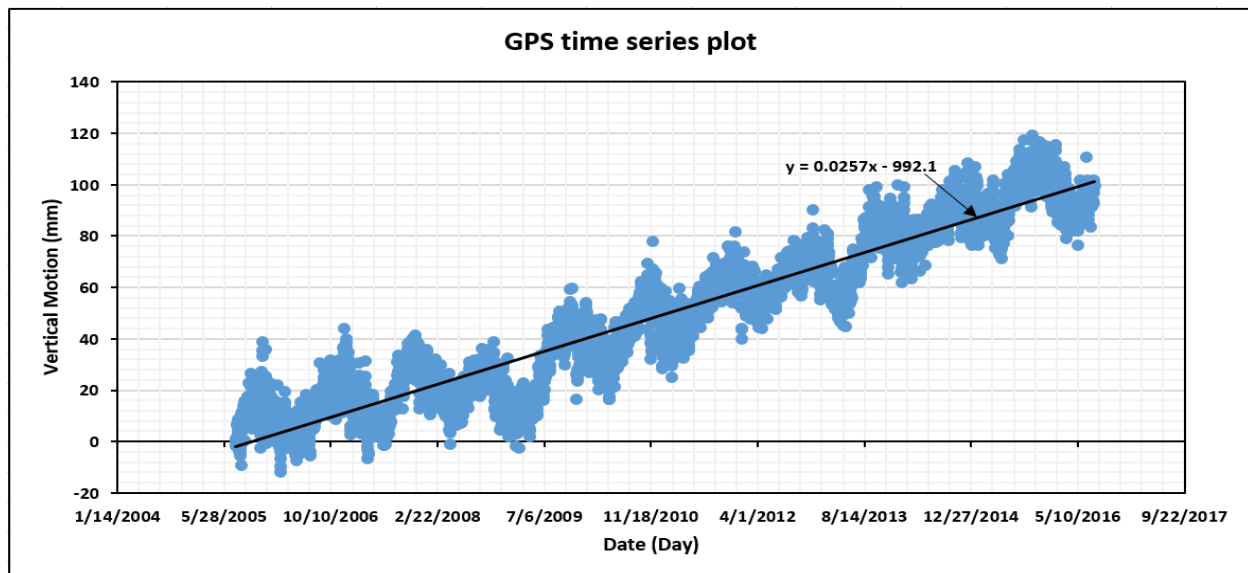


Figure 14: GPS time series plot for data AC11 showing the rate of vertical motion (unit is mm/day).

Location information of this GPS is in Appendix C

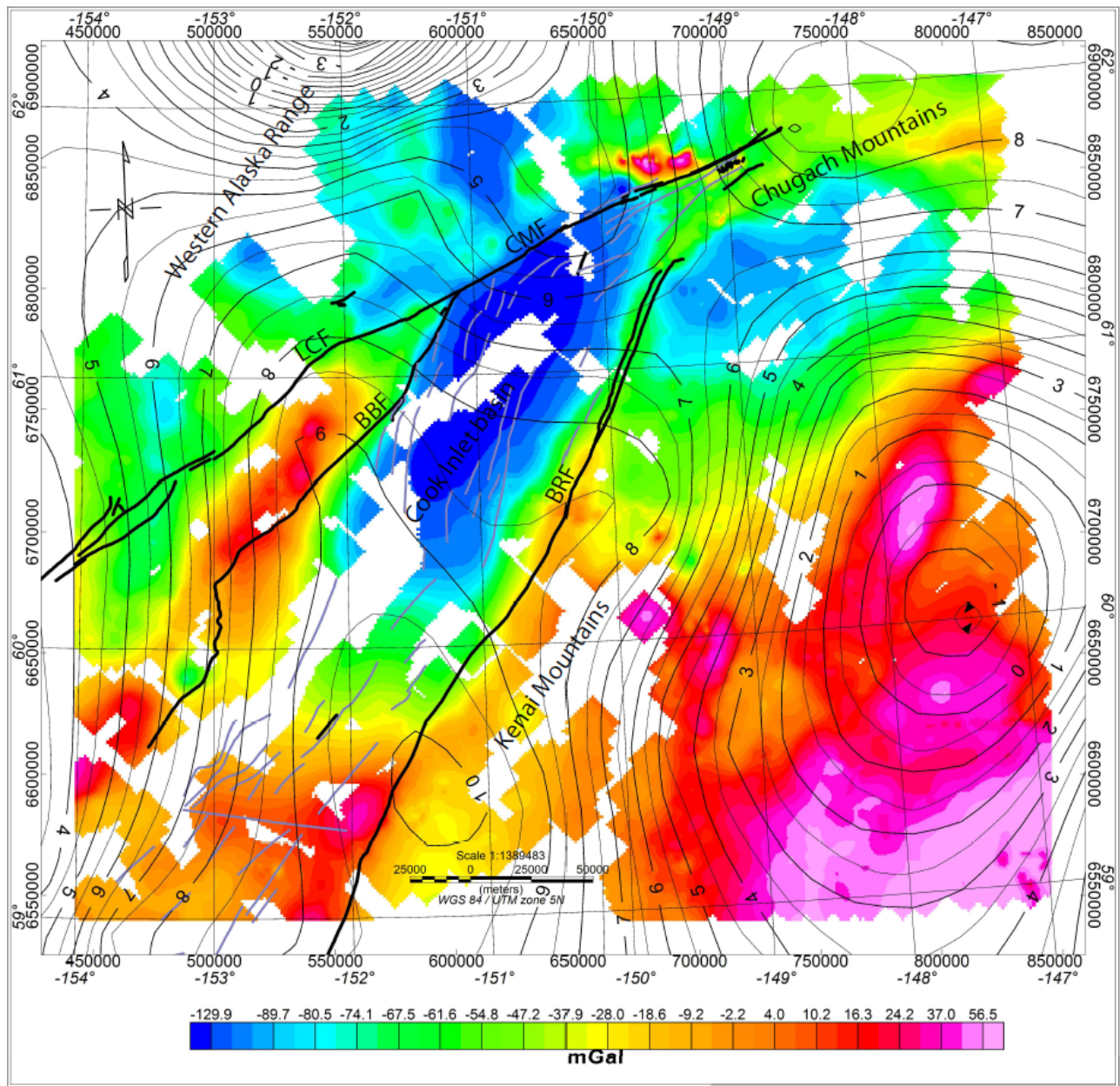


Figure 15: Rate of uplift contours within CIB from time series GPS data superimposed on complete Bouguer gravity anomaly map. Contour values are in the unit of mm/yr.

## 2.5 DISCUSSION

Depth-to-bottom estimates of the long wavelength magnetic sources from 3D inversion and spectral analysis shows a variation across CIB. Maximum depth-to-bottom are estimated within the southern section from the 3D inversion of magnetic data in the basin (~36 to 37 km for block 10 and 16 respectively), the shallowest depth are located in middle of the basin along the zone with low Bouguer anomaly (~15 km east of block 10 and west to block 11 up to block 4) and increased towards the upper or north-northeast section of the basin (between 21 km to 26 km between block 6 and 7). The depth at the southwestern section of the basin are within estimated range of Curie point depth (36.8 to 39.4 km) from temperature-depth profiles except for the northeast section. The difference in the depth to bottom from the southwest to the north-northeast is in the range of 11 to 16 km. This range is comparable to 10 to 20 km estimated as the thickness of the subducting Yakutat plate (e.g. Eberhart-Phillips et al., 2006). I speculate that shallow depth-to-bottom of the long wavelength magnetic source at the north-northeast or upper CIB is due to the upward displacement of the overlying plate during the subduction of the Yakutat microplate. The inversion of the complete Bouguer anomaly data shows the depth-to-top of Bouguer anomaly is ~15 km. The depth-to-bottom of the long wavelength magnetic anomaly along the zone of Bouguer anomaly is <15 km. This puts the source of the long wavelength low gravity anomaly beneath/below the source of high magnetic anomaly. The depth to the low-density anomaly from the complete Bouguer inversion correlates with the modelled depth of the low-velocity density zone (LVDZ) of Mankhemthong et al. (2012) and low velocity observed by Eberhart-Phillips et al. (2016) from a seismic tomography study and supported by a seismic refraction cross-section models generated by Byrne (1986) and Ye et al. (1997). I speculate that the low density zone sits beneath a region of thin crust. The depth-to-bottom of the low Bouguer anomaly zone is not well

constrain from the inversion. Earthquake relocation compared with the Complete Bouguer anomaly inversion shows the presence of an aseismic zone within the region mapped as LDZ in figures 6a and 4a. The earthquake relocated events maps out the subducting Pacific plate which provides an estimate to the bottom extent of the low Bouguer anomaly zone (maximum depth-to-bottom is ~56 km) within CIB. This LDZ is also mapped as a low velocity zone in a Rayleigh wave ambient noise tomography by Ward (2015) within period slices from 10 to 35 seconds corresponding to depth range of 10.5 to 34.5 km. An overlay of isovelocity contour, generated by Eberhart-Phillips et al. (2006) from crust-mantle boundary P-wave velocity of 7.8 km/s, with complete Bouguer anomaly map (Figure 17) shows Moho depth to be ~70 km along the northern boundary of the low-density anomaly region in the CIB. An overlay of Benioff-Wadatti zone (BWZ) contour (blue line) labelled 100 km along the northeastern boundary of low Bouguer anomaly within CIB, shows the depth of the subducting plate (Figure 13). This shows the presence of a thick crust bounding the northeastern edge of the low Bouguer anomaly zone, as modelled by Saltus et al. (2007) and Mankhemthong et al. (2012), sitting on the subducting Pacific plate. The thicker crust and flat subduction of the Pacific plate within this region can produce high coupling along the subducting interface and create the formation of a secondary accretionary zone, beneath CIB, of the underplated sediments on top of the subducting Pacific plate that may have been carried from the ongoing subduction process in south-central Alaska (e.g., Pavlis and Bruhn, 1983; Moore et al., 1991). Infer that the LDZ zone is region containing accumulated sediments. The presence of underplated thick sediments atop the subducting Pacific plate has also been hypothesized by Valentino et al., (2016) as forming a localized seizure of rock uplift within Kenai Mountain based on the slow rate of exhumation measured.



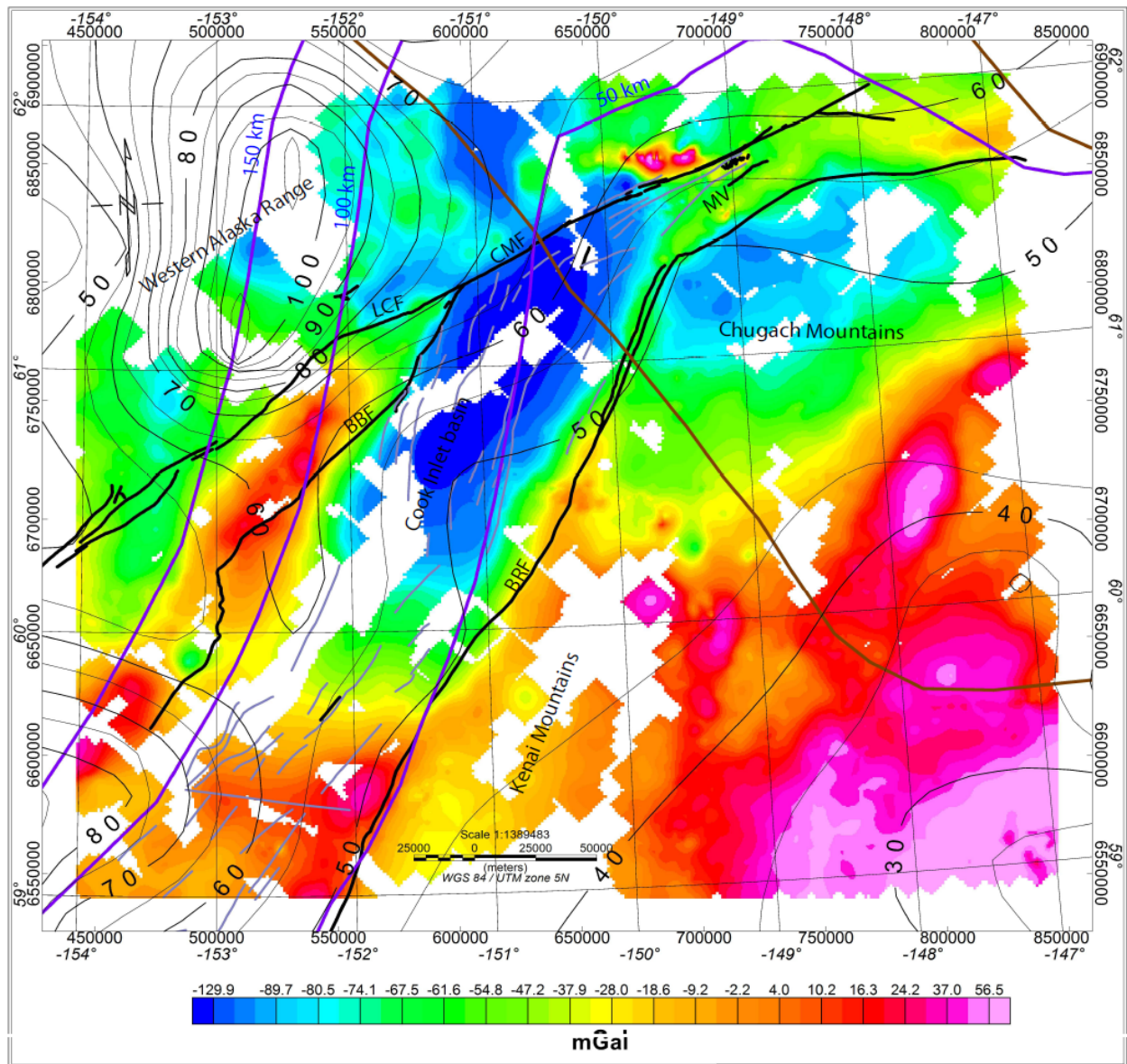


Figure 16: Complete Bouguer map with Isovelocity contours showing estimates of depth (km) to Moho within the southcentral Alaska showing crustal thickness within the basin. Blue lines show depth of the Benioff-Wadatti zone, thick black lines are fault lines and the brown line is the edge of the western edge of the subducting Yakutat microplate.

In contrast the uplift rates from the GPS data shows a trend of increasing relative rate at the eastern margin unto the southern Kenai Mountain. The measured age of rocks (30-50 Ma) by Valentino et al. (2016) compared with the uplift rate of the southern Kenai Mountains, I hypothesize the uplift rate increased later into the subduction of the Yakutat microplate. This can be attributed to the redistribution of the compressional stress associated with the subducting Yakutat microplate to the Kenai Mountains.

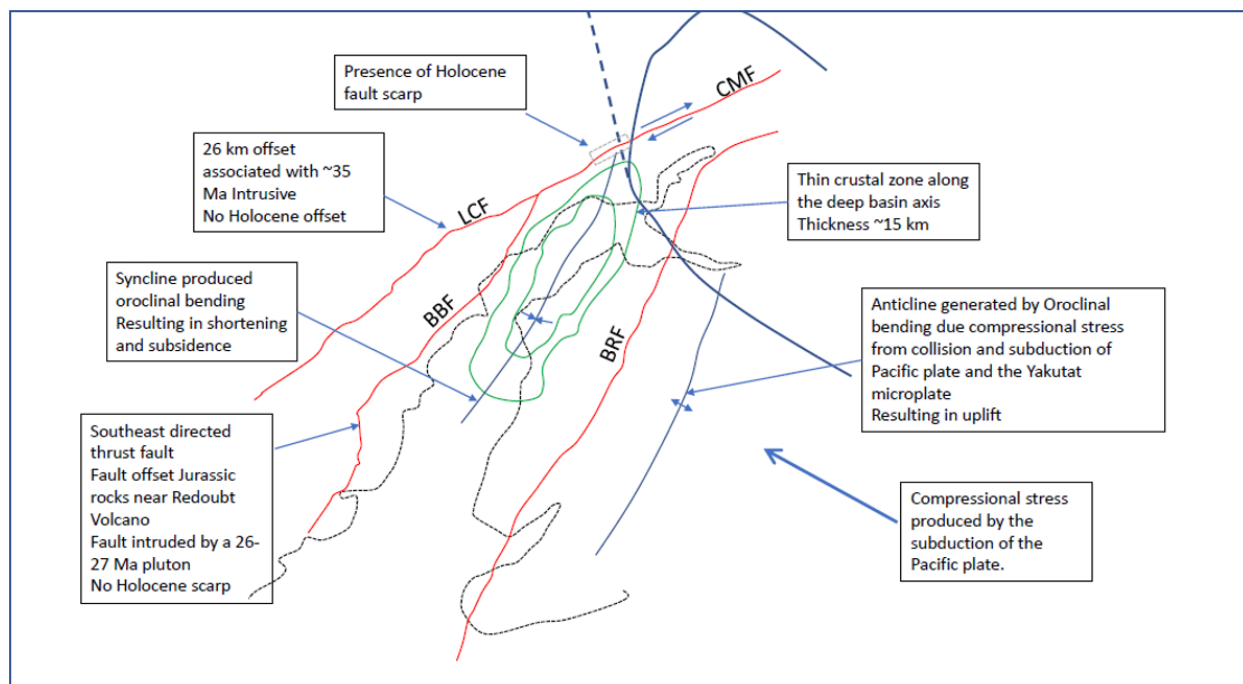


Figure 17a: Cartoon summary of tectonic deformation causing subsidence and shortening of CIB and uplift of Kenai.



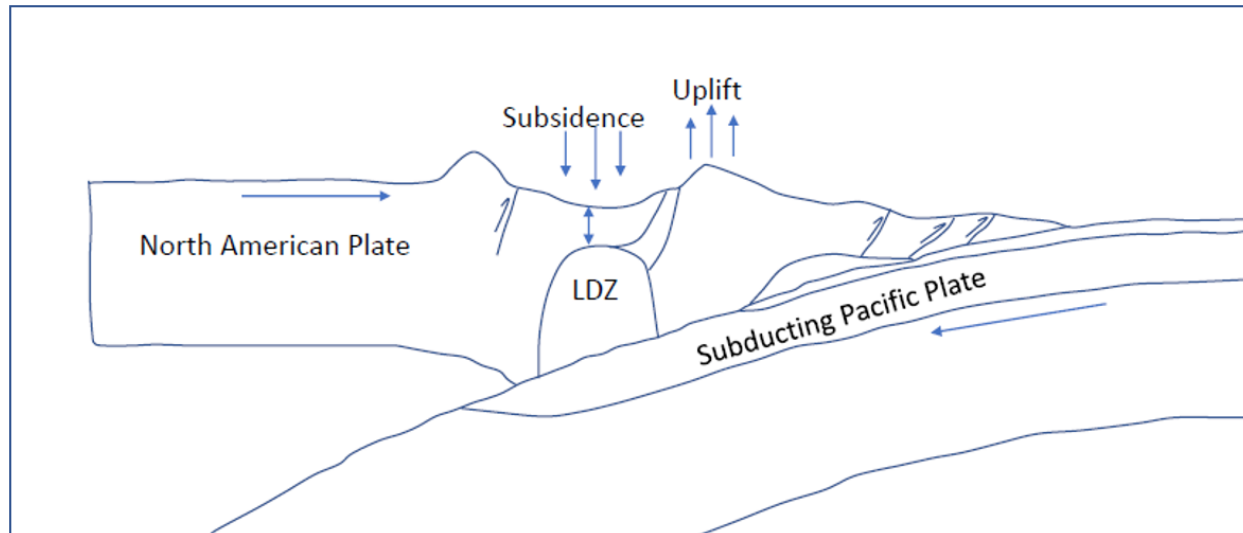


Figure 17b: Cross sectional profile of the subducting Pacific plate and overriding North American Plate with the subsidence and uplift of CIB and Kenai Mountains respectively.

To understand subsidence of CIB and uplift of the Kenai Peninsula, the thin crustal section of CIB mapped from the complete Bouguer anomaly are compared with the tectonic history of southcentral Alaska (Figure 17a). CMF is the only active bounding fault of CIB, a combination of right lateral strike-slip and steeply-dipping north fault system (Detterman et. al., 1974; Haeussler et al., 2002, Bruhn and Haeussler, 2006), with a record of Holocene movement with evidence fault scarp at the western part (Detterman et al., 1974; Haeussler, 1998; Willis et al., 2007) and a history dated back to at least 47 Ma (Parry et al., 2001). Late Neogene and younger deformations resulting in shortening along the northeastern axis of the basin has been attributed to the collision and subduction of the Yakutat microplate and counterclockwise rotation of south-central Alaska (Bruhn and Haeussler, 2006). The north-south axis of the low amplitude anomaly, smallest crustal thickness, lies approximately along the north-south axis and impinges onto the zone expose Holocene scarp along the CMF. From these comparison, I speculate that the subsidence within CIB is controlled by the formation of a syncline along with its axis along the region of thin crust

produced by oroclinal bending with the anticlinal axis running parallel to the eastern boundary of the basin (Figure 17a) producing uplift of the Kenai Mountain. A cross section across the northwest to southeast (Figure 17b) shows the vertical motion produced as a result of oroclinal bending.

## 2.6 CONCLUSION

The application of 3D inversion of magnetic and gravity data reveals the depth of long wavelength magnetic anomalies and gravity anomaly within the crust beneath CIB. The results from magnetic inversion, power spectrum analysis estimate the depth range of the long wavelength magnetic anomaly within CIB. The geometry with estimated depth-to-bottom of the magnetic anomaly shows a huge variation across the basin. Comparing the depth of the magnetic anomaly with estimated Moho depth contours generated from isovelocity maps shows the anomaly is located within the crust. An inversion of the complete Bouguer anomaly data maps the depth of the low amplitude gravity anomaly. The bottom of these anomaly is not well constraint from the inversion. A comparison of the low amplitude gravity anomaly with relocated earthquake data provides an estimate range of the bottom of the of the gravity anomaly from the mapping of the subducting Pacific plate. Comparing the depth-to-top of the low amplitude gravity anomaly with the depth-to-bottom of the long wavelength magnetic anomaly shows the low amplitude gravity anomaly sits beneath a zone with a shallow depth-to-bottom of the magnetic anomaly source. The difference in depth to the location of the magnetic and gravity anomaly sources implies that both anomalies are likely not properties associated with the same rock, casting doubt on the earlier hypothesis that interprets the anomalies as signatures from the same source. The Moho depths superimposed on the Bouguer map within the basin shows thick crust bounding the northwestern edge of the LDZ. This sit along the transition from normal subduction to flat slab subduction. Therefore, we infer the presence of a high interplate coupling that is producing secondary sediment accretion beneath the basin. This supports the presence of thick sediments atop the subducting Pacific plate beneath the basin. The thin crustal thickness along the long axis of the low amplitude compared with

tectonic history and deformation within the vicinity of CIB shows subsidence within the basin is produced by oroclinal bending creating uplift of the Kenai Mountains.

## 2.7 REFERENCES

Abers, G.A., van Keken, P.E., Kneller, E.A., Ferris, A., and Stachnik, J.C., 2006, The thermal structure of subduction zones constrained by seismic imaging: Implications for slab dehydration and wedge flow: *Earth and Planetary Science Letters*: v. 241, p. 387–397, doi: 10.1016/j.epsl.2005.11.055.

Amato, J. M., Pavlis, T. L., Clift, P. D., Kochelek, E. J., Hecker, J. P., Worthman, C. M., Day, E. M., 2013, Architecture of the Chugach accretionary complex as revealed by detrital zircon ages and lithologic variations: Evidence for Mesozoic subduction erosion in south-central Alaska. *Geol. Soc. Am. Bull.* **125**, 1891–1911. doi:10.1130/B30818.1

Batir J.F, Blackwell, D.D and Richards, M.C, 2013 Updated Heat Flow Map of Alaska: New Insights into the Thermal Regime Final Report (Fairbanks, AK: Alaska Center for Energy and Power)

Batir J F, Blackwell D D, Richards M C, 2016, Heatflow and temperature-depth curves throughout Alaska: finding regions for future geothermal exploration, *J Geophys. Eng* 13 366-377

Batir J F, Blackwell D D, Richards M C, 2010, Heat flow and temperature-depth curves throughout Alaska: finding regions for future geothermal exploration; *J Geophys. Eng.* 13 366-377

Bauer, M.A., 2014, Seismic structure of southeastern Alaska [Ph.D. thesis]: Bloomington, Indiana University, 191 p.

Bhattacharyya, B., and Leu, L. (1975), Spectral analysis of gravity and magnetic anomalies due to two dimensional structures, *Geophysics* 40, 993–1013.

Blackwell D D and Richards M C (ed) 2004b *Heat Flow Map of North America* (Tulsa, OK: American Association of Petroleum Geologists)

Blackwell D D, Negraru P T and Richards M C 2007 Assessment of the enhanced geothermal system resource base of the United States *Nat. Resour. Res.* **15** 283–308

Bruhn, R., Haeussler, P., 2006. Deformation driven by subduction and microplate collision: geodynamics of Cook Inlet basin, Alaska. *Geol. Soc. Am. Bull.* 118 (3–4), 289–303.  
<http://dx.doi.org/10.1130/b25672.1>.

Blakely, R.J. (1988), Curie temperature isotherm analysis and tectonic implications of aeromagnetic data from Nevada. *J. Geophys. Res.* vol. 93, no. B10, pp. 11,817–11,832.

Boss R.F., Lennon R.B., Wilson B.W., 1976, Middle Ground Shoal oil field, Alaska, in Braunstein J., ed., *North American Oil and Gas Fields*: American Association of Petroleum Geologists Memoir 24, p. 1–22.

Bouligand, C., Glen, J., and BLAKELY, R. (2009), Mapping Curie temperature depth in the western United States with a fractal model for crustal magnetization, *Journal of Geophysical Research* 114. doi:10.1029/2009JB006494.

Bradley, D., Kusky, T., Haeussler, P., Goldfarb, R., Miller, M., Dumoulin, J., Nelson, S.W., Karl, S., 2003. Geologic signature of early Tertiary ridge subduction in Alaska. In: Sisson, V.B., Roeske, S.M., Pavlis, T.L. (Eds.), *Orogen Developed During Ridge–Trench Interaction Along the North Pacific Margin*, GSA Special Paper. *Geology of a Transpressional*, vol. 371, pp. 19–50.

Brandon, M. T., and Vance, J. A., 1992, Tectonic evolution of the Cenozoic Olympic subduction complex, Washington States, as deduced from fission track ages for detrital zircons: *American Journal of Science*, v. 292, p. 565–636.

Bruhn, R.L., Parry, W.T., and Bunds, M.P., 2000, Tectonics, fluid migration, and fluid pressure in a deformed forearc basin, Cook Inlet, Alaska; Geological Society of America Bulletin, v. 112, p.550-563.

Bruhn, R., Haeussler, P., 2006. Deformation driven by subduction and microplate collision: geodynamics of Cook Inlet basin, Alaska. Geol. Soc. Am. Bull. 118 (3–4), 289–303.

<http://dx.doi.org/10.1130/b25672.1>.

Byerly, P. E., and Stolt, R. H. (1977), An attempt to define the Curie point isotherm in Northern and Central Arizona, Geophysics 42, 1394–1400.

Calderwood, K.W., and Fackler, W.C., 1972, Proposed stratigraphic nomenclature for Kenai Group, Cook Inlet Basin, Alaska: American Association of Petroleum Geologists Bulletin, v. 56, p. 739-754.

Carslaw H S and Jaeger J C 1959 *Conduction of Heat in Solids* (Oxford: Oxford University Press)

Chai, Y., and Hinze, W. J., 1988, Gravity inversion of an interface above which the density contrast varies exponentially with depth: Geophysics, 53, 837–845

Chapman, DS, Furlong, KP., 1992. Thermal state of continental lower crust. In: Fountain, D.M., Arculus, R., Kay, R.W. (Eds.), Continental Lower Crust. Elsevier Science, Amsterdam, pp. 179-199.

Clardy, B.I., 1974, Origin of the lower and middle Tertiary Wishbone and Tsdaka Formations, Matanuska Valley, Alaska [M.S. thesis]: Fairbanks, University of Alaska, 74 p.

Clift, P.D., Pavlis, T., DeBari, S.M., Draut, A.E., Rioux, M., Kelemen, P.K., 2005, Subduction erosion of the Jurassic Talkeetna-Bonanza arc and the Mesozoic accretionary tectonics of western North America: Geology, v.33, p.881-884.

Clift, P. D., Carter, A., Giosan, L., Durcan, J., Duller, G. A., Macklin, M. G., ... & Fuller, D. Q. (2012). U-Pb zircon dating evidence for a Pleistocene Sarasvati River and capture of the Yamuna River. *Geology*, 40(3), 211-214.

Cohen, S.C., Freymueller, J.T. 1997. Deformation of the Kenai Peninsula, Alaska. *J.Geophys. Res.* 102 (B9), 20479-20487. <http://dx.doi.org/10.1029/97JB01513>

Cohen, S. C., and J. T. Freymueller (2004), Crustal deformation in the southcentral Alaska subduction zone, *Adv. Geophys.*, 47, 1 – 58.

Denig-Chakroff D, Reeder J W and Economides M J 1985 Development potential of the Makushin geothermal reservoir of Unalaska Island, Alaska *Geotherm. Resour. Counc. Trans.* 9 177–182

Doser, D. I. (2004), Seismicity of the Denali–Totschunda fault zone in central Alaska (1912–1988) and its relation to the 2002 Denali fault earthquake sequence, *Bull. Seismol. Soc. Am.*, 94, 132–144.

Doser, D. I., and A. M. Veilleux (2009), A comprehensive study of the seismicity of the Kenai Peninsula-Cook Inlet Region, South-Central Alaska, *Bull. Seismol. Soc. Am.*, 99(4), 2208–2222, doi:10.1785/0120080251

Eberhart-Phillips D, Christensen D H, Brocher T M, Hansen R, Ruppert N A, Haeussler P J and Abers G A 2006 Imaging the transition from Aleutian subduction to Yakutat collision in central Alaska, with local earthquakes and active source data *J. Geophys. Res.* **111** B11303

Erkan K, Holdmann G, Benoit W and Blackwell D D, 2008, Understanding the Chena Hot Springs, Alaska, geothermal system using temperature and pressure data from exploration boreholes *Geothermics* **37** 565–85



- Espinosa-Cardena, J.M., and Campos Enriquez, J.O., 2008, Curie point depth from spectral analysis of aeromagnetic data from Cerro Prieto geothermal area, Baja California, México: *Journal of Volcanology and Geothermal Research* 176(4):601-609
- Finzel, E. S., L. M. Flesch, and K. D. Ridgway (2011). Kinematics of a diffuse North America–Pacific–Bering plate boundary in Alaska and western Canada, *Geology* 39, no. 9, 835–838.
- Fisher, M.A., and Magoon, L.B., 1978, Geologic framework of lower Cook Inlet, Alaska: *AAPG Bulletin*, v.62, p.373-402.
- Finzel, E. S., K. D. Ridgway, and J. M. Trop (2015), Provenance signature of changing plate boundary conditions along a convergent margin: Detrital record of spreading-ridge and flat-slab subduction processes, Cenozoic forearc basins, Alaska, *Geosphere*, 11(3), 1–27, doi:10.1130/GES01029.1.
- Fliedner, M.M, and Klemperer, S.L, 1999, Structure of an island arc: Wide-angle seismic studies in the eastern Aleutian Islands, Alaska, *J. Geophys. Res.* 104, 10667-10694
- Flores, C., and Doser, D.I., 2005, Shallow seismicity of the Anchorage, Alaska, region (1964–1999): *Bulletin of the Seismological Society of America*, v. 95, no. 5, p. 1865–1879, doi: 10.1785 /0120040121.
- Flores, R.M., and Stricker, G.D., 1993, Interfluve-channel facies models in the Miocene Beluga Formation near Homer, south Kenai Peninsula, Alaska, in, Rao, P.D., and Walsh, D.E., eds., *Focus on Alaska's coal 1993: Mineral Industry Research Laboratory, University of Alaska, Fairbanks*, p.140-166.
- Flores R.M., Stricker G.D., Roberts S.B., 1994, Miocene coal-bearing strata of the Tyonek Formation: Braided-stream deposits in the Chuit Creek–Chuitna River drainage basin, Southern

Alaska, in Till A.B., Moore T.E., eds., *Geologic studies in Alaska by the U.S. Geological Survey, 1993: U.S. Geological Survey Bulletin 2107*, p.95–114.

Flores R.M., Stricker G.D., Bader L.R., 1997, Stratigraphic architecture of the Tertiary alluvial Beluga and Sterling Formations, Kenai Peninsula, Alaska in Karl S.M., Vaughn N.R., Ryherd T.J., eds., *1997 Guide to the Geology of the Kenai Peninsula, Alaska*: Anchorage, Alaska, Alaska Geological Society, p.36–53.

Flores, R.M., et al., 1999, National coal resource assessment non-proprietary data; location, stratigraphy, and coal quality of selected Tertiary coal in the Northern Rocky Mountains and Great Plains region: U.S. Geological Survey Open-File Report No.OF 99-00376, 12p.

Freymueller, J. T., Woodard, H., Cohen, S. C., Cross, R., Elliott, J., Larsen, C. F., Hreinsdóttir, S., and Zweck, R., 2008, Active Deformation Processes in Alaska, Based on 15 Years of GPS Measurements, Active Tectonics and Seismic Potential of Alaska Geophysical Monograph Series 179 Copyright 2008 by the American Geophysical Union. 10.1029/179GM02

Frost, B.R., and Shive, P.N. (1986), Magnetic mineralogy of the lower continental crust. *J. Geophys. Res.* 91, 6513–6521.

Gesch, D., M. Oimoen, S. Greenlee, C. Nelson, M. Steuck, and D. Tyler (2002), The National Elevation Dataset, *Photogramm.Eng. Remote Sens.*, 68

Gedney, Larry, 1985, Stress Trajectories across the Northeast Alaska range, *Bulletin of the Seismological Society of America*, Vol. 75, No.4. pp. 1125-1134.

Gesch, D.B., 2007. The National Elevation Dataset. In: Maune, D., ed., *Digital Elevation Model Technologies and Applications: The DEM User's Manual*, 2nd Edition. American Society for Photogrammetry and Remote Sensing, Bethesda, Maryland, pp. 99-118.

Gough, D. I., and J. S. Bell, Stress orientations from oil well fractures in Alberta and Texas, Can. J. Earth Sci., 18, 638-645, 1981.

Green, W. R., 1975, Inversion of gravity profiles by use of a BackusGilbert approach: Geophysics, 40, 763–772.

Guspi, F., 1992, Three-dimensional Fourier gravity inversion with arbitrary density contrast: Geophysics, 57, 131–135.

Gutscher, M. A., and S. M. Peacock (2003), Thermal models of flat subduction and the rupture zone of great subduction earthquakes, J. Geophys. Res., 108(B1), 2009.

Gutscher, M.A., Spakman, W., Bijwaard, H., Engdahl, E.R., 2000. Geodynamics of subduction: seismicity and tomographic constraints from the Andean margin. Tectonics 19, 814–833.

Haeussler P.J, Bruhn R. L., Pratt T. L.; 2000; Potential seismic hazards and tectonics of the upper Cook Inlet basin, Alaska, based on analysis of Pliocene and younger deformation; GSA bulletin; v. 112; no. 9; p. 1414–1429;

Haeussler, P., Bradley, D., Wells, R., Miller, M., 2003. Life and death of the Resurrection plate: evidence for its existence and subduction in the northeastern Pacific in Paleocene–Eocene time. Geol. Soc. Am. Bull. 115 (7), 867–880. [http://dx.doi.org/10.1130/00167606\(2003\)115<0867:lado>2.0.co;2](http://dx.doi.org/10.1130/00167606(2003)115<0867:lado>2.0.co;2).

Haeussler, P.J., 2008, An overview of the neotectonics of interior Alaska—Far-Field Deformation from the Yakutat Microplate Collision: American Geophysical Union Monograph 179, p. 83–108, doi: 10.1029/179GM05'

Haeussler, P.J., O'Sullivan, P., Berger, A.L., Spotila, J.A., 2008. Neogene exhumation of the Tordillo Mountains, Alaska, and correlations with Denali (Mount McKinley). In: Freymueller,

J.T., Haeussler, P.J., Wesson, R.J., Ekstrom, G. (Eds.), Active Tectonics and Seismic Potential of Alaska: Geophysical Monograph Series, 179, pp. 269–285.

Haeussler, P.J., and Saltus, R. W., 2011, Location and extent of Tertiary structures in Cook Inlet Basin, Alaska, and mantle dynamics that focus deformation and subsidence, in Dumoulin, J. A., and Galloway, J.P., eds., Studies by the U.S. Geological Survey in Alaska 2008-2009: U.S. Geological Survey Professional Paper 1776-D. p. 26.

Haggerty, S.E. (1978), Mineralogical constraints on Curie isotherm in deep crustal magnetic anomalies. *Geophys. Res. Lett.* 5(2), pp. 105–109. S.M. Peacock, R.D. Hyndman, Hydrous minerals in the mantle wedge and the maximum depth of subduction thrust earthquakes, *Geophys. Res. Lett.* 26 (1999) 2517-2520.

Handi, Lu, 2003, Deformation pattern of convergent margin within accretionary prism, Aleutian arc-trench: 2D finite element modeling, *Japanese journal of structural geology* (47), 23-36

Hartman, D.C., Pessel, G.H., McGee, D.L., 1974. Stratigraphy of the Kenai Group, Cook Inlet. Alaska Division of Geological and Geophysical Surveys. Alaska Open File Report 49.

He, R, Liu, G, Golos, E, Gao, R, Zheng, H, 2014, Isostatic gravity anomaly, lithospheric scale density structure of the northern Tibetan plateau and geodynamic causes for potassic lava eruption in Neogene, *Tectonophysics* 628, 218-227.

Hong, M. R. (1982), The inversion of magnetic and gravity anomalies and the depth to Curie isotherm, Ph.D. Thesis (University of Texas at Dallas, Richardson, Tx. USA).

Hussein, M., Mickus, K., and Serpa, L. (2012), Curie point depth estimates from aeromagnetic data from Death Valley and surrounding regions, California. *Pure and Applied Geophysics* 170, 617–632.

Hyndman, R.D., and S.M. Peacock, 2003, Serpentinization of the forearc mantle, *Earth Planet. Sci. Lett.*, 212(3-4), 417-432, doi:10.1016/S0012-821X (03)00263-2.

Kirschner, C.E., Lyon, C.A., 1973. Stratigraphic and Tectonic Development of Cook Inlet Petroleum Province. *Regional Arctic Geology of Alaska*, pp. 396–407.

Kissling, E., and J. C. Lahr, 1991, Tomographic image of the Pacific slab under southern Alaska, *Eclogae Geol. Helv.*, 84, 297-315

Kolker A M 2007 *Alaska Geothermal Development: a Plan* (Anchorage, AK: Alaska Energy Authority)

Kolker A.M, Stelling P, Cumming W and Rohrs D, 2012, Exploration of the Akutan geothermal resource area 37th Workshop on Geothermal Reservoir Engineering (Stanford University) SGP-TR-194

Lachenbruch A H 1970 Crustal temperatures and heat production: implications of the linear heat-flow relation *J. Geophys. Res.* [75 3291–300](#)

Lachenbruch A H, Sass J H, Marshall B V and Moses T H Jr 1982 Permafrost, heat flow, and the geothermal regime of Prudhoe Bay, Alaska *J. Geophys. Res.* [87 9301–16](#)

Last, B. J., and Kubik, K, 1983, Compact gravity inversion: *Geophysics*, 48, 713–721

LePain, D.L., Stanley, R.G., Helmold, K.P., and Shellenbaum, D.P., 2013, Geologic framework and petroleum systems of Cook Inlet basin, south-central, Alaska, *in* Stone, D.M., and Hite, D.M., eds., *Oil and Gas Fields of the Cook Inlet Basin, Alaska: American Association of Petroleum Geologists Memoir 104*, p. 37–116.

Li, Y., and Oldenburg D.W. (1996), 3D inversion of magnetic data, *Geophysics* 61, 394–408.

MacKevett, E.M., Jr., and Plafker, G., 1974, The Border Ranges fault in south-central Alaska: *US, Geological Survey Journal of Research*, v. 2, p. 323-329.

Magoon, L. B., 1994, Petroleum resources in Alaska, in Plafker, B., and Berg, H.C., eds The geology of Alaska: Boulder, Colorado, Geological Society of America, Geology of North America v G-1, p. 905-936.

Manea, M, and Manea V.C., 2010, Curie Point Depth Estimates and Correlation with Subduction in Mexico, Pure and Applied Geophysics, DOI 10.1007/s100024-010-0238-2.

Manea, M., and Manea, V. (2011), Curie point depth estimates and correlation with subduction in Mexico, Pure and Applied Geophysics 168, 1489–1499.

Mankhemthong, N., Doser, D.I., and Pavlis, T.L., 2013, Interpretations of gravity and magnetic data and development of 2.5D cross sectional models for the Border Ranges fault system, south-central Alaska, Geosphere, v. 9, p. 242-259, doi:10.1130/GES00833.1.

Mickus, K. (1989), Backus and Gilbert inversion of two and one-half dimensional gravity and magnetic anomalies and crustal structure studies in western Arizona and the eastern Mojave Desert, California, Ph.D. Thesis (University of Texas at El Paso, El Paso, TX, USA).

Mickus, K., Hussein, M., 2015, Curie Depth Analysis of the Salton Sea Region, Southern California, Pure Appl. Geophys. 173 (2016), 537–554, DOI 10.1007/s00024-015-1100-3

Motyka, R.J, Moorman M.A and Liss S.A, 1983, Geothermal Resources of Alaska: Miscellaneous Publication MP 8 (Fairbanks, AK: State of Alaska, Department of Natural Resources, Division of Geological & Geophysical Surveys)

Nettleton L.L., 1939, Determination of density for reduction of gravimeter observations, Geophysical Journal of the Royal Astronomical Society, 57, 137-157.

Oldenburg, D. W., 1974, The inversion and interpretation of gravity anomalies: Geophysics, 39, 394–408

Okubo, Y., Graf, R., Hansen, R., Ogawa, K., and Tsu, H. (1985), Curie depths of the island of Kyushu and surrounding areas, Japan, *Geophysics* 53, 481–494.

Page, R. A., N. N. Biswas, J. C. Lahr, and H. Pulpan (1991), Seismicity of continental Alaska, in *Neotectonics of North America, Decade Map, I*, edited by D. B. Slemmons et al., pp. 47–68, Geol. Soc. of Am., Boulder, Colorado.

Paranis, D.S., 1952, A study of rock densities in English Midlands: *Geophysical Journal International*, 6, 252-271.

Parry, W.T., Bunds, M.P., Bruhn, R.L., Hall, C.M., Murphy, J.M., 2001. Mineralogy,  $^{40}\text{Ar}/^{39}\text{Ar}$  dating and apatite fission track dating of rocks along the Castle Mountain fault, Alaska. *Tectonophysics* 337 (3–4), 149–172. [http://dx.doi.org/10.1016/S0040-1951\(01\)00117-2](http://dx.doi.org/10.1016/S0040-1951(01)00117-2).

Pavlis, T.L., Bruhn, R.L., 1983. Deep-seated flow as a mechanism for the uplift of broad forearc ridges and its role in the exposure of high P/T metamorphic terranes. *Tectonics* 2 (5), 473–497. <http://dx.doi.org/10.1029/TC002i005p00473>.

Pavlis, T.L., Picornell, C., Serpa, L., Bruhn, R.L., Plafker, G., 2004. Tectonic processes during oblique convergence: insights from the St. Elias Orogen, northern North American Cordillera. *Tectonics* 23. [doi:10.1029/2003TC001557](https://doi.org/10.1029/2003TC001557).

Pavlis, T.L., and Roeske, S.M., 2007, The Border Ranges fault system, southern Alaska, in Ridgeway, K.D., Trop, J.M., Glen, J.M.G., and O'Neill, J.M., eds., *Tectonic growth of a Collisional continental margin: Crustal evolution of southern Alaska*: Geological Society of America Special paper 431, p.95-128.

Pedersen, L. B., 1977, Interpretation of potential field data: A generalized inverse approach: *Geophys. Prosp.*, 25, 199–230. 1979, Constrained inversion of potential field data: *Geophys. Prosp.*, 27, 726–748

Peterson S 2013 Preliminary geothermal gradient mapping in Alaska's Cook Inlet forearc basin  
Geotherm. Resour. Counc. Trans. 37 315–20

Plafker, G., W. J. Nokleberg, and J. S. Lull, 1989, Bedrock geology and tectonic evolution of the Wrangellia, Peninsular, and Chugach Terranes along the Trans-Alaska Crustal Transect in the Chugach Mountains and Southern Copper River Basin, Alaska, *J. Geophys. Res.*, 94, 4255–4295.

Plafker, George, Moore, J.C., and Winkler, G.R., 1994, Geology of the southern Alaska margin, in Plafker, George, and Berg, H.C., eds., *The geology of Alaska*: Boulder, Colo., Geological Society of America, *The Geology of North America*, v. G-1, p.389–449.

Ratchkovski, N. A. (2003). Change in stress directions along the central Denali fault, Alaska after the 2002 earthquake sequence, *Geophys. Res. Lett.* 30, 2017, doi 10.1029/2003GL017905.

Ratchkovski, N. A., and R. A. Hansen (2002a). New constraints on tectonics of interior Alaska: Earthquake locations, source mechanisms and stress regime, *Bull. Seism. Soc. Am.* 92, 998–1014.

Ratchkovski, N., Wiemer, S. & Hansen, R., 2004. Seismotectonics of the central Denali Fault, Alaska and the 2002 Denali Fault earthquake sequence, *Bull. seism. Soc. Am.*, 64, 156–174.

Ravat, D., Pignatelli, A., Nicolosi, I., and Chiappini, M. (2007), A study of spectral methods of estimating the depth to the bottom of magnetic sources from near-surface magnetic anomaly data, *Geophysical Journal International* 169, 421–434.

Reamer, S. K., and Ferguson, J. F., 1989, Regularized two-dimensional Fourier gravity inversion method with application to the Silent Canyon Caldera, Nevada: *Geophysics*, 54, 486–496

Sass, J.H., Lawver, L.A and Munroe R.J, 1985, A heat-flow reconnaissance of southeastern Alaska *Can. J. Earth Sci.* 22 416–21



- Ross, H.E., Blakely, R.J., and Zoback, M.D. (2006), Testing the use of aeromagnetic data for the determination of Curie depth in California. *Geophysics*, vol. 71, no. 5, L51–L59, doi:10.1190/1.2335572.
- Ruppert, N. A., 2008, Stress Map for Alaska From Earthquake Focal Mechanisms, Active Tectonics and Seismic Potential of Alaska Geophysical Monograph Series 179: American Geophysical Union. 10.1029/179GM20.
- Saltus, R.W., Haeussler, P.J., Bracken, R.E., Doucette, J.P., and Jachens, R.C., 2001, Anchorage Urban Region Aeromagnetics (AURA) Project—Preliminary Geophysical results: U.S. Geological Survey Open-File Report 01-0085, 21 p.
- Saltus, R.W., Hudson, T.L., Wilson F.H., 2007, The geophysical character of southern Alaska—Implications for crustal evolution, Geological Society of America, doi: 10.1130/2007.2431(01) *GSA Special Papers* 2007, v. 431, p. 1-20
- Saltus, R. W., Stanley, R. G., Haeussler, P. J., Jones III, J.V., Potter, C. J., Lewis, K. A., Late Oligocene to present contractional structure in and around the Susitna basin, Alaska-Geophysical evidence and geological implications: *Geosphere*, v. 12, no. 5, . 1378-1390, doi:10.1130/GES013279.1.
- Sano, Y., and Wakita, H. (1985), Geographical distribution of  $3\text{He}/4\text{He}$  ratios in Japan: Implications for arc Tectonics and Vol. 173, (2016) Curie Depth Analysis of the Salton Sea Region, Southern California 553 incipient magmatism, *Journal of Geophysical Research* 90, 8729–8741.
- Schinagel S. M., 2015, A geophysical study of the Castle Mountain fault system and Matanuska-Susitna valley near Anchorage, Alaska, Masters Thesis (University of Texas El Paso)

Saltus, R. W., Stanley, R. G., Haeussler, P.J., Jones, J.V., III, Potter, C.J., and Lewis, K.A., 2016, Late Oligocene to present contractional structure in and around the Susitna basin, Alaska- Geophysical evidence and geological implications: *Geosphere*, v.12, no.5, p.1378-1390, doi:1130/GES01279.1.

Schlenger, C.M., 1985, Magnetization of lower crust and interpretation of regional magnetic anomalies: Example from Lofoten and Vesteralen, Norway, *Journal of Geophysical research, solid Earth*, DOI: 10.1029/JB090iB13p11484-11,504.

Shuey, R., Schellinger, D., Tripp, A., and Alley, L. (1977), Curie depth determination from aeromagnetic spectra, *Geophysical Journal of the Royal Astronomical Society* 50, 75–101.

Silwal V and Carl Tape, 2018, Crustal earthquakes in the Cook Inlet and Susitna region of southern Alaska, Elsevier, *Tectonophysics*, <https://doi.org/10.1016/j.tecto.2018.08.013> .

Simpson, R.W., Jachens, R.C., Blakely, R.J., 1986. A new Isostatic residual gravity map of the conterminous United States with a discussion on the significance of Isostatic residual anomalies. *J. Geophys. Res.* 91, 8348–8372.

Spector, A., and Grant, F. (1970), Statistical models for interpreting aeromagnetic data, *Geophysics* 35, 293–302.

Stanley, R.G., Haeussler, P.J., Benowitz, J.A., Goodman, D.K., Ravn, R.L., Shellenbaum, D.P., Saltus, R.W., Lewis, K.A., and Potter, C.J., 2013, New stratigraphic revelations in the subsurface Susitna basin, south-central Alaska, from geochronology and biostratigraphy [poster]: Fresno, California, Geological Society of America Cordilleran Section Meeting, May 22, 2013: Alaska Division of Geological & Geophysical Surveys, 1 sheet. doi: 10.14509/26887 (<http://dggs.alaska.gov/pubs/id/26887>) .

Stutz G R, Williams M, Frone Z F, Reber T J, Blackwell D D, Jordan T and Tester J W 2012 A well by well method for estimating surface heat flow for regional geothermal resource assessment *37th Workshop on Geothermal Reservoir Engineering (Stanford University)* SGPTR-194

Suito, H., J. T. Freymueller, and S. C. Cohen (2003), 3-D Viscoelastic FEM modeling of postseismic deformation caused by the 1964 Alaska Earthquake, southern Alaska, 2003 IUGG General Assembly, JSG01/08P/D-014

Suito, H., Freymueller, J.T., 2009. A viscoelastic and afterslip postseismic deformation model for the 1964 Alaska earthquake. *J. Geophys. Res.* 114, B11404. <http://dx.doi.org/10.1029/2008JB005954>

Swanberg, C., and Morgan, P. (1978), The linear relation between temperatures based on silica content of groundwater and regional heat flow: A new heat flow map of the United States, *Pure and Applied Geophysics* 117, 227–241.

Swenson, R.F., 1997, Introduction to Tertiary tectonics and sedimentation in the Cook Inlet Basin, in Karl, S.M., Vaughn, N.R., and Rhyerdt, T.J., eds., 1997 guide to the geology of the Kenai Peninsula, Alaska: Geological Society of Alaska, Anchorage, p. 18-27.

Syracuse, E. M., van Keken, P. E., Abers, G. A., 2010, The global range of subduction zone thermal models, *Physics of the Earth and Planetary Interiors*, 183 73-90, doi:10.1016/j.pepi.2010.02.004

Tanaka, A., Okubo, Y., and Matsubayashi, O. (1999), Curie point depth based on spectrum analysis of the magnetic anomaly data in East and Southeast Asia. *Tectonophysics* 306, 461–470.

Tarantola, A., and Valette, B., 1982, Generalized non-linear inverse problems solved using least squares criterion: *Review of Geophysics and Space Physics*, 20, 219-232.

- Toft, P.B., Arkani-Hamid, J., Haggerty, S.E., 1990, The effects of serpentization on density and magnetic susceptibility: a petrophysical model: *Physics of the Earth and Planetary Interiors*, v.65, p.137-157.
- Trop, J.M., and Ridgway, K.D., 1999, Sedimentology and provenance of the Paleocene-Eocene Arkose Ridge Formation, Cook Inlet-Matanuska Valley forearc basin, southern Alaska: Short notes on Alaskan geology, Alaska Division of Geological and Geophysical Surveys: Professional Report, v. 119, p. 129–144
- Trop, J.M., and Ridgway, K.D., 2000, Sedimentology and provenance of the Paleocene–Eocene Arkose Ridge Formation, Cook Inlet–Matanuska Valley forearc basin, southern Alaska, *in* Pinney, D.S., and Davis, P.K., eds., Short Notes on Alaskan Geology 1999: Alaska Division of Geological and Geophysical Surveys Professional Report 119J, p. 129–144.
- Trop, J.M., Szuch, D.A., Rioux, M., Blodger, R.B., 2005, Sedimentology and provenance of the Upper Jurassic Naknek Formation, Talkeetna Mountains, Alaska; bearings of the accretionary tectonic history of the Wrangellia composite terrane, *Geological Society of America Bulletin*, v. 117, p. 570-588.
- Turner S, Caulfield J, Turner M, van Keken P, Maury R, Sandiford M, Prouteau G (2011) Recent contribution of sediments and fluids to the mantle's volatile budget. *Nature Geosci* 5:50–54
- Ussami, N., Cogo de Sa, N., Molina, E.C., 1993. Gravity map of Brazil 2. Regional and residual isostatic anomalies and their correlation with major tectonic provinces. *J. Geophys. Res.* 98, 2199–2208.
- Wada, I., Wang, K.L., He, J.G., Hyndman, R.D., 2008. Weakening of the subduction interface and its effects on surface heatflow, slab dehydration, and mantle wedge serpentization. *J. Geophys. Res.* 113, B04402, doi:10.1029/ 2007JB005190.

Wada, I., Rychert, C. & Wang, K., 2011. Sharp thermal transition in the forearc mantle wedge as a consequence of nonlinear mantle wedge flow, *Geophys. Res. Lett.*, 38, L13308, doi:10.1029/2011GL047705.

Ward, K. M., 2015, Ambient noise tomography across the southern Alaskan Cordillera, *Geophys. Res. Lett.*, 42, 3218-3227, doi:10.1002/2015GL063613

Waring G A 1917 Mineral Springs of Alaska U.S. Geological Survey Water-Supply Paper 418

Willis, J.B., Haeussler, P.J., Bruhn, R.L., Willis, G.C., 2007. Holocene slip rate for the western segment of the Castle Mountain fault, Alaska. *Bull. Seismol. Soc. Am.* 97 (3), 1019–1024.

Ye, S., Flueh, E. R., Kaeschen, D., Von Huene, R., 1997, Crustal Structure along the Edge transect beneath the Kodiak Shelf off Alaska derived from OBH seismic refraction data. *Geophys. J. Int.* 130, 283-302. <http://dx.doi.org/10.1111/j.1365-246X.1997>

Zhang, J., Gao, R., Zeng, L., Li, Q., Guan, Y., He, R., Wang, H., Lu, Z., 2010. Relationship between characteristics of gravity and magnetic anomalies and the earthquakes in the Longmenshan range and adjacent areas. *Tectonophysics* 491, 218–229.

Zweck, C., J. T. Freymueller, and S. C. Cohen (2002), Three-dimensional elastic dislocation modeling of the postseismic response to the 1964 Alaska earthquake, *J. Geophys. Res.*, 107(B4), doi:10.1029/2001JB000409

### SECTION 3

#### APPENDIX A

One-dimensional conductive heat flow equation where the temperature gradient is constant can be calculated using the equation (Fournier's law):

$$q = k \frac{dT}{dz} \quad (1)$$

Where  $q$  is the heat flux,  $\frac{dT}{dz}$  is the temperature gradient and  $k$  is the thermal conductivity. Tanaka et al. (1999) showed the Curie temperature,

$$C = \left( \frac{dT}{dz} \right) D \quad (2)$$

Where  $D$  is the CPD. This equation assumes no heat source or sinks between the earth's surfaces.

Therefore  $D$  the is:

$$D = k \frac{C}{q} \quad (3)$$

## APPENDIX B

Temperature –to-depth (TD) or temperature at depth ( $T_z$ ) profile or curves are computed using three reference temperatures to a given depth. Mathematically;

$$T_z = T_{surf} + T_{sed} + T_{bas} \quad (4)$$

Where:

$T_z$  = temperature at depth (Z) (°C)

$T_{surf}$  = surface temperature (°C)

$T_{sed}$  = temperature contribution of the sediment section within the TC profile (°C)

$T_{bas}$  = temperature contribution of the basement section within the TD profile (°C)

$T_{surf}$  is added to TD curves as a constant. The best source of  $T_{surf}$  is the mean annual ground surface temperature (MAGST). I generated the mean annual ground surface temperatures based on the Western Regional Climate Center (WRCC) online website (URL: [wrcc@dri.edu](http://wrcc@dri.edu) ).

$T_{sed}$  is the component of the TD profile based on the conductivity of the sediments. The predominant mode of heat transfer through the crust is conduction. Mathematically;

$$T_{sed} = \frac{(Q_s - A_{sed}Z_{sed})*(Z_{sed})}{K_{sed}} - \frac{A_{sed}*(Z_{sed})^2}{2K_{sed}} \quad (5)$$

Where:

$Q_s$  = surface heat flow ( $\text{m Wm}^{-2}$ )

$A_{sed}$  = radiogenic heat production of the sedimentary section ( $\mu\text{Wm}^{-3}$ )

$Z_{sed}$  = thickness of sedimentary section (m)

$K_{sed}$  = thermal conductivity of sedimentary section ( $\text{Wm}^{-1}\text{K}$ ).

$T_{bas}$  is the temperature contribution from the basement rocks. Regions with no sediments  $T_{bas}$  is directly added to  $T_{surf}$  to compute for  $T_z$ .

$$T_{bas} = \frac{Q_m * Z_{btm-sed}}{K_{bas}} + \frac{A_{bas} b^2 * \left(1 - e^{\left(-\frac{Z_{btm-sed}}{b}\right)}\right)}{K_{bas}} \quad (6)$$

Where:

$Q_m$ =Mantle heat flow ( $\text{mWm}^{-2}$ )

$A_{bas}$ =radiogenic heat production of the basement rocks ( $\mu\text{Wm}^{-3}$ )

$Z_{btm-sed}$ =thickness of basement section (m)

$K_{bas}$ =thermal conductivity of basement ( $\text{Wm}^{-1}\text{K}$ ). Continental average thermal conductivity of  $2.4 \text{ Wm}^{-1}\text{K}$  (e.g. Batir et al., 2016) is used for this research

$b$ =thickness of heat generation in the basement (m). The thickness of heat generation value is 10 km since sediment thickness is  $\leq 5\text{km}$ . The choice of this value was the same value chosen by previous publications (e.g. Blackwell et al., 2007; Majorowicz and Grasby 2010; Stutz et al 2012; Batir et al 2016)



## APPENDIX C

Table showing GPS time series data used to compute uplift rate.

# ID	Station Name	Lat (deg)	Long (deg)	Ellip. Elev. (m)	Vert. rate(mm/day)	Vert. rate(mm/yr)
AC02	AkhiokCorpAK2005	56.95058441	154.1830444	126.8321	0.0024	0.8742
AC03	AnchorPnt_AK2007	59.77063751	151.8645325	19.6203	0.028	10.199
AC06	BradleyLakAK2005	59.76363754	-150.890564	631.4341	0.025	9.10625
AC07	Buckland__AK2007	65.96129608	161.2866211	176.3173	-0.0011	-0.400675
AC08	CapDouglasAK2007	58.92877579	153.6446991	644.1659	0.0223	8.122775
AC09	KayakIsl__AK2007	59.86847687	144.5238495	368.8863	0.0075	2.731875
AC10	CpSarichefAK2008	54.52258301	-164.886734	170.4717	0.011	4.00675
AC11	ChickaloonAK2005	61.80707932	148.3317566	790.8619	0.0257	9.361225
AC12	ChernaburaAK2008	54.83096314	159.5895691	84.3969	-0.0031	-1.129175
AC13	ChirikofIsAK2008	55.8218956	-155.622406	222.7865	-0.0296	-10.7818
AC14	EstherIsleAK2007	60.84870148	-147.999588	748.7078	0.0038	1.38415
AC15	cooperIndgak2005	60.48133087	149.7240143	151.4435	0.0239	8.705575
AC16	DeepWater_AK2007	60.51820374	148.0932312	34.0404	0.0012	0.4371
AC17	DriftRiverAK2006	60.66390228	152.4038391	882.5885	0.0253	9.215525
AC18	Ushagat_IsAK2008	58.92595673	-152.249527	214.7043	0.0245	8.924125
AC19	FarewellMTAK2008	62.51921463	153.6073303	546.5062	0.0081	2.950425
AC20	Girdwood__AK2005	60.92920685	149.3525085	43.664	0.0192	6.9936
AC21	PerryvilleAK2006	55.92108917	159.1277161	170.9344	-0.0011	-0.400675
AC23	Soldotna__AK2007	60.47509384	150.8779602	80.7912	0.0223	8.122775
AC24	KingSalmonAK2006	58.68157196	156.6527557	36.3621	0.0047	1.711975
AC25	King_Cove_AK2005	55.08896637	162.3140564	584.2617	0.0024	0.8742
AC26	Cape_Gull_AK2008	58.21455383	154.1502991	190.125	0.0112	4.0796

AC27	AC27MNeil_AK2004	59.25250626	- 154.1628876	417.4785	0.009	3.27825
AC28	NagaiIsIndAK2008	55.07849121	- 160.0491638	365.0917	0.0003	0.109275
AC29	Middleton_AK2014	59.42958903	- 146.3399746	56.53133	0.0192	6.9936
AC31	Bald_Head_AK2006	64.6379776	- 162.2391205	228.3407	-0.0005	-0.182125
AC32	Mt_SusitnaAK2006	61.47312164	- 150.7369232	1347.7422	0.0124	4.5167
AC33	TokoDenaliAK2007	62.671178	- 150.6850732	1521.16803	0.0056	2.0398
AC34	OldHarbor_AK2006	57.22002792	- 153.2791748	103.2401	0.0087	3.168975
AC35	PetrofLakeAK2006	59.37581253	- 150.7932434	408.4465	0.0279	10.162575
AC36	MoosePointAK2008	60.95531845	- 150.6083527	46.454	0.021	7.64925
AC37	LakeClark_AK2007	60.43968582	-153.865387	1626.5662	0.0111	4.043175
AC38	Quartz_CrkAK2005	57.753685	- 153.3418732	43.8163	0.0202	7.35785
AC39	ShuyakIsSPAK2006	58.60971832	- 152.3940735	157.1464	0.0263	9.579775
AC40	PortHeidenAK2007	56.93035126	- 158.6185761	39.8903	0.003	1.09275
AC41	PortMollerAK2006	55.90866852	- 160.4073029	407.7255	0.0017	0.619225
AC42	SanakIsIndAK2007	54.47177506	- 162.7836456	257.8949	0.0065	2.367625
AC43	Seal_RocksAK2007	59.52127838	- 149.6287384	69.5244	0.0105	3.824625
AC44	ArcticVly_AK2008	61.24217224	- 149.5671234	832.1389	0.0183	6.665775
AC45	SitkinakIsAK2006	56.56445313	- 154.1809692	451.0515	-0.0101	-3.678925
AC46	Skwentna_RAK2006	61.98626709	- 151.5240021	619.7311	0.0124	4.5167
AC47	SlopeMtn__AK2007	60.08145142	- 152.6239471	922.2508	0.0226	8.23205
AC48	NakedIsl__AK2007	60.64586258	- 147.3430176	379.5367	0.0018	0.65565
AC50	BaldyMtn__AK2007	65.55384827	- 164.5665741	516.8434	-0.0004	-0.1457
AC51	StrandlineAK2007	61.49808121	- 151.8353424	957.3876	0.0188	6.8479

AC52	PilotPointAK2007	57.5672493	- 157.5742188	51.8105	0.0027	0.983475
AC53	Willow_CrkAK2006	61.76897049	- 150.0689545	57.4581	0.009	3.27825
AC55	Yentna_RvrAK2006	62.38444466	- 151.7645883	1012.30531	-0.0667	-24.295475
AC57	ThompsonPaAK2006	61.13859558	- 145.7427063	826.3767	0.0245	8.924125
AC58	StPaulIslAK2008	57.15608978	- 170.2178192	19.3669	-0.0019	-0.692075
AC59	AC59Ursus_AK2004	59.56719589	- 153.5852051	308.5398	0.015	5.46375
AC60	Westeast__AK2008	52.71461868	- 174.0762634	18.2751	0.0072	2.6226
AC61	ChickenM61AK2006	64.02925873	- 142.0758514	745.3835	-0.002	-0.7285
AC62	DenliHwy32AK2004	63.08360672	- 146.3126984	1347.0765	0.0121	4.407425
AC63	ATTPS_____AK2004	63.50242615	- 145.8472443	815.0563	0.0221	8.049925
AC64	MtnDrumVP_AK2004	62.71401596	- 144.3039856	774.5094	0.0284	10.3447
AC65	Mentasta__AK2004	62.83151245	- 143.7042236	735.8649	0.0219	7.977075
AC66	AmchitkaIsAK2005	51.37812805	- 179.3013306	106.7878	-0.0014	-0.50995
AC67	PillarMtn_AK2006	57.79071808	- 152.4254303	347.2405	0.0235	8.559875
AC70	Brokebits_AK2003	63.30471039	- -148.188324	810.8383	0.0087	3.168975
AC71	DeltaJunc_AK2003	64.04930115	- -145.713623	363.9708	0.0099	3.606075
AC72	DonnellyC_AK2002	63.69505692	- 145.8876953	558.7971	0.012	4.371
AC74	Cantwello_AK2002	63.46435547	- 148.8072662	668.5803	0.0079	2.877575
AC75	Hurricane_AK2002	62.99930573	- 149.6088257	608.6088	0.0123	4.480275
AC76	LogCabin__AK2008	63.0399971	- 143.2588196	1585.2498	0.0114	4.15245
AC77	Sourdough_AK2003	62.68803024	- 145.4262543	746.8171	0.0177	6.447225
AC78	Tetlin_2__AK2009	63.11349106	- 142.0279388	643.726	-0.0023	-0.837775
AC79	Montague2_AK2010	59.99786758	- 147.4030457	287.7669	-0.0054	-1.96695
AC80	YentnaRvr2AK2010	62.3940773	- 151.7650452	1114.4486	0.0159	5.791575

## **VITA**

Felix Dziedzorm Ziwu was born in Accra-Ghana in West Africa on September 23 1980.

He attended Bishop Herman Secondary School for his senior secondary certificate. He continued to Kwame Nkrumah University of Science and Technology in the year 2001. He graduated with his bachelor's degree in physics in May 2005 with honors. He worked with E. K. Ziwu Surveying Services and worked as a part-time lecturer at the Ghana School of Surveying and Mapping until July 2011. In the Fall 2011, he entered the Graduate School of University of Texas at El Paso and obtained a masters degree in Geophysics in May 2014. H continued for a PhD in Geological Sciences and worked as a Teaching Assistant. He will be pursuing a career in Geophysics in the industry or academia.

Permanent address: P.O. Box MD 148, Madina-Accra,  
Ghana, West Africa

This dissertation was typed by Ziwu Felix Dziedzorm.